

MODELING OF MULTIDIMENSIONAL HEAT TRANSFER IN A  
RECTANGULAR GROOVED HEAT PIPE

A THESIS SUBMITTED TO  
THE GRADUATE SCHOOL OF NATURAL AND APPLIED SCIENCES  
OF  
MIDDLE EAST TECHNICAL UNIVERSITY

BY

GÜLNIHAL ODABAŞI

IN PARTIAL FULFILLMENT OF THE REQUIREMENTS  
FOR  
THE DEGREE OF DOCTOR OF PHILOSOPHY  
IN  
MECHANICAL ENGINEERING

JUNE 2014



Approval of the thesis:

**MODELING OF MULTIDIMENSIONAL HEAT TRANSFER IN A  
RECTANGULAR GROOVED HEAT PIPE**

submitted by **GÜLNIHAL ODABAŞI** in partial fulfillment of the requirements  
for the degree of **Doctor of Philosophy in Mechanical Engineering De-  
partment, Middle East Technical University** by,

Prof. Dr. Canan Özgen \_\_\_\_\_  
Dean, Graduate School of **Natural and Applied Sciences**

Prof. Dr. Suha Oral \_\_\_\_\_  
Head of Department, **Mechanical Engineering**

Prof. Dr. Zafer Dursunkaya \_\_\_\_\_  
Supervisor, **Mechanical Engineering, METU**

**Examining Committee Members:**

Prof. Dr. Haluk Aksel \_\_\_\_\_  
Mechanical Engineering Department, METU

Prof. Dr. Zafer Dursunkaya \_\_\_\_\_  
Mechanical Engineering Department, METU

Prof. Dr. İ. Hakkı Tuncer \_\_\_\_\_  
Aeronautical Engineering Department, METU

Prof. Dr. I. Hakan Tarman \_\_\_\_\_  
Engineering Sciences Department, METU

Assist. Prof. Dr. Barbaros Çetin \_\_\_\_\_  
Mechanical Engineering Department, Bilkent University

**Date:** \_\_\_\_\_

I hereby declare that all information in this document has been obtained and presented in accordance with academic rules and ethical conduct. I also declare that, as required by these rules and conduct, I have fully cited and referenced all material and results that are not original to this work.

Name, Last Name: GÜLNIHAL ODABAŞI

Signature :

# ABSTRACT

## MODELING OF MULTIDIMENSIONAL HEAT TRANSFER IN A RECTANGULAR GROOVED HEAT PIPE

Odabaşı, Gülnihal

Ph.D., Department of Mechanical Engineering

Supervisor : Prof. Dr. Zafer Dursunkaya

June 2014, 156 pages

Heat pipes are generally preferred for electronics cooling application due to large heat transfer capacity in spite of small size. Micro heat pipes use small channels, whose dimension is on the order of micrometers, to generate necessary capillary action maintaining fluid flow for heat pipe operation. In the present study a flat micro heat pipe with rectangular cross section is analyzed numerically. A simplified axial fluid flow model is utilized to find liquid–vapor interface shape variation along the heat pipe axis through Young–Laplace equation. Three dimensional steady heat transfer model both in solid and fluid domain is coupled with flow equation. A coordinate transformation is applied for the heat transfer analysis in fluid domain, since the physical domain has an irregular shape along the heat pipe axis. Phase change heat transfer is introduced to the study as a boundary condition, where evaporation and condensation models at the liquid–vapor interface are solved. Heat transfer equation in liquid domain includes convection, which is generally neglected and the effect of the convection on

heat pipe performance is investigated. The study is performed to investigate the effect of physical dimension of heat pipe and boundary condition on the performance of the heat pipe. Also a sample study simulating the cooling of an electronic component is conducted to define the groove size according to the defined maximum operating temperature.

Keywords: Flat heat pipe, grooved, multidimensional heat transfer

# ÖZ

## DİKDÖRTGEN OLUKLU ISI TÜPÜNDE ÇOK BOYUTLU ISI TRANSFERİ MODELLEMESİ

Odabaşı, Gülnihal

Doktora, Makina Mühendisliği Bölümü

Tez Yöneticisi : Prof. Dr. Zafer Dursunkaya

Haziran 2014 , 156 sayfa

Küçük boyutlarına karşın yüksek ısı transfer kapasiteleri nedeniyle ısı tüpleri genellikle elektroniklerin soğutulmasında tercih edilmektedir. Mikro ısı tüpleri mikrometre ölçüsündeki ince kanalları yardımıyla ısı tüpündeki sıvının akışını sağlayan kapilleri etkiyi oluşturur. Bu çalışmada dikdörtgen kesitli yivlere sahip düz bir ısı tüpü nümerik olarak incelenmiştir. Eksenel akış basitleştirilmiş bir modelle benzetimlenmiş ve Young–Laplace eşitliği kullanılarak sıvı–gaz arayüzünün eksen boyunca değişimi elde edilmiştir. Üç boyutlu ısı transferi denklemi hem katı hem de sıvı içerisinde sıcaklık dağılımı için çözülmüş ve akış modeli ile birleştirilmiştir. Sıvı çözüm alanının şekli ısı tüpü eksenini boyunca değiştiğinden bu alandaki denklemler için koordinat dönüşümü uygulanmıştır. Buharlaşma ve yoğuşma modellerinden elde edilen faz değişimi sırasındaki ısı transferi probleme sınır koşulu olarak eklenmiştir. Sıvı içerisinde ısı transferi modeline genellikle ihmal edilen taşınım modeli de eklenerek etkisi incelenmiştir. Bu çalışma ısı tüpü

boyutları ve sınır koşulunun performansa etkisini incelemek üzere kullanılmıştır. Ayrıca elektronik bir komponentin soğutulması simule edilerek oluk ölçüleri tanımlanan maksimum çalışma sıcaklığına göre belirlenmiştir.

Anahtar Kelimeler: Düz ısı tüpü, oluklu, çok boyutlu ısı transferi

*To my parents*

## ACKNOWLEDGMENTS

The author wishes to express her gratitude to her thesis supervisor Dr. Zafer Dursunkaya for his guidance, encouragement and taking time for through and long discussions to understand the physical aspect of the problem with a lot of how's and why's.

The author also express her appreciation to Dr. M.Ali Ak and Fatih Çevik for their technical support in FORTRAN, which saves time to obtain the solution.

Somebody compared doctorate study to running a marathon. The author would like to thank her parents for their support and patience along this long period. Special thanks go to her friends Nalan, Aylin, Gani and İlknur for their motivation, moral support and creating social events, even they had to listen some technical issues about the problem.

# TABLE OF CONTENTS

ABSTRACT . . . . .	v
ÖZ . . . . .	vii
ACKNOWLEDGMENTS . . . . .	x
TABLE OF CONTENTS . . . . .	xi
LIST OF TABLES . . . . .	xv
LIST OF FIGURES . . . . .	xvi
LIST OF ABBREVIATIONS . . . . .	xxii
CHAPTERS	
1 INTRODUCTION . . . . .	1
1.1 Types of Heat Pipes . . . . .	4
1.1.1 Micro heat pipes . . . . .	4
1.1.2 Flat heat pipes . . . . .	6
1.1.3 Loop heat pipes . . . . .	6
1.1.4 Variable conductance heat pipe . . . . .	7
1.2 Operational Limits of Heat Pipes . . . . .	8
1.2.1 Capillary limit . . . . .	8

1.2.2	Entrainment limit . . . . .	10
1.2.3	Sonic limit . . . . .	10
1.2.4	Viscous limit . . . . .	11
1.2.5	Boiling limit . . . . .	11
1.3	Literature Review . . . . .	11
1.3.1	Heat pipes with a porous wick structures . . . . .	12
1.3.2	Heat pipes with grooved wick structures . . . . .	17
1.3.3	Heat pipes with combined grooved and porous wick structure . . . . .	25
1.4	Description of the Current Study . . . . .	27
2	PHASE CHANGE . . . . .	29
2.1	Evaporation Modeling . . . . .	29
2.2	Condensation Modeling . . . . .	39
3	SOLUTION METHODOLOGY . . . . .	47
3.1	Flow Modeling in the Working Fluid . . . . .	49
3.2	Heat Transfer Modeling . . . . .	54
3.2.1	Grid generation . . . . .	60
3.3	Solution Procedure . . . . .	61
4	RESULTS FOR HEAT PIPE MODEL . . . . .	67
4.1	Validation of the Present Study . . . . .	67
4.2	A Parametric Study of Heat Pipe Performance . . . . .	74
4.2.1	The effect of ambient heat transfer coefficient . . . . .	76

4.2.2	The effect of solid thermal conductivity . . . . .	77
4.2.3	The effect of heat load . . . . .	79
4.2.4	The effect of initial interface radius . . . . .	81
4.2.5	The effect of groove depth . . . . .	83
4.2.6	The effect of fin thickness . . . . .	85
4.2.7	The effect of groove width . . . . .	87
4.2.8	The effect of working fluid . . . . .	88
4.2.9	The effect of heat source and sink region length	91
4.3	Maximum Heat Capacity of the Heat Pipe . . . . .	93
4.3.1	Fixed total length of fin thickness and groove width . . . . .	93
4.3.2	Effect of different groove width and depth for fixed fin thickness . . . . .	95
4.3.3	Effect of different heat pipe length . . . . .	102
5	DESIGN PROBLEM . . . . .	105
5.1	Definition of the Design Problem . . . . .	105
5.2	Result for the Design Problem . . . . .	107
6	CONCLUSION . . . . .	111
	REFERENCES . . . . .	115
APPENDICES		
A	DERIVATION OF ENERGY EQUATION IN THE TRANSFORMED DOMAIN . . . . .	121

B	ENERGY BALANCE EQUATIONS AT THE INTERFACES . . . . .	127
B.1	Energy Balance for Region I . . . . .	128
B.2	Energy Balance for Region II . . . . .	132
B.3	Energy Balance for Region III . . . . .	135
B.4	Energy Balance for Region IV . . . . .	139
B.5	Energy Balance for Region V . . . . .	143
B.6	Energy Balance for Liquid–Vapor Interface . . . . .	148
	CURRICULUM VITAE . . . . .	155

## LIST OF TABLES

### TABLES

Table 2.1	Physical parameters used in evaporation model . . . . .	37
Table 2.2	Physical properties used for condensation mass flux calculation	43
Table 4.1	Dimension and physical properties used in validation model .	68
Table 4.2	Dimension and physical properties used in the parametric study	75
Table 4.3	Thermophysical properties of working fluids . . . . .	89
Table 4.4	Dimensions of heat source, heat sink and adiabatic regions . .	91
Table 5.1	Dimension and physical properties used for design problem . .	107
Table 5.2	Test cases for the design problem . . . . .	108

## LIST OF FIGURES

### FIGURES

Figure 1.1 Heat pipe wick types (a) Axially grooved (b) Sintered powder [2] . . . . .	3
Figure 1.2 Different micro heat pipe cross-sections [4] . . . . .	5
Figure 1.3 Construction of flat micro heat pipes [5, 6] . . . . .	6
Figure 1.4 A typical loop heat pipe [7] . . . . .	7
Figure 1.5 Schematics of a variable conductance heat pipe [8] . . . . .	8
Figure 2.1 Evaporation micro region and subregions . . . . .	31
Figure 2.2 Coordinate system used in the evaporating region . . . . .	32
Figure 2.3 Pressure balance at the liquid–vapor interface . . . . .	33
Figure 2.4 Liquid film thickness variation along the micro region . . . . .	38
Figure 2.5 Heat flux variation along the micro region . . . . .	39
Figure 2.6 Condensation region and the groove geometry . . . . .	40
Figure 2.7 Liquid film thickness variation along the fin top . . . . .	44
Figure 2.8 Heat flux variation along the fin top . . . . .	44
Figure 2.9 Liquid film thickness variation along the fin top for different contact angles . . . . .	45
Figure 2.10 Heat flux variation along the fin top for different contact angles	45

Figure 2.11 Liquid film thickness variation along the fin top for different temperature difference . . . . .	46
Figure 2.12 Heat flux variation along the fin top for different temperature difference . . . . .	46
Figure 3.1 Heat and mass flow paths . . . . .	48
Figure 3.2 Axial variation of the liquid shape in the grooves, and the solid domain . . . . .	48
Figure 3.3 Forces acting on a fluid particle in the axial direction . . . . .	49
Figure 3.4 Groove geometry . . . . .	52
Figure 3.5 Mass balance . . . . .	53
Figure 3.6 Heat transfer domain geometry with boundary conditions . . . . .	55
Figure 3.7 Computational grid in the physical domain at a cross-section of the channel . . . . .	61
Figure 3.8 Mass balance in the liquid domain for the calculation of transverse velocity . . . . .	64
Figure 3.9 Flowchart for the solution procedure . . . . .	66
Figure 4.1 Liquid interface radius variation along the heat pipe axis . . . . .	69
Figure 4.2 Axial liquid velocity variation along the heat pipe axis . . . . .	70
Figure 4.3 Edge temperature variation along the heat pipe axis . . . . .	70
Figure 4.4 3-D temperature distribution in the liquid and solid regions . . . . .	71
Figure 4.5 Edge temperature variation in the heat pipe and copper block . . . . .	74
Figure 4.6 Liquid interface radius variation along the heat pipe axis for different ambient heat transfer coefficients . . . . .	76

Figure 4.7 Edge temperature variation along the heat pipe axis for different ambient heat transfer coefficients . . . . .	77
Figure 4.8 Liquid interface radius variation along the heat pipe axis for different solid thermal conductivity . . . . .	78
Figure 4.9 Edge temperature variation along the heat pipe axis for different solid thermal conductivity . . . . .	78
Figure 4.10 Liquid interface radius variation along the heat pipe axis for different heat load values . . . . .	79
Figure 4.11 Edge temperature variation along the heat pipe axis for different heat load values . . . . .	80
Figure 4.12 Vapor temperature and total fluid mass variation for different heat load values . . . . .	80
Figure 4.13 Liquid interface radius variation along the heat pipe axis for different initial radius values . . . . .	82
Figure 4.14 Edge temperature variation along the heat pipe axis for different initial radius values . . . . .	82
Figure 4.15 Vapor temperature and fluid mass for different initial radius values . . . . .	83
Figure 4.16 Liquid interface radius variation along the heat pipe axis for different groove depths . . . . .	84
Figure 4.17 Edge temperature variation along the heat pipe axis for different groove depths . . . . .	84
Figure 4.18 Liquid interface radius variation along the heat pipe axis for different fin thickness . . . . .	86
Figure 4.19 Edge temperature variation along the heat pipe axis for different fin thickness . . . . .	86

Figure 4.20 Liquid interface radius variation along the heat pipe axis for different groove width . . . . .	87
Figure 4.21 Edge temperature variation along the heat pipe axis for different groove width . . . . .	88
Figure 4.22 Liquid interface radius variation along the heat pipe axis for different working fluids . . . . .	90
Figure 4.23 Edge temperature variation along the heat pipe axis for different working fluids . . . . .	90
Figure 4.24 Liquid interface radius variation along the heat pipe axis for different heat sink and source lengths . . . . .	92
Figure 4.25 Edge temperature variation along the heat pipe axis for different heat sink and source lengths . . . . .	92
Figure 4.26 Maximum heat flux and the vapor temperature variation for different groove width to fin thickness ratios . . . . .	94
Figure 4.27 Fluid mass for different groove width to fin thickness ratios . . . . .	95
Figure 4.28 Maximum heat flux variation for different groove depths and widths for an initial radius of 0.9 mm. . . . .	96
Figure 4.29 Maximum heat flux variation for different groove depths and widths for an initial radius of 1.2 mm. . . . .	97
Figure 4.30 Maximum heat flux variation for different groove depths and widths for an initial radius of 2.4 mm. . . . .	97
Figure 4.31 Total fluid mass variation for different groove depths and widths . . . . .	98
Figure 4.32 Maximum heat flux and vapor temperature variation for different groove depths and widths . . . . .	99

Figure 4.33 Maximum heat flux variation for constant groove depth and width values . . . . .	100
Figure 4.34 Total fluid mass and temperature variation for 35000 W/m <sup>2</sup>	101
Figure 4.35 Maximum heat flux and total fluid mass distribution for vapor temperature 393 K . . . . .	101
Figure 4.36 Maximum heat flux variation for different heat pipe lengths	102
Figure 4.37 Maximum heat flux variation in terms of heat source length to heat pipe length ratio . . . . .	103
Figure 5.1 Liquid interface radius variation along heat pipe axis . . . . .	109
Figure 5.2 Edge temperature variation along heat pipe axis . . . . .	110
Figure 5.3 Maximum edge temperature for test cases . . . . .	110
Figure B.1 Energy balance for Region I . . . . .	129
Figure B.2 Enthalpy flow to Region I . . . . .	131
Figure B.3 Heat balance for Region II . . . . .	133
Figure B.4 Enthalpy flow to Region II . . . . .	135
Figure B.5 Heat balance for Region III . . . . .	136
Figure B.6 Enthalpy flow to Region III . . . . .	138
Figure B.7 Heat balance for Region IV . . . . .	140
Figure B.8 Enthalpy flow to Region IV . . . . .	142
Figure B.9 Heat balance for Region V . . . . .	144
Figure B.10 Enthalpy flow to Region V . . . . .	147
Figure B.11 Heat balance at the liquid–vapor interface . . . . .	149

Figure B.12 Enthalpy flow at the liquid–vapor interface . . . . . 152

## LIST OF ABBREVIATIONS

$A$	Cross sectional area, $\text{m}^2$
$A_d$	Dispersion constant, J
$b$	Half groove width, m
$c$	Accommodation coefficient
$C_p$	Specific heat, J/kg K
$d$	Groove depth, m
$D_h$	Hydraulic diameter, m
$f$	Friction coefficient
$F$	Function for surface equation
$h$	Groove thickness, m
$h_{lv}$	Latent heat of evaporation, J/kg
$h_{pc}$	Phase change heat transfer coefficient, $\text{W}/\text{m}^2 \cdot \text{K}$
$h_{amb}$	Ambient heat transfer coefficient, $\text{W}/\text{m}^2 \cdot \text{K}$
$k$	Thermal conductivity, $\text{W}/\text{m} \cdot \text{K}$
$L$	Length, m
$M$	Molar mass of liquid, kg/mol
$\dot{m}$	Mass flow rate, kg/s
$m'$	Mass flow rate per unit length, $\text{kg}/\text{s} \cdot \text{m}$
$m''$	Mass flux, $\text{kg}/\text{s} \cdot \text{m}^2$
$m''_c$	Condensation mass flux, $\text{kg}/\text{s} \cdot \text{m}^2$
$m''_e$	Evaporation mass flux, $\text{kg}/\text{s} \cdot \text{m}^2$
$n$	Surface normal
$P$	Pressure, Pa
$P_c$	Capillary pressure, Pa
$P_d$	Dispersion pressure, Pa
$q''$	Heat flux, $\text{W}/\text{m}^2$
$R$	Liquid–vapor interface radius, m
$R_u$	Universal gas constant, $\text{J}/\text{mol} \cdot \text{K}$

Re	Reynolds number
$s$	Coordinate for phase change analysis, m
$T$	Temperature, K
$T_{amb}$	Ambient temperature, K
$T_w$	Temperature at fin top corner point, K
$t$	Fin thickness, m
$u$	Axial velocity, m/s
$V$	Molar volume of liquid, m <sup>3</sup> /mol
$x$	Coordinate along the width of heat pipe, m
$y$	Coordinate along the heat pipe axis, m
$z$	Coordinate along the depth of heat pipe, m

***Greek Symbols***

$\delta$	Liquid film thickness, m
$\eta$	Transformed coordinate in $y$ -direction, m
$\lambda$	Transformed coordinate in $x$ -direction, m
$\xi$	Transformed coordinate in $z$ -direction, m
$\mu$	Dynamic viscosity, Pa·s
$\nu$	Kinematic viscosity, m <sup>2</sup> /s
$\Phi$	Viscous dissipation, s <sup>-2</sup>
$\rho$	Density, kg/m <sup>3</sup>
$\sigma$	Surface tension, N/m
$\theta$	Liquid–solid contact angle
$\tau$	Shear stress, Pa

***Subscripts***

$c$	Condensation region
$e$	Evaporation region
$l$	Liquid
$lv$	Liquid–vapor
$lw$	Liquid–groove wall
$nb$	Normal at the lower surface
$nt$	Normal at the upper surface
$pc$	Phase change
$s$	Solid
$t$	Total

$v$	Vapor
$x$	Component along the $x$ -coordinate
$y$	Component along the $y$ -coordinate
$z$	Component along the $z$ -coordinate

# CHAPTER 1

## INTRODUCTION

Heat pipes are passive devices that transport heat from a source (evaporator) to a sink (condenser) over a distance *via* the latent heat of evaporation of a working fluid. A typical heat pipe consists of a sealed case which contains a working fluid and a wicking structure which lines the inner wall. The case is initially vacuumed, then charged with a working fluid, and hermetically sealed. When the heat pipe is heated at one end, the working fluid evaporates and the vapor travels through the hollow core to the other end of the heat pipe, where heat is removed by a heat sink or other means, where the vapor condenses. The phase change causes liquid–vapor interface variation along the heat pipe axis, which generates a capillary pressure difference. The liquid then travels back to the condenser end *via* the wick due to this capillary action. This fluid motion is a continuous process as long as there is a temperature difference between the two ends. The heat pipe is similar in some respects to a thermal syphon in which the lower end is heated and vaporized liquid moves to the cold end and the condensate returns to the hot end due to the action of gravity. The basic heat pipe differs from thermal syphon in that capillary forces generated by the wick structure return the condensate to the evaporator. Capillary fluid movement is achieved when the intermolecular adhesive forces between a fluid and a solid are greater than the cohesive forces within the fluid itself. This results in an increase in surface tension on the fluid and a force is applied causing the fluid to move. The main difference between a heat pipe and a thermal syphon is that the evaporator in the heat pipe may be in any orientation, uninfluenced by the effect of gravity.

A Perkins tube can be regarded as predecessor of heat pipe, which was patented in 1831 by A.M Perkins [1]. This device is basically a hermetic tube boiler in which water is circulated. The first use of the Perkins tube operating on a two-phase cycle was patented by J. Perkins in 1936 [1]. The heat pipe concept was first introduced by R.S. Gaugler in a patent published in 1944. It is basically a thermal syphon, where a capillary structure was proposed as the means for returning the liquid from the condenser to the evaporator. Grover's patent on behalf of the US Atomic Energy Commission in 1963, introduced the name "heat pipe" to describe the device. The patent included a limited theoretical analysis and results of experiments carried out on stainless steel heat pipes incorporating a wire mesh wick and sodium as the working fluid. During 1967 and 1968, several studies appeared in the scientific press and mentioned increased thermal conductivity when compared with solid conductors such as copper. Work at Los Alamos Laboratory continued at a high level and space application of first heat pipe took place in 1967 [1]. Since then heat pipes have been used in different applications and numerous numerical and experimental studies were performed for different heat pipe types.

A container, a wick (or capillary structure) and working fluid are the basic components of a heat pipe. The function of the container is to isolate the working fluid from the outside environment. The material of the container should be compatible with the working fluid. Thermal conductivity of the container should be high to provide effective heat transfer from the heat source. For practical reasons, ease of fabrication is also a point to be considered. Possible heat pipe materials include pure metal alloys such as aluminum, stainless steel, or copper; composite materials, either metal or carbon composites.

The purpose of the wick is to generate a capillary pressure to transport the working fluid from the condenser to the evaporator. It must also be able to distribute the liquid around the evaporator where heat is received. The wick structure can be made of porous materials, which are called homogeneous wicks, or fine grooves carved in the container can be used. Meshes, sintered powders or fibrous materials (ceramic or carbon fibers) are some forms of homogeneous wicks. Maximum capillary head is generated with decreasing pore size, however,

wick permeability increases with increasing pore size, therefore pore size should be optimized according to operational condition.

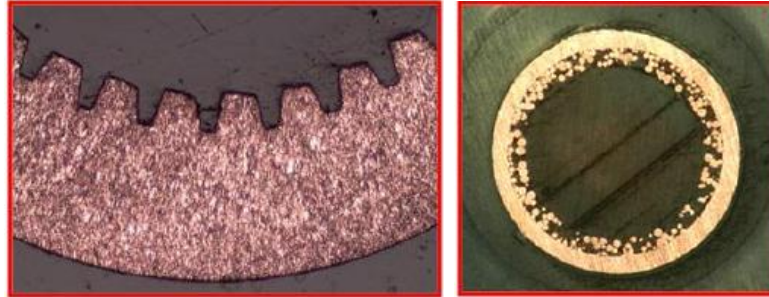


Figure 1.1: Heat pipe wick types (a) Axially grooved (b) Sintered powder [2]

First consideration for a suitable working fluid selection is the operating temperature range, but compatibility with the wick structure and container should also be considered. A high latent heat of working fluid is desirable for more effective heat transfer. Surface tension of the working fluid should be high to generate large capillary forces. The working fluid should also have good wettability characteristics on the wick structure, to improve evaporation. From helium and nitrogen for cryogenic temperatures, to liquid metals like sodium and potassium for high temperature applications, there is a wide range of working fluid selection alternatives. Some of the more common heat pipe fluids used for electronics cooling applications are ammonia, water, acetone and methanol.

When a heat source and heat sink are placed at a distance, heat pipes form an efficient path for heat transfer. Heat capacity of a heat pipe is greater than a solid conductor due to the phase change and this low thermal resistance across hot and cold ends reduces the required temperature difference. This heat spreading ability finds a wide application area in electronics cooling. Thermal management is regarded to be the limiting factor in the development of higher power electronic devices. Current systems can dissipate heat up to 100 W per printed circuit boards. It is also desirable to maintain standard size of casing and connections,

therefore, more components are inserted on the same board by minimizing components size. Traditional methods such as forced cooling become inadequate and multiphase heat transfer in channels having cross-sections of 50–1000 micrometers become attractive. The micro channels may be used in an array, capable of dissipating up to  $100 \text{ W/cm}^2$ . In electronics cooling applications three main features of the heat pipes are used, which are the separation of heat source and sink, temperature flattening and temperature control. Electronic components on different platforms such as personal computers, laptops, aircraft or satellite systems utilize the efficient cooling ability of heat pipes. They are also proposed for cooling heat dissipating devices used for micro fabrication processes; such as laser diodes and other small localized heat generating devices such as photovoltaic cells. There are some biomedical applications such as the treatment of carcinoma and control of epileptic seizures. Heat pipes are also integrated into air conditioners, or refrigerators to improve performance.

Other uses of heat pipe include chemical reactors that take advantage of temperature flattening characteristics of heat pipes to maintain the temperature of catalyst approximately a constant. Liquid metal heat pipes can be used in high temperature chemical reactors. Thermal gradients in spacecraft structure due to solar radiation and internal heat generation by electronic components can be alleviated using heat pipes.

## **1.1 Types of Heat Pipes**

### **1.1.1 Micro heat pipes**

Micro heat pipes consist of a long, thin, noncircular channels that utilize sharp-angled corner regions as liquid arteries. The micro heat pipe, as defined by Cotter [3] has “channels which are so small, that the mean curvature of the vapor–liquid interface is comparable in magnitude to the reciprocal of the hydraulic radius of the flow channel”. The size of the hydraulic radius is generally 100 micrometers. These types of heat pipes can be employed in electronics cooling as well as in the cooling of semiconductors, photovoltaic cells or medical

devices.

Micro heat pipes of different shapes have been used in various applications (Figure 1.2). The triangular shape has been proposed for the first time by Cotter [3] in a theoretical study related to the determination of the maximum heat transfer capacity of a microchannel. Rectangular shape with straight or incurved sides, square shape with straight sides, trapezoidal shape, circular shape with incurved walls, triangular cross section with concave walls are some examples of internal and external geometries used in heat pipes [4]. Capillary pressure difference insures the flow of the working fluid from the condenser back through the corner regions functioning as a wick.

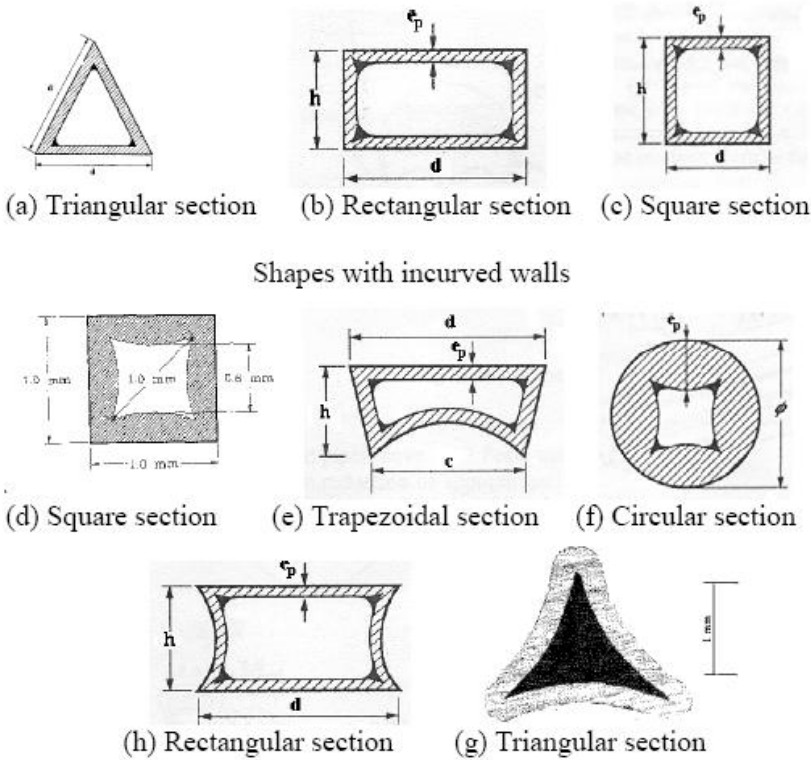


Figure 1.2: Different micro heat pipe cross-sections [4]

### 1.1.2 Flat heat pipes

Flat heat pipes are similar to traditional cylindrical heat pipes but have a rectangular cross-section. They are used to cool and render uniform temperature distribution on semiconductor or transistor packages assembled in arrays on top of the heat pipe. For the metallic flat mini heat pipes, axial microgrooves with triangular, rectangular, and trapezoidal shapes are fabricated. Microgrooves mixed with screen mesh or sintered metal are proposed to improve the performance. A number of different techniques including high speed dicing and rolling method, Electric Discharge Machining (EDM), CNC milling process, drawing and extrusion processes have been applied to fabrication of microgrooves.

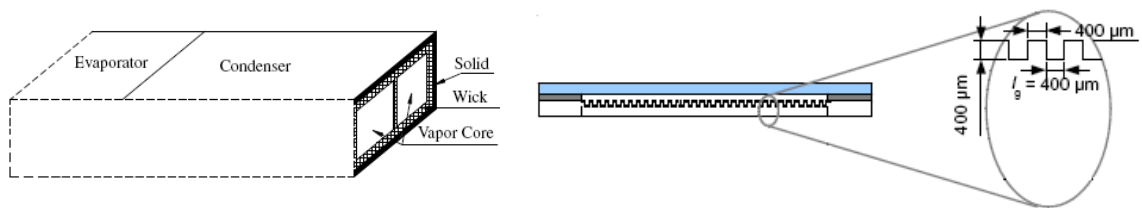


Figure 1.3: Construction of flat micro heat pipes [5, 6]

### 1.1.3 Loop heat pipes

Loop heat pipes have separate vapor and liquid lines between the evaporator and condenser sections. A unique feature of the loop heat pipe is the use of a compensation chamber which helps maintain the fluid inventory. Loop heat pipes utilize high pumping power allowing heat to be transported for several meters since loop heat pipes have a wick structure only in the evaporator section. Loop heat pipes are typically used in aerospace applications and electronics cooling.

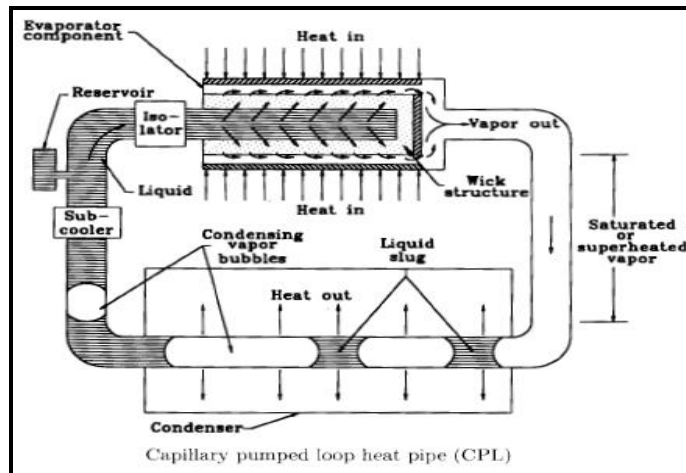


Figure 1.4: A typical loop heat pipe [7]

#### 1.1.4 Variable conductance heat pipe

This type of heat pipe maintains the heat source temperature at an almost constant level over a wide range of heat inputs. This is achieved by maintaining a constant pressure but at the same time varying the condensation area, which is called the “gas buffering”. The reservoir, whose volume is much larger than the heat pipe, is filled with an inert gas. During normal operation the pressure in the reservoir is equal to the saturation pressure of the fluid. When the temperature of the source increases, the saturation pressure increases and the gas in the reservoir recedes to increase the condensation area. The applications range from thermal control of components on satellites to conventional electronics cooling.

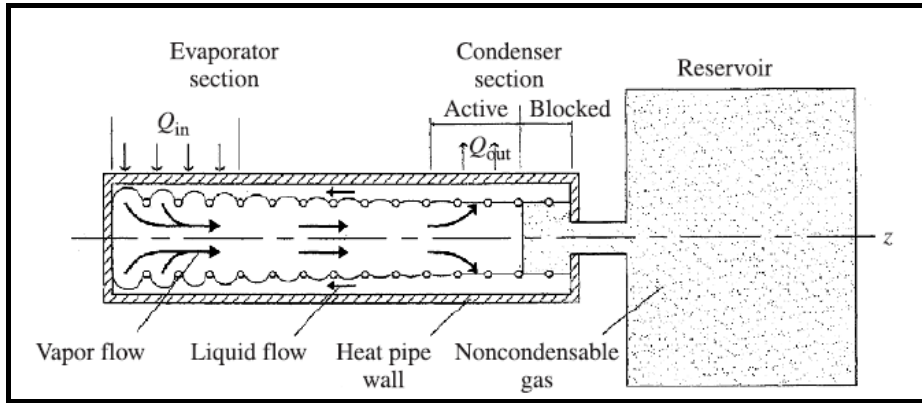


Figure 1.5: Schematics of a variable conductance heat pipe [8]

## 1.2 Operational Limits of Heat Pipes

Limitations of the maximum heat input that may be transported by a heat pipe can be divided into two primary categories, limits that result in heat pipe failure and limits that do not. For the limitations resulting in heat pipe failure, all are characterized by insufficient liquid flow to the evaporator for a given heat input, thus resulting in dry-out of the evaporator wick structure. However, limitations not resulting in heat pipe failure require that the heat pipe operate at an increased temperature for an increase in heat input. Capillary, boiling and entrainment limits cause dry-out of the heat pipe. The definitions of the limitations are summarized in the following sections.

### 1.2.1 Capillary limit

A liquid droplet on a solid surface has three interfaces, one between the solid and vapor, a second one between the solid and liquid, and a third one between the liquid and vapor. There are two types of forces between different substances.

The forces which act between neighboring parts of the same substance are called forces of cohesion, and those which act between different substances are called forces of adhesion. These forces are quite insensible when separated by a measurable distance; however, they become perceptible when the distance becomes exceedingly small. The action between a small size container and a liquid is named the capillary action. The shape of a liquid–vapor interface (meniscus) is dependent on the liquid’s surface tension and the solid–liquid adhesion force. If the adhesion force is greater than the surface tension, the liquid near the solid will be forced upward. The capillary pressure created by two menisci of different radii of curvature is given by the Young–Laplace equation, where  $R_I$  and  $R_{II}$  are principal radii of the meniscus surface,

$$P_c = \sigma \left( \frac{1}{R_I} + \frac{1}{R_{II}} \right). \quad (1.1)$$

In the heat pipe as the liquid in the evaporator vaporizes, the radius of curvature of the menisci in the wick decreases. The difference in the radius of curvature results in capillary pressure difference, which is the basic driving force for liquid motion in a heat pipe.

When the capillary forces, developed through the wick structure, are insufficient to drive back enough liquid from the condenser to the evaporator, dry-out occurs in the evaporator and the heat pipe will fail to operate. Under normal operating conditions capillary pressure difference is greater than the total pressure drop along the heat pipe, which is made up of three components defined below.

- The pressure drop in the liquid phase,  $\Delta P_l$ , required to drive the liquid from the condenser to the evaporator.
- The pressure drop in vapor the phase,  $\Delta P_v$ , required to cause vapor to flow from the evaporator to the condenser.
- The pressure due to gravitational head,  $\Delta P_g$ , which may be zero, positive or negative depending on the inclination of the heat pipe.

The condition defined by the following relation should be satisfied for proper

operation of a heat pipe, otherwise dry-out condition occurs at the evaporator,

$$\Delta P_c > \Delta P_l + \Delta P_v + \Delta P_g. \quad (1.2)$$

### 1.2.2 Entrainment limit

In a heat pipe the liquid and vapor flow in opposite directions, whose interaction results in shear forces at the liquid–vapor interface. The magnitude of the force depends on the vapor properties and velocity, where liquid resists this force by the surface tension. At high vapor velocities, droplets of liquid in the wick can be torn from the wick and entrained into the vapor. This results in insufficient liquid flow through the wick structure.

### 1.2.3 Sonic limit

The sonic limit is typically experienced in liquid metal heat pipes during start-up or low-temperature operations due to the associated very low vapor densities under these conditions. With the increased vapor velocities inertial effects of the vapor flow become significant, and heat pipe may no longer operate in a nearly isothermal state, resulting in an increased temperature gradient along the heat pipe. An analogy between this mode of heat pipe operation and compressible flow in a converging-diverging nozzle can be made. In a converging-diverging nozzle, the mass flow rate is constant and the vapor velocity varies due to the varying cross-sectional area. In heat pipes, however, the flow area is typically constant and the vapor velocity varies due to mass addition (evaporation) and mass rejection (condensation) along the heat pipe. As in nozzle flow, decreased outlet (back) pressure, or in the case of heat pipes, condenser temperatures, result in a decrease in the evaporator temperature until the sonic limit is reached. Any further increase in the heat rejection rate does not reduce the evaporator temperature or the maximum heat transfer capability but only reduces the condenser temperature due to the existence of choked flow. The sonic limitation actually serves as an upper bound to the axial heat transport capacity and does

not necessarily result in dry-out of the evaporator wick or total heat pipe failure.

#### **1.2.4 Viscous limit**

When the heat pipe operates at low temperatures, the available vapor (saturation) pressure in the evaporator region may be very small to provide required pressure gradient to drive the vapor from the evaporator to the condenser. In this case, the total vapor pressure is balanced by opposing viscous forces in the vapor channel. Thus, the total vapor pressure within the vapor region may be insufficient to sustain an increased flow. This low-flow condition in the vapor region is referred to as the viscous limit.

#### **1.2.5 Boiling limit**

For low values of heat flux, heat is transported to the liquid surface partly by conduction through the wick and liquid, partly by convection. Evaporation occurs from the liquid surface. As the heat flux increases, the liquid in contact with the container wall will be superheated and bubbles will form. With further increase in the input heat load the wick will dry out and heat pipe stops to operate.

### **1.3 Literature Review**

In order to better understand the physical mechanism governing the heat and momentum transfer in heat pipes and to optimize product design, mathematical models were developed and experiments were conducted. Previous studies are summarized in the following sections. The summary is organized according to the wick structure, where the heat pipes with homogeneous or porous wick structure will be explained first. Next, the studies on the heat pipes with grooved wick structure with different cross-sections will be summarized. Finally, some examples about the heat pipes will be given, where the porous and grooved wick structure are combined to improve the heat removal capacity.

### 1.3.1 Heat pipes with a porous wick structures

A flat heat pipe with a porous wick structure is generally composed of a flat container, whose inner side is lined with the wick structure and has a hollow core for vapor flow. Heat pipes with groove wick structure can only transfer heat along the groove orientation, however, heat pipes with porous wick structure can provide heat transfer in any direction. Therefore, they are sometimes referred as heat spreaders. This property finds wide application in electronics cooling, where the temperature gradient is reduced and localized hot spots are eliminated. Homogeneous wick structure also allows cooling of multiple heat sources, such as integrated heat pipes on electronic boards or chips.

Vafai and Wang [9] analyzed a specific application of a flat heat pipe, where it was used to cool a medical device used in Boron Neutron Capture Therapy. The heat pipe material was aluminum and the working fluid, heavy water. Heat pipe contained a top and a bottom wick structure and the area for vapor flow was divided into channels with vertical wicks. An analytical solution is obtained for the velocity and pressure distribution in the vapor and liquid phases. Clausius–Clapeyron relation was used to obtain the vapor temperature and operating condition. It was shown that the capillary and boiling limits were not exceeded and operating temperature was below the operation point of the medical device. In this application heat source was located at the top center of the heat pipe, where the remaining area served as the condensation region. It was also shown that vapor flow was not symmetric and maximum velocity shifted towards the bottom side due to the vapor injection from the heat source region, whereas the flow became symmetric away from the heat source region towards the outer sides of the heat pipe. In [9] vapor flow was analyzed as pseudo-three dimensional and liquid flow was simulated using Darcy’s law. The study on the same heat pipe configuration was extended by Zhu and Vafai [10] including a finite element simulation for complete three-dimensional vapor flow and liquid flow including non-Darcian effect. Studies in [9] and [10] did not include heat transfer analysis. Wang and Vafai [11] modeled the conduction heat transfer in the heat pipe container and wick structure in transverse direction for evaporation and

condensation regions. A second degree polynomial was assumed for the temperature distribution where the constants were derived using boundary conditions and an overall heat balance along the heat pipe. This analytical model was used to predict the transient performance for both the start-up and shutdown operations. The heat pipe container material was copper, while sintered copper powder was the wick material and water the working fluid. It was shown that the thermal diffusivity of the container and the wick dominated the time for heat transfer towards the inner side. The ambient heat transfer coefficient had a substantial effect where larger values decreased the time to reach steady state. The same heat pipe model was investigated by Vafai and Wang [5] experimentally and temperature distribution was measured. The temperature difference in the vapor domain was very small and therefore, it was taken as an average of the evaporation and condensation region end temperatures. Temperature on the outside surface of the container was measured and it was found that temperature along the condensation area was uniform, whereas the temperature in the evaporation region was approximately two degrees centigrade higher than the condensation area. The results also indicated that the porous wick of the evaporator section created the main thermal resistance resulting in the largest temperature drop.

Flat heat pipe with the asymmetrical boundary condition in [10, 5] was improved by Faghri and Xiao [12] by including the effect of three-dimensional heat conduction in the wall, fluid flow in the vapor chambers and porous wicks, and the coupled heat and mass transfer at the liquid–vapor interface. The governing equations for the container, wick and vapor cores were derived and solved by SIMPLE algorithm. For the vapor region compressible, and for the liquid region incompressible equations of motion were solved. At the liquid–vapor interface heat balance was used to find the phase change mass fluxes. It was shown that the vertical wicks improved heat pipe performance by increasing the capillary pressure. Parametric effects including the heat input and the axial length on the thermal and hydrodynamic behavior in the heat pipe were investigated.

It was explained that flat heat pipes with porous wick structure provide temperature flattening for multiple heat sources. Location of the heat source re-

gion/regions on the surface of the heat pipe result in a variation of evaporation and condensation regions according to the application. A simplified analytical thermal–fluid model including the container, liquid and vapor flows was developed for such a heat pipe with four different heating and cooling configurations by Aghvami and Faghri [13]. The configurations were; (i) single heat source and sink at top, (ii) multiple heat sources and sink at top, (iii) heat source at the bottom and heat sink on the top, (iv) multiple heat sources and sink positioned at both the top and bottom of the heat pipe. Two-dimensional steady heat conduction equation inside the container was solved to obtain the temperature distribution. Steady, laminar, incompressible flow in vapor and liquid regions was solved for the axial and transverse velocities and also for the axial pressure distribution. The results showed that evaporation and condensation are not confined to the heat source and heat sink regions due to the axial heat transfer in heat pipe container wall. Therefore, the assumptions that evaporation occurs only in the heat source region and that condensation occurs only in the heat sink region, are valid only if the thermal conductivity of the heat pipe container is very small.

The typical function of a heat pipe is the transfer of heat from a source to a sink whose locations are fixed. In space applications, however, source and sink positions can be changed for thermal management. Switching source and sink positions reverses the flow and heat transfer directions and this transient process was studied by Park *et al.* [14]. In this case a cylindrical heat pipe with a porous wick structure was analyzed using the transient, compressible, two-dimensional flow and heat transfer equations in the vapor region. Wick and container were included in the analysis in terms of heat transfer, where in the former an effective thermal conductivity of the wick was defined. Heat sources were defined as heat flux boundary conditions, whereas in the condensation region convection and radiation boundary conditions were used. Finite difference forms of the governing equations were solved using an in-house developed code. Transition time after switching the source and sink positions for convection and radiation boundary conditions were obtained.

Lefevre and Lallemand [15] studied an integrated flat heat pipe with several

electronic components and heat sinks. Two-dimensional flow model for both the liquid and the vapor flows were coupled to a three-dimensional thermal model in the heat pipe container. Constant heat flux was used as boundary condition at the heat source and heat sink regions. Convection heat transfer coefficient was defined at the outside surface of the heat pipe container. The temperature of the vapor phase was assumed to be constant and equal to saturation temperature. Liquid velocity was obtained using Darcy's law whereas the vapor velocity was obtained assuming the presence of a laminar incompressible flow between the two parallel plates. This model enabled the calculation of the proportion of the heat flux, which was conducted through the heat pipe container. It was shown that the maximum temperature difference was approximately three times higher when an equivalent thickness full copper plate was used for cooling. A similar model was analysed numerically by Sonan *et al.* [16] and the model was improved with the inclusion of transient effects. A transient three-dimensional thermal model was developed to define the transient heat transfer, both from the electronic components to the fluid and from the fluid to the condensers through the heat pipe container, which was used for the phase change at the container-wick interface. Electronic components were the heat sources, which were modeled by a constant heat flux boundary condition and the condensation regions were modeled by a convection heat transfer coefficient defined between the container and the surrounding ambient. In addition, a transient two-dimensional hydrodynamic model was developed to characterize the fluid flow in both the wick and the vapor core. The simulation was used in the problem of cooling of three electronic components of a starter generator. The time evolution of maximum temperatures over the electronic component were compared to that of an equivalent solid copper plate. The response time of the heat pipe was faster, however, it was seen that at maximum power dissipation, the temperature using the heat pipe was approximately 10°C higher than the copper plate. During the power descending phase, the maximum temperature with the heat pipe was about 20°C lower. However, using the heat pipe resulted in a lower temperature gradient and had lighter weight, which could be preferable in a system design.

Finite element method was applied by Thuchayapong *et al.* [17] to simulate two-

dimensional heat transfer and fluid flow at steady state in a heat pipe. The model included the vapor core, the wick, the container and the water jacket. The results were compared to experimentally obtained vapor and container temperature distributions of heat pipes with the copper–mesh wick. The results showed that the capillary pressure gradient inside the wick at the end of the evaporator section was large which might be attributed to fast liquid motion at the end of the evaporator section. It was shown that conduction heat transfer dominated in wick structure except the end of the evaporation section, where high liquid velocity provided efficient heat transfer through convection and resulted in a decrease in the wall temperature.

High heat flux values and the restrictions imposed on the size of heat sinks and fans, and on the noise level associated with the increased fan speed, necessitate enhanced CPU cooling techniques. Elnaggar *et al.* [18] simulated a finned U-shaped heat pipe using ANSYS-FLOTTRAN. The evaporation section was located at the bottom of U-shape in the horizontal position, but the rest constituted two finned condensation sections in the vertical position, requiring the effect of gravity to be accounted for. Two-dimensional heat and fluid flow equations were solved to determine appropriate ambient coolant velocity. The results were compared to experimentally measured container temperatures and coolant velocity, which were in good agreement.

Heat pipe model studied in [9] was used to investigate the performance improvement effect of nanoparticles in working fluid in by Bianco *et al.* [19]. Nano particles such as silver, gold, CuO, diamond, titanium, nickel oxide can be added to the working fluid, which change the thermal conductivity, viscosity and density of the fluid. The analytical model used in [9] was modified to include new working fluid properties. Different concentrations of Al<sub>2</sub>O<sub>3</sub>, CuO, and TiO<sub>2</sub> with diameters of 10, 20 and 40 nanometers were also investigated. It was shown that nanoparticles reduced thermal resistance of the heat pipe and the liquid velocity. Wick thickness and nanoparticle concentration levels were optimized to maximize the heat removal capacity.

### 1.3.2 Heat pipes with grooved wick structures

The concept of “micro” heat pipe was first introduced by Cotter [3] and it was defined as “one so small that the mean curvature of the liquid–vapor interface is comparable in magnitude to the reciprocal of the hydraulic radius of total flow channel”. Micro heat pipes do not have wick structure, but non circular channels serve as liquid arteries. This type of heat pipes also have a wide application area in electronics cooling, therefore they are investigated both mathematically and experimentally to understand the operating limitations and the effect of geometric parameters on their performance. Modeling of a heat pipe requires a coupled analysis of momentum transfer in the liquid and vapor domains along with the heat transfer analysis in heat pipe container. Phase change mass flow rates should be incorporated in both conservation of mass and energy over the whole domain. Therefore, different mathematical approaches were used for modeling. Generally the analyses are not complicated compared to those heat pipes with homogeneous wick structure and simplified numerical and analytical analyses were performed to understand the overall behavior. Some examples from the previous studies will be summarized in the following section, where simple to detailed mathematical modeling approach used in the literature will be addressed.

The basic assumption in the momentum model is that the flow is steady, unidirectional and incompressible both in the liquid and vapor domains. Total heat input from the external boundary is used for phase change and conduction in the heat pipe container is neglected due to the high thermal conductivity of the solid compared to the working fluid. Capillary pressure in the liquid domain is introduced using Young–Laplace equation and the liquid–vapor interface radius variation along the heat pipe axis is also obtained using this relation. This general approach was used by Babin and Peterson [3] to understand the operating characteristics, where the cross-section of the heat pipe was rectangular but the internal incurved geometry formed corners which were modeled as triangular grooves serving as liquid arteries. Capillary limit was the dominant operating limitation as is the case for other heat pipes, therefore capillary pressure should

overcome the pressure losses in the vapor, liquid regions and the hydrostatic pressure drop. An analytical relation was obtained for total pressure drop and equalized to capillary pressure to obtain the dry-out limit and maximum heat transfer capacity. The temperature of the heat pipe container was measured experimentally and maximum temperature change region was defined as the beginning of the dry-out region and the analytical results were compared to experiments.

Micro heat pipes with different cross-sections utilize sharp corners for liquid feed to the evaporation region. These corners can be modeled as triangular grooves, therefore studies generally concentrate on micro heat pipes having triangular or V-shaped grooves. Peterson and Ma [20] and Khrustalev and Faghri [21] studied heat transfer capacity of grooves with triangular geometry. Momentum equations in both liquid and vapor regions were solved using available correlations. The studies took liquid–vapor interfacial shear stress into account and it was shown that neglecting the shear stress at the free surface of the liquid due to vapor–liquid frictional interaction could lead to an overestimation of the maximum heat transfer capacity. Energy equation was introduced in the problem where the axial change in mass flow rate was found due to evaporation and condensation as mentioned in basic assumptions above in [20]. However, Khrustalev and Faghri [21] performed a more detailed analysis, where condensation and evaporation heat transfer rates were calculated by solving liquid film thicknesses and conduction through micro liquid regions. The variation of liquid–vapor interface along heat pipe axis, maximum heat capacity, pressure drops in liquid and vapor regions were obtained. It was shown that as the inclination angle and the length of the heat pipe increased, the heat transport capacity decreased. However, decreasing apex angle of the triangle increased the heat transport capacity of the heat pipe.

V-shaped groove was modeled by Kumar and Dasgupta [22] where a more detailed evaporation model was applied to obtain evaporation mass flow rates in transition and meniscus regions and results were reported for different heat input values. In this study, heat balance at macro level was written for a unit liquid volume, where the difference between the inflow and evaporation heat transfer

was used to increase the liquid temperature axially. The change of the liquid–vapor interface radius was investigated for different values of heat input. The effects of inclination and apex angle on the heat capacity of the heat pipe were studied. The decrease in apex angle resulted in an increased liquid–vapor interface radius change and hence improved capillary pumping, resulting in higher heat transfer capacity.

Suman and DasGupta [23] generalized the fluid flow model for any arbitrary (polygonal) shaped groove. However, the detailed evaporation mass transfer model given in [22] was not used in this study. In addition, macro level heat balance for a unit liquid volume did not consider the axial temperature distribution. The numerical model used in the solutions of grooved heat pipes with triangular and rectangular cross-sectional geometries. In this case, the axial variation of liquid–vapor interface radius was used to predict the onset of the dry-out point and the propagation of the dry-out length, where the minimum value of the radius at the end of the evaporation region is defined by the contact angle and the geometry of the cross-section. It was shown that triangular heat pipes have higher heat carrying capacity with respect to rectangular ones. Similar analysis was conducted by Suman and Hoda [24], where the effect of contact angle, surface tension and viscosity of the working fluid, inclination, apex angle of V-groove, length of adiabatic section on the heat removal capacity of the heat pipe were studied.

The modeling approach in [23] was extended to include the transient effects by Suman *et al.* [25]. The triangular micro-heat pipe was taken as a test case. The coupled equations of heat, mass and momentum transfer were solved to obtain the transient as well as the steady state profiles of temperature. It was shown that higher heat input required more time to reach steady state.

Experiments were carried out to study the onset and propagation of dry-out point on a silicon surface with V-shaped grooves where pentane was used as the working fluid by Anand *et al.* [26]. The axial temperature distribution was accurately measured as a function of the heat input and inclination without the working fluid in the heat pipe. Since no working fluid at dry-out point was

present, the temperature distribution during the operation of the heat pipe was compared to the measured temperature without the working fluid. Where these two temperatures coincide, it was noticed that dry-out point was reached. The problem was also solved numerically using an approach similar to [23] to predict the onset, location and propagation of the dry-out point. The results showed that by increasing inclination angle and heat input, dry-out point propagated away from the heat input region.

Shear stress at the liquid–vapor interface contributes to the increase of the liquid pressure drop and decreases the heat transfer capacity of the heat pipe. Generally, heat pipe analysis uses predefined correlations to include this effect. Thomas *et al.* [27] studied fully developed laminar flow for one cross-section in a trapezoidal groove. A correlation for shear stress was defined in terms of Poiseuille number ( $f \cdot Re$ ) as a function of groove aspect ratio, groove half angle and liquid contact angle. A semi-analytical solution for capillary limit was obtained.

Launay *et al.* [28] developed a mathematical model for predicting the heat transport capacity and temperature distribution along the axial direction of a triangular heat pipe, filled with water. A detailed evaporation and condensation model from kinetic theory was utilized and film thickness along evaporation and condensation micro regions were obtained, which were used to calculate thermal resistance and the heat transfer rate through the liquid film. An iterative procedure in terms of vapor temperature was applied, where heat transferred from the condensation region became equal to the defined heat input at the evaporation region. In this study heat pipe container temperature was also obtained using detailed evaporation and condensation models. Ratios of heat transferred in the evaporator and condenser regions showed that the geometry of the micro region could be altered to increase the heat removal capacity of the heat pipe. The velocity, pressure, and temperature distributions in the vapor and liquid phases were calculated. Fluid fill charge effect on heat pipe heat removal capacity was predicted and it was shown that fill ratio should be optimized to obtain maximum heat removal capacity for a given heat input.

One of the features of heat pipes is that they can operate at any inclination either in a favorable configuration, where the condensation side is at a higher level than the evaporation side; or unfavorable configuration, where the condensation side is at a lower level than the evaporation side. The effect of gravity on a triangular grooved heat pipe was studied by Hung and Tio [29] for both favorable and unfavorable configurations. In addition to the previous studies, heat transfer in heat pipe container was included in the study and the ratios of the conduction heat transfer to the phase change heat transfer were presented for different inclination angles. A one-dimensional, steady, simplified model was developed for momentum and mass balance. A heat balance model was developed from first principles in which heat input from evaporation side was equated to the axial solid conduction and convection heat transfer at solid–liquid interface, which was used for evaporation heat transfer. It was shown that for a particular operating temperature, the heat transport capacity increased with the angle of inclination at favorable configuration, but the converse was true for unfavorable configuration. The order of the ratio of solid conduction heat transfer to phase change heat transfer was about 0.01, however, both heat transfer rates increased for favorable configuration. It was observed that the heat pipe container temperature difference between evaporation and condensation sides decreased for the unfavorable configuration. Another result shown was that higher operating temperatures induced a larger temperature difference for both configurations. The same mathematical approach was used by Chang and Hung in [30] to study the effect of different heat pipe container materials and working fluids. The coupled effect of working fluid and solid wall was quantified by deriving a new non-dimensional parameter and the values of this parameter were presented for different operating temperatures.

Previous studies about triangular micro heat pipes consider solid–liquid contact angle to be a constant along the heat pipe. The effect of variable contact angle distribution along a triangular heat pipe on the thermal performance was analyzed based on a one-dimensional steady-state model by Qu *et al.* [31]. The unidirectional flow model was used, where the contact angle was defined in momentum equation in term of geometric coefficient. The results showed that micro

heat pipe with variable contact angle could remove a larger amount of heat for a given heat input. Increased thermal performance could be attributed to the increase in the liquid capillary force, however, it was observed that there was no perceptible increase in the liquid shear force.

Grooved heat pipes with different cross-section profiles were also investigated such as  $\Omega$ -shaped [32] or dual cored trapezoidal grooved [33] and trapezoidal grooved [34] cylindrical heat pipes.

A theoretical model of fluid flow and heat transfer with axial  $\Omega$ -shaped grooves was studied for maximum heat transport capability by Chen *et al.* [32]. The influence of variations in the liquid–vapor interface radius, interfacial shear stress and the contact angle were considered. The axial distribution of the liquid–vapor interface radius, fluid pressure and mean velocity were obtained where the accuracy of the developed model was verified by experimental data.

Among the heat pipes with different wick structures like wire mesh, arteries, foams, axial grooves, and porous materials, axially grooved heat pipes are proven to be reliable for long-life spacecraft missions. Dual core axially trapezoidal grooved aluminum heat pipe using ethane as working fluid was chosen for satellite thermal control by Anand *et al.* [33]. Flow equations for liquid and vapor cores were considered for maximum heat transport capacity and the results of the analysis were also verified by experimental study.

A mathematical model for heat and mass transfer in a cylindrical heat pipe with trapezoidal grooved structure was solved analytically by Kim *et al.* [34]. The effects of the liquid–vapor interfacial shear stress, contact angle, and the amount of initial liquid charge were considered in the proposed model. Modified Shah method was suggested and validated for liquid–vapor interfacial shear. For the heat transfer equation, thermal resistances in solid and liquid regions, simplified models for evaporation and condensation by defining effective heat transfer coefficients were used. Analytical results for the maximum heat transport rate and total thermal resistance were shown to be in close agreement with the experimental results.

Viscous losses in grooved heat pipes limit the heat transport capacity, which is less than that of a homogeneous wicked heat pipe. The electrohydrodynamic (EHD) pumping offers a promise to improve the capacity with a smaller size, which is a concern whenever size limitation is imposed. The EHD phenomenon involves the interaction of the electrical field and the flow field in a dielectric fluid medium. This interaction can result in electrically induced fluid motion that is caused by an electrical body force. V-grooved micro heat pipe was studied by Suman [35], where an electrical body force was added in the momentum equation of the working fluid. Analytical expressions for the critical heat input and dry-out lengths were obtained, which showed that the critical heat input increased and the dry-out length decreased with increasing applied electrical field.

Theoretical modeling of a triangular micro-heat pipe showed that the heat transport capacity increases when the channel apex angle and the length of the micro-heat pipe decreases. Star-grooved heat pipes obtain the desired corner apex angle without affecting the number of corners, therefore, under identical operating conditions star-grooved micro-heat pipe reveal better performance. The study by Hung and Seng [36] considered a one-dimensional, steady-state mathematical model, where the continuity, momentum, and energy equations of the liquid and vapor phases, together with the Young–Laplace equation, were solved numerically to yield the heat and fluid flow characteristics of the micro heat pipe.

Chauris *et al.* [37] analyzed a flat heat pipe, where lower, upper and vertical sides contain triangular grooves, whereas the intersection between horizontal and vertical sides were combined through droplet shaped grooves at the corners. Simple mathematical models for momentum model and mass balance were used and heat input was used to find liquid–vapor interface velocity. Different working fluids were studied to investigate dry-out length as a function of working temperatures.

Flat heat pipes having rectangular groove arrays were investigated by various authors [38, 39]. A mathematical model was developed for predicting the thermal performance of a flat micro heat pipe with a rectangular groove by Do *et al.*

[38]. Generally, heat pipe calculations were carried out with the following assumptions: (i) evaporation and condensation were assumed to occur uniformly in the axial direction; (ii) neither evaporation nor condensation occurred in the adiabatic section inside the heat pipe; (iii) the container temperature was either assumed to be constant or its variation was neglected. These simplifying assumptions had good applicability to small heat pipes, whereas experiments showed a temperature drop of 25°C for a length of 120 mm. This suggested that the axial variation of the container temperature and the evaporation and condensation rates should be taken into consideration. Therefore, the axial variation of the container temperature was accounted for in the energy balance equation. The evaporation and condensation mass flow rates were calculated from the relations obtained from kinetic theory and conduction through the liquid region. The effects of the liquid–vapor interfacial shear stress, contact angle, and the amount of liquid charge were included in this model. Numerical results were found to be in good agreement with those given in [40]. Finally, the grooved wick structure was optimized for maximum heat transport rate as a function of the width and the height of the groove.

Two-phase heat spreaders with rectangular grooves have a high evaporation area compared to the condensation area. A one-dimensional two-phase flow model was developed for such a heat spreader in horizontal orientation by Rulliere *et al.* [41]. A confocal microscope was used to measure the liquid–vapor interface radius along the groove. The measurements were compared to the results of fluid flow model based on mass and momentum balance and the Young–Laplace equation. Container temperatures were measured with three different working fluids, namely water, *n*-pentane and methanol. The experimental results were found to be in good agreement with the calculated liquid–vapor interface radii that were obtained without considering interfacial shear stress, since vapor cross section was larger than liquid cross section in this heat pipe. A similar analysis was performed by Lefevre *et al.* [6], where the heat conduction in each cross section in liquid and solid regions was solved to obtain the thermal resistance, which was used to find the axial temperature distribution along the heat pipe container. The results were validated in experiments, in which liquid–vapor

interface radius and container temperatures were measured. An optimization study was carried out for maximum heat capacity as a function of groove height and width. The effect of filling ratio and the vapor space thickness on thermal performance was investigated in a numerical and experimental study by Lips *et al.* [42]. It was shown that small vapor space induced liquid retention and thus reduced the thermal resistance of the system, however, it influenced the level of the liquid–vapor interface radii and hence reduced the maximum capillary pressure. As a result, it had to be carefully optimized to improve performance. In all the cases, the optimum filling was in the range one to two times the total volume of the grooves. An experiment conducted in non-horizontal position showed that the presence of nucleate boiling in the system did not constitute a limit but dry-out of the evaporator occurred due to the capillary limit [43].

In grooved heat pipes heat source and heat sink regions are located at the opposite ends of the heat pipe. Gillot *et al.* [39] investigated a flat heat pipe, where rectangular grooves were positioned circumferentially around the central vapor core region. Heat source and sink were also placed asymmetrically, where a heat source was located at the top middle and the two sides of the top, whereas the bottom side served as the heat sink region. Two vertical grooves at both ends provided liquid flow to the evaporation region. Analytical solution for liquid and vapor flow was used to obtain total pressure drop and capillary limit, and heat transfer in heat pipe container and working fluid was modeled by conduction using equivalent thermal conductivity. The results were compared to experimental results obtained for brass and silicon heat pipes [39, 44]. This study showed that grooved heat pipes can be used as heat spreaders similar to the ones with homogeneous wick structure.

### **1.3.3 Heat pipes with combined grooved and porous wick structure**

Heat pipes with axial grooves are easy to manufacture, however, they generally provide one dimensional heat transfer, on the other hand heat pipes with porous wick structure operate with increased flow resistance. To improve the heat transfer capacity and provide a more homogeneous temperature distribu-

tion in any direction some novel design prototypes were proposed and studied. One example is the heat pipe produced and investigated both analytically and experimentally by Wang and Peterson [45]. Copper screen mesh was used as the primary wicking structure, in conjunction with a series of parallel wires, which formed liquid arteries where water was selected as the working fluid. Capillary, boiling, entrainment limitations were investigated through empirical relations considering heat input and geometric parameters. Two prototypes were tested experimentally and maximum heat removal capacity results were found to be in good agreement with empirical results. Increasing the wire diameter resulted in an increase in the maximum heat transport capacity. The mesh number had conflicting effects on the capillary pumping capacity and the frictional pressure drop, *i.e.* increasing mesh number provided higher capillary force, however, also resulted in higher pressure drop. Therefore, optimum design parameters should be searched for a specific operating temperature. Similar to the mesh number, the wick thickness had an opposing effect on the capillary and boiling heat transfer. As the wick thickness increased liquid pressure drop decreased due to larger area, but it reduced boiling limit, where the liquid was easily superheated. The inclination angle had a dominant effect on the maximum heat transfer capacity, as the heat transport capacity decreased with increasing inclination angle.

Rectangular grooved flat heat pipe mentioned in [38] was extended by Do and Jang [46] by adding water-based  $\text{Al}_2\text{O}_3$  nanofluids as the working fluid. The nanoparticles increased thermal conductivity of the working fluid, but also accumulated on the heat transfer surface in the evaporation region. This porous layer enhanced evaporation heat transfer and the driving capillary force. Axial momentum equations in the liquid and vapor were solved, where effective density and viscosity values were defined by considering the volume fraction of nanoparticles. Evaporation and condensation mass fluxes for each cross-section along the heat pipe axis were calculated by the relations obtained from kinetic theory, where the thermal conductivity of the liquid was recalculated due to the addition of nanoparticles. Due to nanoparticle coating in evaporation region, one additional relation from kinetic theory and Darcy's law was obtained for the evaporation region on the fin top. The effects of the volume fraction and

the size of nanoparticles on the thermal performance were studied, where results showed that adding less than 1% nanofluids enhanced thermal performance up to 100%.

#### **1.4 Description of the Current Study**

As summarized in the previous section, numerous studies have been performed on heat pipes to compute the maximum heat removal capacity and get an insight to the physical mechanisms involved. The effects of the physical and geometrical parameters (groove size, contact angle, shear force at the liquid–vapor interface) were investigated for geometries with different cross section. For flat heat pipes with porous wick, detailed analyses were performed for momentum equation both in liquid and vapor regions and heat transfer in the container. For grooved micro heat pipes the analyses were less detailed, simplifying assumptions and pre-defined correlations for solid–liquid and liquid–vapor interface shear stresses were used. Temperature distribution along the heat pipe container was not considered generally and evaporation and condensation mass flow rates correlated through heat input to the evaporator. Studies on flat grooved heat pipes with rectangular cross-section included axial temperature distribution through the heat transfer equation in the heat pipe container and working fluid by defining thermal resistances and using electrical analogy. Evaporation and condensation mass fluxes were found from correlations available in the literature or defined heat transfer coefficient at the liquid–vapor interface.

In the present study a flat micro heat pipe with rectangular cross section is investigated. Three dimensional heat transfer equation both in the heat pipe container, solid domain, and in the working fluid, liquid domain, is solved, which is coupled to the evaporation and condensation models at the liquid–vapor interface. Evaporation and condensation models are used to define the liquid film thickness along the micro region, which is used to find the phase change mass fluxes at each cross-section along the heat pipe. The details of the modeling will be presented in Chapter II.

The shape of the interface between liquid and vapor is not known *a priori* and each cross-section is assumed to be circular. Since the physical domain is irregular in the liquid domain, a coordinate transformation is made and a transformed form of the heat transfer equation is obtained for a fixed rectangular computational domain, which is used in the numerical solution. Heat transfer equation in the liquid domain includes the effect of convective heat transfer, which is generally neglected and the effect of the convection on heat pipe performance is investigated.

The axial flow is modeled as a one dimensional incompressible flow where the averaged velocity is used at each cross section. Shear force between solid–liquid interface is defined by an empirical relation. Young–Laplace equation is used to correlate surface tension and the liquid–vapor interface radius to pressure drop in the liquid domain.

The details of the solution methodology will be explained in Chapter III. Chapter IV includes validation of the current model with the results of Lefevre *et al.* [6] as well as a parametric study considering the effect of the dimensions of the heat pipe geometry and boundary conditions on the heat removal capacity of the heat pipe. A sample problem simulating cooling of an electronic component is solved in Chapter V to design a heat pipe with a given set of design objectives and restrictions.

## CHAPTER 2

### PHASE CHANGE

Heat pipes take advantage of phase change heat transfer to remove large amounts of heat in small areas with small temperature differences. Evaporation and condensation modeling is a major area of interest in heat pipe research and a detailed explanation of evaporation and condensation modeling will be given in this chapter and the comparison of the present model with the previous studies will be presented.

#### 2.1 Evaporation Modeling

Evaporation is a surface phenomenon, where the liquid molecules with sufficient energy to overcome intermolecular forces at the liquid–vapor interface escape from the bulk liquid region and change state to gaseous phase. If evaporation takes place in an enclosed area, the escaping molecules accumulate as a vapor above the liquid and many of the molecules return to the liquid. When the process of escape and return reaches equilibrium, the vapor state is “saturated”. For a system consisting of vapor and liquid of a pure substance, this equilibrium state is related to the vapor pressure by the Clausius–Clapeyron relation,

$$\ln \left( \frac{P_2}{P_1} \right) = -\frac{h_{lv}}{R_u} \left( \frac{1}{T_2} - \frac{1}{T_1} \right), \quad (2.1)$$

where  $P_1$  and  $P_2$  are vapor pressures at temperatures  $T_1$  and  $T_2$ ,  $R_u$  the universal gas constant and  $h_{lv}$  the latent heat of evaporation.

At the liquid–vapor interface the conservation of mass, momentum and energy should be satisfied. Momentum equation at the interface reduces to Young–Laplace equation, since the momentum terms due to interface motion are small,

$$P_l - P_v = \frac{\sigma}{R}, \quad (2.2)$$

where  $R$  is the radius at the liquid–vapor interface and  $\sigma$  is the surface tension of the liquid. The definition of the capillary pressure was given in Equation 1.1 by two principal radii of liquid–vapor interface, however, the radius in axial direction is very large compared to the one along the groove cross-section and it's contribution is neglected in Equation 2.2.

Conservation of energy at the interface requires

$$q_l'' - q_v'' = m_e'' h_{lv} \quad (2.3)$$

where  $q_l''$  and  $q_v''$  are heat fluxes at liquid and vapor sides and  $m_e''$  is evaporation mass flux at the interface.

When the evaporator section of a grooved heat pipe is analyzed, three subregions of the evaporating film section can be observed (Figure 2.1).

- the adsorbed film/non-evaporating region, where the liquid layer is thin, of the order of a fraction of nanometers and remains constant. There is no mass transfer, since intermolecular interactions between the wall and the liquid–vapor interface dominate,
- evaporating thin film region, where both the intermolecular and capillary forces are dominant,
- meniscus/macro region, where intermolecular forces are negligible, and the curvature of the interface becomes constant. In this zone, the liquid layer is too thick to be influenced by the liquid–solid interactions. The equilibrium is mainly governed by the capillary forces.

The first two regions are called the “micro-region” which forms a very small portion of the global meniscus. However, this region is characterized by high heat transfer rates due to the very low resistance to heat transfer across the liquid film. It was shown that liquid–vapor interface curvature is not constant

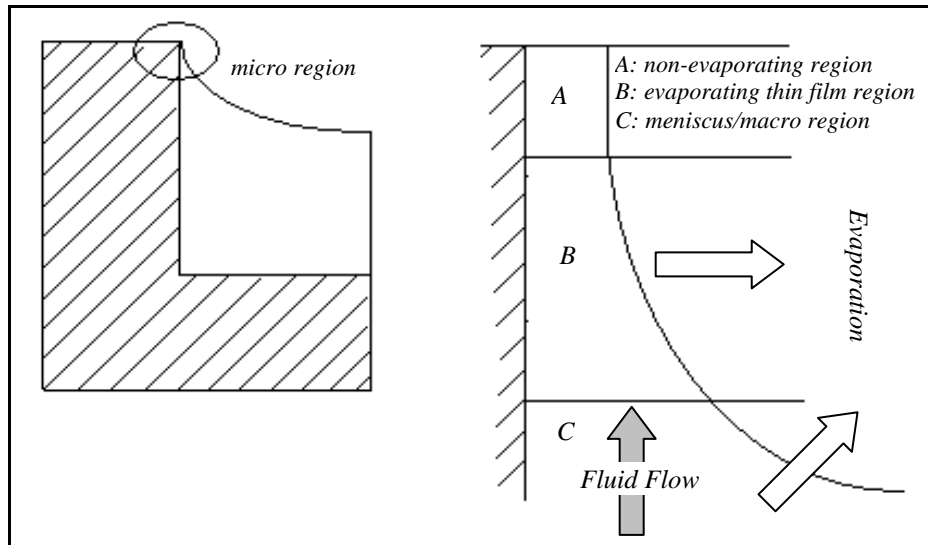


Figure 2.1: Evaporation micro region and subregions

and the interface temperature is greater than the saturation temperature in the micro region [47]. Transverse pressure gradient in liquid phase results in large curvatures in this region, which decrease the volatility of the liquid and increases the interface temperature above the saturation temperature.

The coordinate system used for the micro region evaporation model is given in Figure 2.2. The origin of the coordinate system is placed at the interface between the evaporating thin film region and meniscus regions. The axial direction,  $s$ , extends to the non-evaporating region and transverse direction,  $n$ , extends from the liquid to vapor phase.

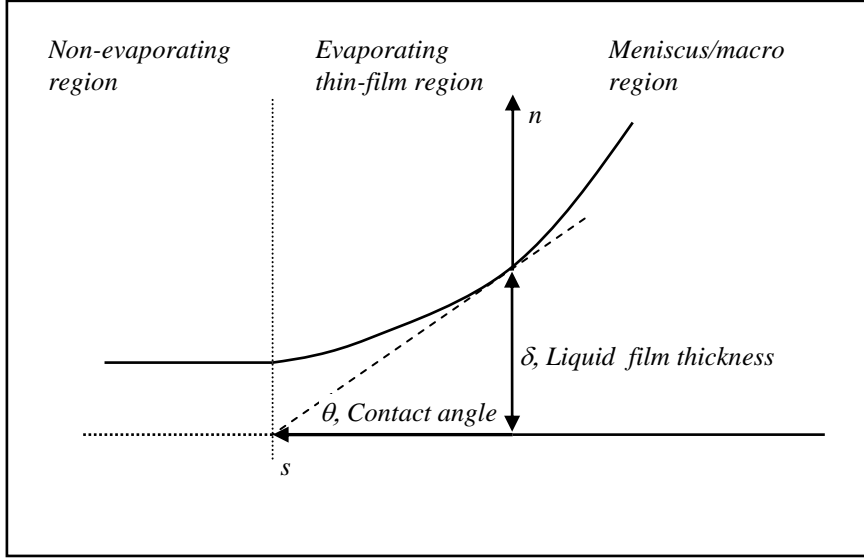


Figure 2.2: Coordinate system used in the evaporating region

The liquid flow in the axial direction compensates the evaporation mass flux from thin film region as shown in Figure 2.1. Evaporation mass flux in the evaporating thin film region can be defined from kinetic theory as in Equation 2.4,

$$m_e'' = a(T_{lv} - T_v) + b(P_l - P_v), \quad (2.4)$$

where

$$a = \frac{2c}{2-c} \left( \frac{M}{2\pi R_u T_{lv}} \right)^{1/2} \left( \frac{M P_v h_{lv}}{R_u T_v T_{lv}} \right), \quad (2.4a)$$

$$b = \frac{2c}{2-c} \left( \frac{M}{2\pi R_u T_{lv}} \right)^{1/2} \left( \frac{P_v V_l}{R_u T_{lv}} \right), \quad (2.4b)$$

where  $c$  is the accommodation coefficient,  $h_{lv}$  is the latent heat of evaporation,  $M$  is the molecular weight,  $R_u$  universal gas constant,  $V$  molar volume of liquid

phase,  $P_v$  vapor pressure,  $P_l$  liquid pressure,  $T_v$  vapor temperature, and  $T_{lv}$  liquid–vapor interface temperature.

There are two contributions to the pressure difference between the liquid and vapor phases, which are due to the effects of dispersion and surface tension as represented in Figure 2.3.

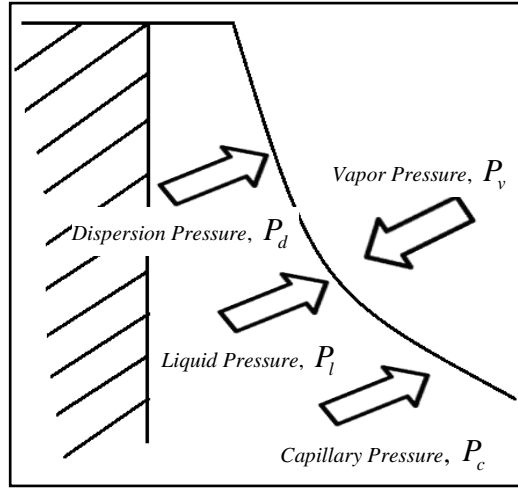


Figure 2.3: Pressure balance at the liquid–vapor interface

Dispersion pressure in the micro region comprises several components which include the molecular component, electrostatic component (existing in ionic solutions) and structural component which is related to the formation of the hydration layers of polar molecules near interfaces [48]. For a non-polar liquid, the dispersion pressure can be expressed as,

$$P_d = \frac{A_d}{\delta^3}, \quad (2.5)$$

where  $P_d$ , is the dispersion constant and,  $\delta$ , is the liquid film thickness. For polar

liquids like water and aqueous solutions logarithmic functions from experimental studies are also used to represent the dispersion pressure.

Capillary pressure is defined in terms of curvature of the liquid–vapor interface (Equation 2.6).

$$P_c = \sigma \frac{d^2\delta/ds^2}{(1 + (d\delta/ds)^2)^{3/2}} \quad (2.6)$$

The difference between the vapor and liquid pressures is balanced by the dispersion and capillary pressures at the interface,

$$P_v - P_l = P_d + P_c. \quad (2.7)$$

By differentiating Equation 2.7 with respect to  $s$ , which is the coordinate defined from the meniscus region to the non-evaporating region (Figure 2.2), the variation of liquid pressure in terms of liquid film thickness,  $\delta$ , is obtained assuming that the vapor pressure is constant.

$$\frac{dP_l}{ds} - \frac{3A_d}{\delta^4} \frac{d\delta}{ds} + \sigma \frac{d^3\delta/ds^3}{(1 + (d\delta/ds)^2)^{3/2}} - 3\sigma \frac{(d^2\delta/ds^2)^2}{((1 + (d\delta/ds)^2)^{5/2})} \frac{d\delta}{ds} \quad (2.8)$$

The liquid feed from the “macro region” can be formulated as a fully developed one-dimensional flow in the  $s$ -direction as given in Equation 2.9,

$$\frac{dP_l}{ds} = \mu \frac{d^2u_l}{dn^2}, \quad (2.9)$$

subject to the boundary conditions,

$$du_l/dn = 0 \quad \text{at} \quad n = \delta, \quad (2.9a)$$

$$u_l = 0 \quad \text{at} \quad n = 0, \quad (2.9b)$$

Mass flow rate at each cross section can be obtained through the integration,

$$m'_e = \rho_l \int_0^\delta u_l \, dn \quad (2.10)$$

Differentiating Equation 2.10 with respect to  $s$  and combining with Equation 2.8 the mass flux along the direction of flow,  $m_e''$ , becomes,

$$-\frac{d}{ds} \left( \frac{\delta^3}{3\nu} - \left( \frac{3A_d d\delta}{\delta^4 ds} + \sigma \frac{d^3\delta/ds^3}{(1 + (d\delta/ds)^2)^{3/2}} - 3\sigma \frac{(d^2\delta/ds^2)^2}{(1 + (d\delta/ds)^2)^{5/2}} \frac{d\delta}{ds} \right) \right) \quad (2.11)$$

Evaporation mass flux can be obtained from Equation 2.4, however as mentioned before liquid–vapor interface temperature is higher than the saturation temperature and is also an unknown. Therefore, the heat flux between liquid–vapor interface and heat pipe wall is used to define the interface temperature.

$$m_e'' = a(T_{lv} - T_v) + b(P_l - P_v) = k_l \frac{T_w - T_{lv}}{\delta h_{lv}} \quad (2.12)$$

$$T_{lv} = \frac{k_l T_w / \delta h_{lv} + a T_v + b(P_v - P_l)}{a + k_l / \delta h_{lv}} \quad (2.13)$$

Evaporation mass flux is written in terms of the heat pipe wall temperature, so Equation 2.4 becomes

$$m_e'' = \frac{a(T_w - T_v) + b(P_l - P_v)}{1 + a\delta h_{lv}/k_l} \quad (2.14)$$

Equations 2.11 and 2.14 are rearranged to give Equation 2.15 and integrated to obtain the liquid film thickness and evaporation mass flux at each cross section of the micro region.

$$\begin{aligned} \frac{d}{ds} \left( \frac{\delta^3}{3\nu} - \left( \frac{3A_d d\delta}{\delta^4 ds} + \sigma \frac{d^3\delta/ds^3}{(1 + (d\delta/ds)^2)^{3/2}} - 3\sigma \frac{(d^2\delta/ds^2)^2}{(1 + (d\delta/ds)^2)^{5/2}} \frac{d\delta}{ds} \right) \right) \\ = -\frac{a(T_w - T_v) + b(P_l - P_v)}{1 + a\delta h_{lv}/k_l} \end{aligned} \quad (2.15)$$

subject to following boundary conditions.

$$\delta = \delta_0 \quad \text{at} \quad s = 0, \quad (2.15a)$$

$$d\delta/ds = -\tan\theta \quad \text{at } s = 0, \quad (2.15b)$$

$$P_v - P_l = \sigma/R \quad \text{at } s = 0, \quad (2.15c)$$

$$d(P_v - P_l)/ds = 0 \quad \text{at } s = 0, \quad (2.15d)$$

$$m_e'' = 0 \quad \text{at } s = l. \quad (2.15e)$$

Since the total length of the evaporating region is not known *a priori*, one additional condition should be introduced to find the length,  $l$ , defined in Equation 2.15.e.

Assuming that dispersion pressure is  $1/100000^{th}$  of the capillary pressure at the beginning of the coordinate system, *i.e.*  $s = 0$ ,

$$P_d = \frac{\sigma}{R}10^{-5} = \frac{A_d}{\delta_0^3} \quad (2.16)$$

the initial value of the liquid film thickness,  $\delta_0$ , can be found.

The heat transfer in micro grooves and heat pipes were investigated by several authors to find out the evaporating heat transfer coefficient and the effect of the physical and geometric parameters on evaporation heat transfer performance. Stephan and Busse [47] modeled the evaporator section of a trapezoidal grooved heat pipe. The study shows that the liquid–vapor interface temperature is higher than the saturation temperature. In this study, liquid film thickness, interface temperature and heat flux variation along the micro region were calculated and the ratio of micro region evaporation heat transfer to the liquid meniscus region was also reported. A similar analysis was performed by Bertossi [49] and different working fluids were compared in terms of micro region evaporation rates. The definition of micro region can be different according to the assumptions and related boundary conditions to formulate the micro region evaporation. Du and Zhao [48] studied the problem by defining a new boundary condition and compared their results to the previous studies. A mathematical model was developed by Jiao *et al.* [50] to investigate the effect of thin film evaporation on the maximum heat capacity of a trapezoidal micro-grooved heat pipe. The effect of the contact angle on meniscus radius, heat transfer rate and micro region

length was investigated. It was shown that contact angle increase results in a nonlinear increase in the meniscus radius and a decrease in the length of the micro region. This results in a decrease in the heat transfer capacity through the micro region. A similar model was developed by Cheng *et al.* [51] to determine the heat transfer through both the thin-film and liquid meniscus regions in a rectangular microgroove. In the liquid meniscus region two-dimensional steady heat conduction equation was solved analytically to determine the heat transfer rate. It was shown that the contribution of heat transfer through the liquid meniscus region depended on the contact angle and solid wall superheat. Present study, where the details were explained in the previous paragraphs, is compared to the results of [47] in terms of liquid film thicknesses and heat fluxes in the micro region. The working fluid in [47] was ammonia and other physical parameters used in the analysis are given in Table 2.1

Table 2.1: Physical parameters used in evaporation model

Vapor temperature (K)	$T_v$	300
Vapor pressure (Pa)	$P_v$	$1.06 \times 10^5$
Latent heat of evaporation (J/kg)	$h_{lv}$	$1.18 \times 10^{-6}$
Density of liquid (kg/m <sup>3</sup> )	$\rho$	600
Surface tension (N/m)	$\sigma$	$2.0 \times 10^{-2}$
Thermal conductivity (W/m · K)	$k_l$	0.48
Molar mass of liquid (kg/mol)	$M$	$17.3 \times 10^{-3}$
Molar volume of liquid (m <sup>3</sup> /mol)	$V_l$	$28.8 \times 10^{-6}$
Accommodation coefficient	$c$	1
Dispersion constant (J)	$A_d$	$2.0 \times 10^{-21}$
Interface radius (m)	$R$	$909 \times 10^{-6}$

Film thickness variation along the micro region is shown in Figure 2.4. There is a 5% difference between the present study and the results of Stephan and Busse

[47]. Heat flux variation is given in Figure 2.5, where the maximum value of both results coincide. It is given in [47] that the overall heat transfer in a span of  $1\mu\text{m}$  region is  $6.6\text{ W}$ , whose value in the present study is  $7.52\text{ W}$ .

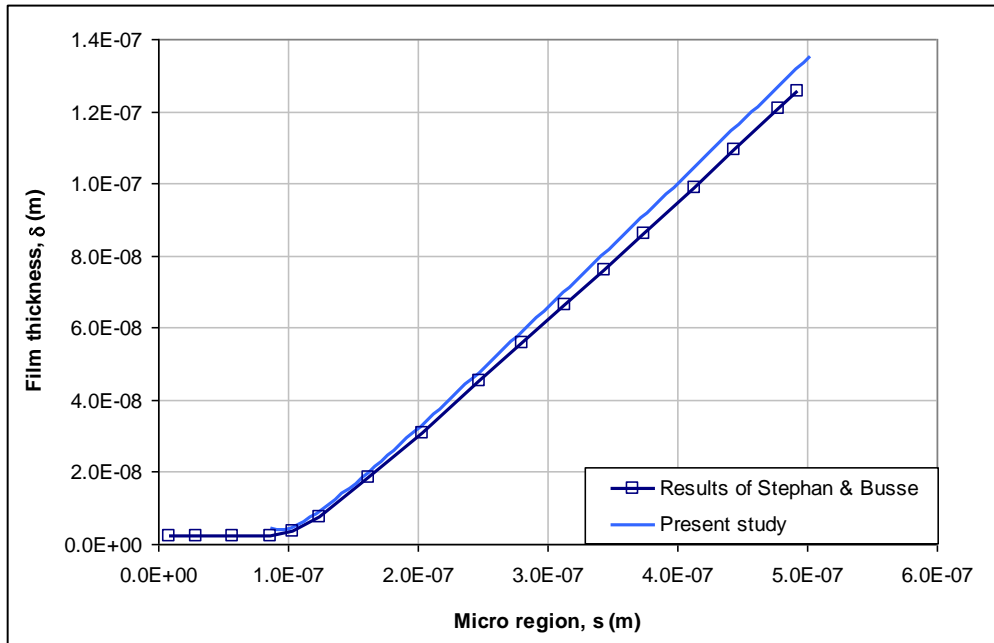


Figure 2.4: Liquid film thickness variation along the micro region

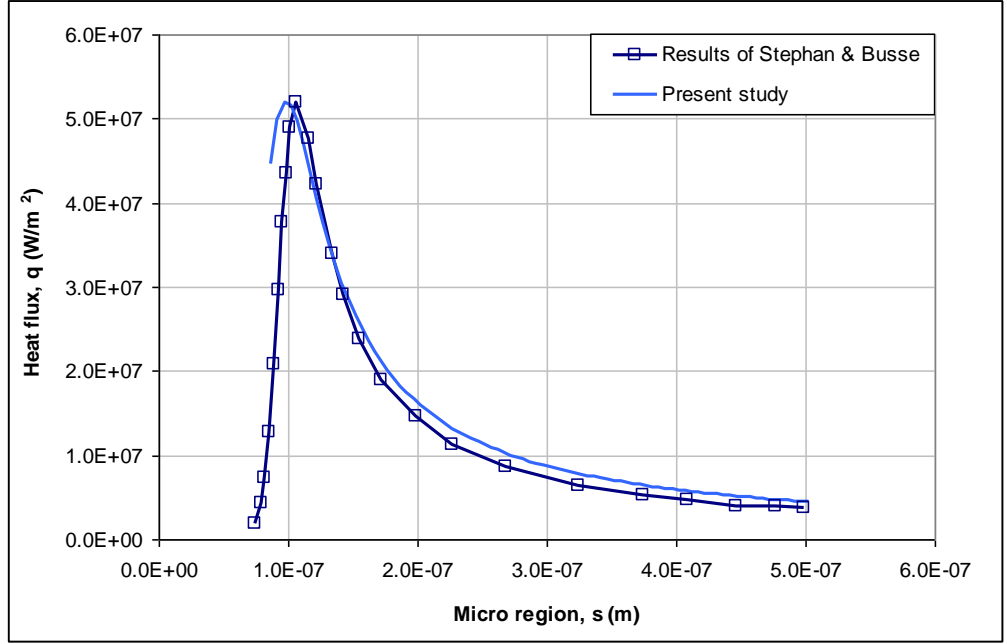


Figure 2.5: Heat flux variation along the micro region

## 2.2 Condensation Modeling

Condensation is the change of the state from gaseous phase into liquid phase, and is the reverse of evaporation. Most of the condensation occurs at the top of the fin, which can be defined as the “micro region” for condensation. A schematic of the condensation on the top of the fin is represented in Figure 2.6. Condensation mass flux is defined in a way similar to the evaporation mass flux using kinetic theory. However, in this case dispersion pressure in the liquid region is neglected. Equation 2.15 given for evaporation is rewritten for condensation in the following form,

$$\frac{\sigma}{3\nu} \frac{d}{ds} \left( \delta^3 \frac{d^3 \delta}{ds^3} \right) = - \frac{a(T_w - T_v) + b(P_l - P_v)}{1 + a\delta h_{lv}/k_l} \quad (2.17)$$

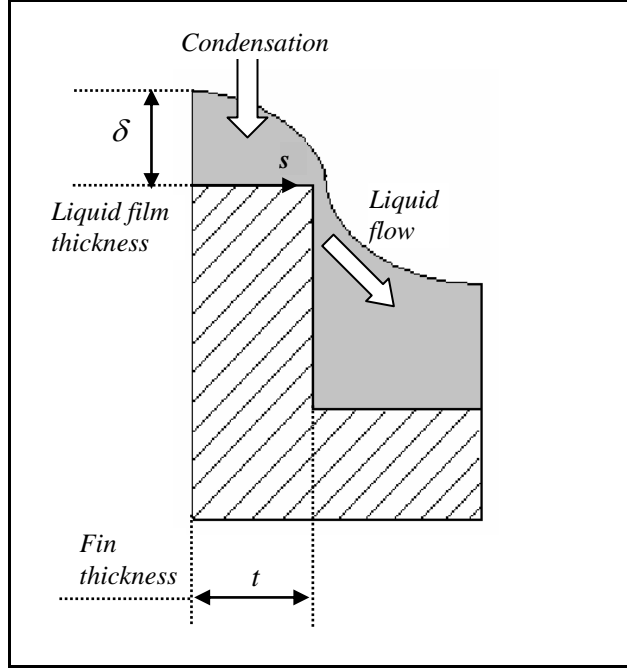


Figure 2.6: Condensation region and the groove geometry

The pressure difference between the vapor and liquid phases is made up of only the capillary pressure. The variation of film thickness along the fin top is small, therefore the derivative in the thin film curvature definition can also be neglected. The pressure jump at the liquid–vapor interface is given in terms of film thickness,  $\delta$ ,

$$P_v - P_l = \sigma \frac{d^2\delta}{ds^2} \quad (2.18)$$

The boundary conditions for the film thickness are

$$d\delta/ds = d^3\delta/ds^3 = 0 \quad \text{at} \quad s = 0, \quad (2.18a)$$

$$d\delta/ds = -\tan\theta \quad \text{at} \quad s = t, \quad (2.18b)$$

$$d^2\delta/ds^2 = 0 \quad \text{at} \quad s = t. \quad (2.18c)$$

The boundary conditions given in Equations 2.18a–c for the liquid film thickness

along the fin top and the mass balance, where the condensed fluid mass is equal to total mass flow rate from the fin, should be satisfied. In this case the differential equation for the film thickness is not solved but an integral approach is adopted using a fourth degree polynomial fit satisfying the boundary conditions to approximate the film thickness,

$$\delta = c_0 + c_1(s - t) + c_2(s - t)^2 + c_3(s - t)^3 + c_4(s - t)^4. \quad (2.19)$$

The coefficients  $c_1 - c_4$  are obtained using the boundary conditions defined in Equations 2.18a–c.

$$c_1 = -\tan(\pi/2 - \theta) \quad (2.19a)$$

$$c_2 = 0 \quad (2.19b)$$

$$c_3 = c_1/2t^2 \quad (2.19c)$$

$$c_4 = c_1/(2t)^3 \quad (2.19d)$$

The condition, where total mass flow rate along the fin top is equal to the condensation mass flow obtained using the kinetic theory, is used to calculate the unknown coefficient  $c_0$  in Equation 2.19. The left hand side of Equation 2.17 is integrated analytically to obtain the total mass flow,

$$\frac{\sigma}{3\nu} 6 c_0^3 c_3 = m'_c. \quad (2.20)$$

Heat flux at the liquid vapor interface is used to define the interface temperature, which is substituted into Equation 2.22.

$$T_{lv} = T_w + \frac{m''_c h_{lv} \delta}{k_l} \quad (2.21)$$

An iterative procedure is applied to obtain the constant  $c_0$  which satisfies Equation 2.22.

$$m'_c + \int_0^t \frac{a(T_w - T_v) + b(P_l - P_v)}{1 + a\delta h_{lv}/k_l} ds = f \quad (2.22)$$

After the film thickness variation defined by the fourth degree polynomial is obtained, the condensation mass flow is calculated from Equation 2.17.

Y. Zhang and A. Faghri [52] modeled a rectangular groove and studied the condensation at the fin top using the Volume of Fluid (VOF) method. Two dimensional incompressible momentum equation in a groove was solved along with the condensation at the fin top. The model included only one cross section of a grooved heat pipe, where the groove wall temperature had a fixed value. The effects of surface tension, wall temperature, contact angle at the solid-liquid interface and fin thickness were investigated. Numerical simulation was performed for water at the saturation temperature of 373 K. It was concluded that the liquid film on top of the fin became flatter and the heat transfer coefficient on the fin top became more uniform when the contact angle increased. It was also observed that the heat transfer coefficient decreased with increasing temperature difference between the groove wall and the liquid vapor temperature. Increasing surface tension decreased liquid film thickness and as a result heat transfer coefficient increased. The results of the present study are compared to the results of [52]. The physical parameters used in the comparison calculation are given in Table 2.2.

The results are compared for film thickness and heat flux variation along the fin top, where the contact angle is 84 degrees and the temperature difference between the vapor and solid wall is 10 K. There is a 25% difference in liquid film thickness at the beginning of the fin top (Figure 2.7) and this difference results in an 18% difference in heat flux values (Figure 2.8).

Table 2.2: Physical properties used for condensation mass flux calculation

Fin top thickness (m)	$t$	$20 \times 10^{-6}$
Vapor temperature (K)	$T_v$	373
Vapor pressure (Pa)	$P_v$	$1.033 \times 10^5$
Latent heat of evaporation (J/kg)	$h_{lv}$	$2.3 \times 10^{-6}$
Density of liquid (kg/m <sup>3</sup> )	$\rho$	1000
Dynamic viscosity (Pa·s)	$\mu$	$2.79 \times 10^{-4}$
Surface tension (N/m)	$\sigma$	$58.9 \times 10^{-3}$
Thermal conductivity (W/m · K)	$k_l$	0.6
Molar mass of liquid (kg/mol)	$M$	$18 \times 10^{-3}$
Molar volume of liquid (m <sup>3</sup> /mol)	$V_l$	$18 \times 10^{-6}$
Accommodation coefficient	$c$	1

The effect of contact angle and temperature difference on liquid film thickness and heat flux variation is also investigated. As the contact angle decreases the liquid film thickness variation is steeper as shown in Figure 2.9. A similar behavior can be seen for heat flux variation, when the liquid film decreases heat flux increases towards the end of the fin top (Figure 2.10).

Temperature difference between the solid wall and vapor affects the amount of condensation. When temperature difference is large, more vapor condenses into liquid phase and liquid film thickness is larger than the case with a smaller temperature difference (Figure 2.11). Since larger temperature differences result in increased condensation, heat flux is higher with larger temperature difference (Figure 2.12). These results are consistent with the results given by Y. Zhang and A. Faghri [52].

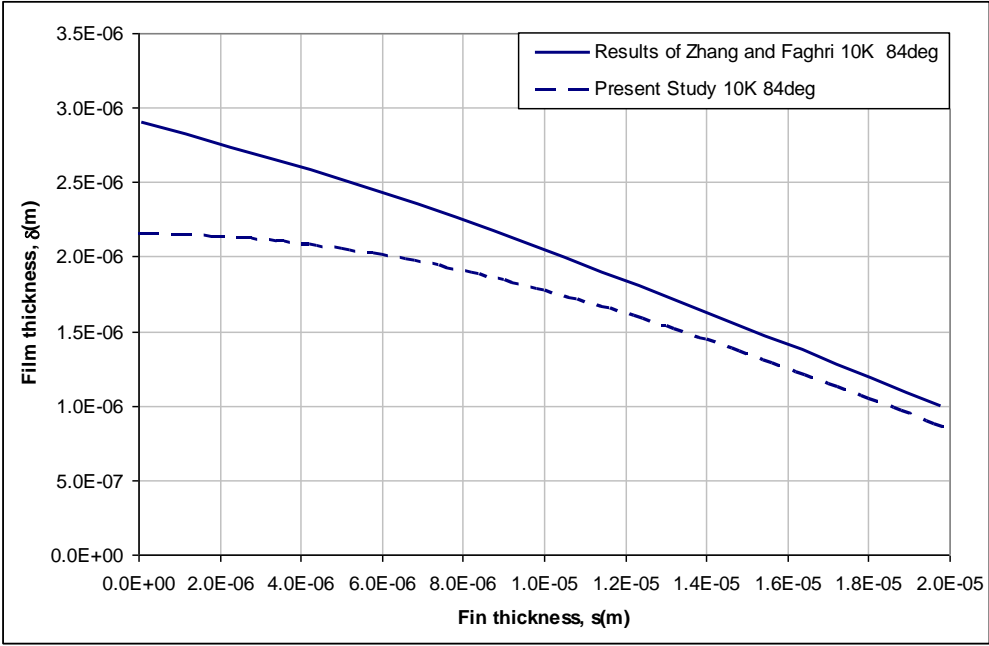


Figure 2.7: Liquid film thickness variation along the fin top

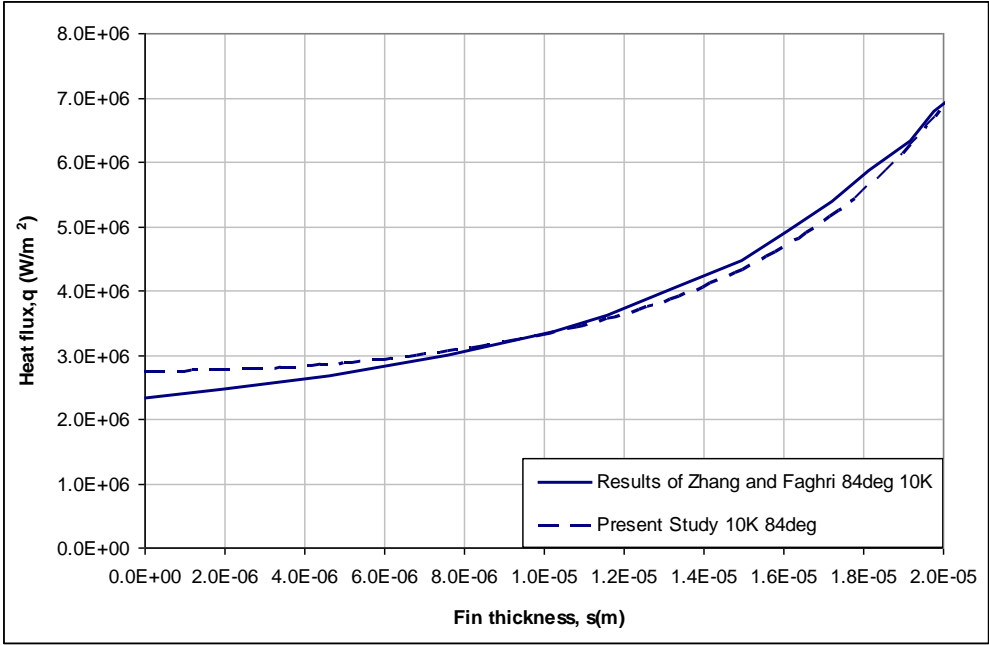


Figure 2.8: Heat flux variation along the fin top

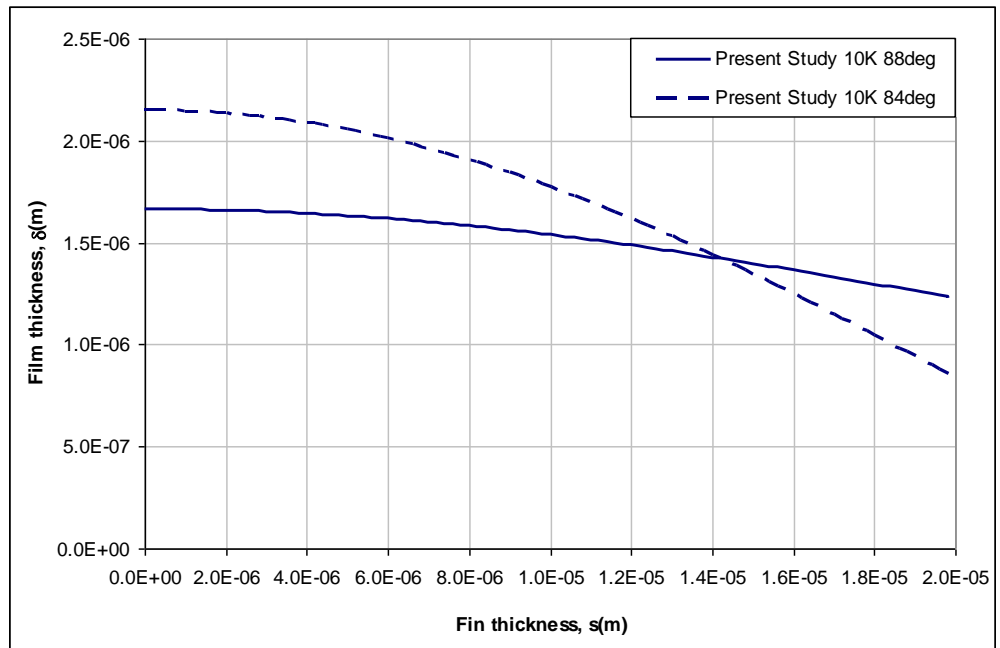


Figure 2.9: Liquid film thickness variation along the fin top for different contact angles

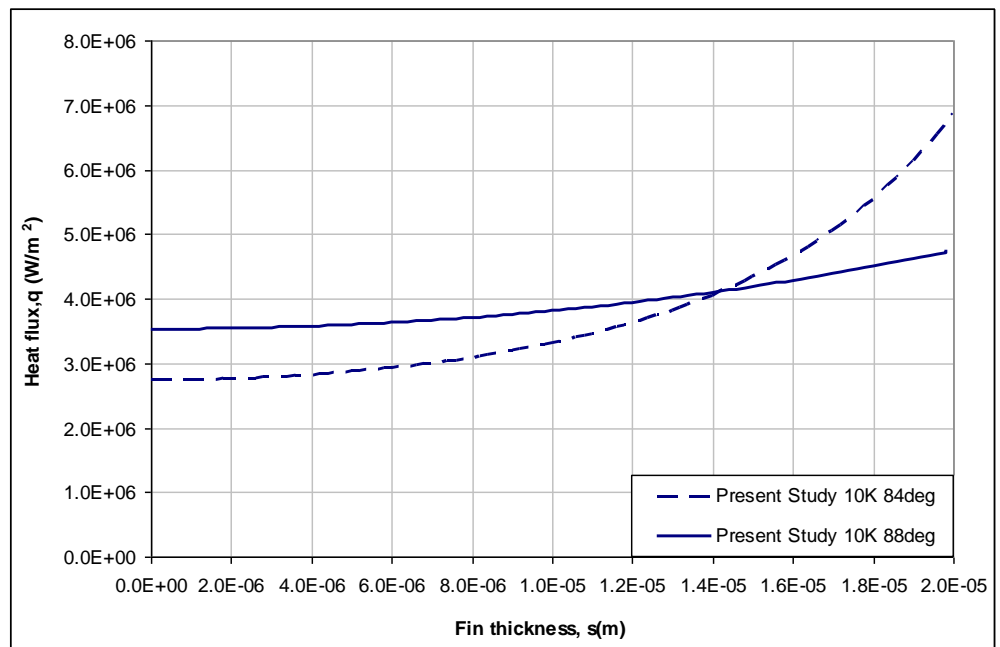


Figure 2.10: Heat flux variation along the fin top for different contact angles

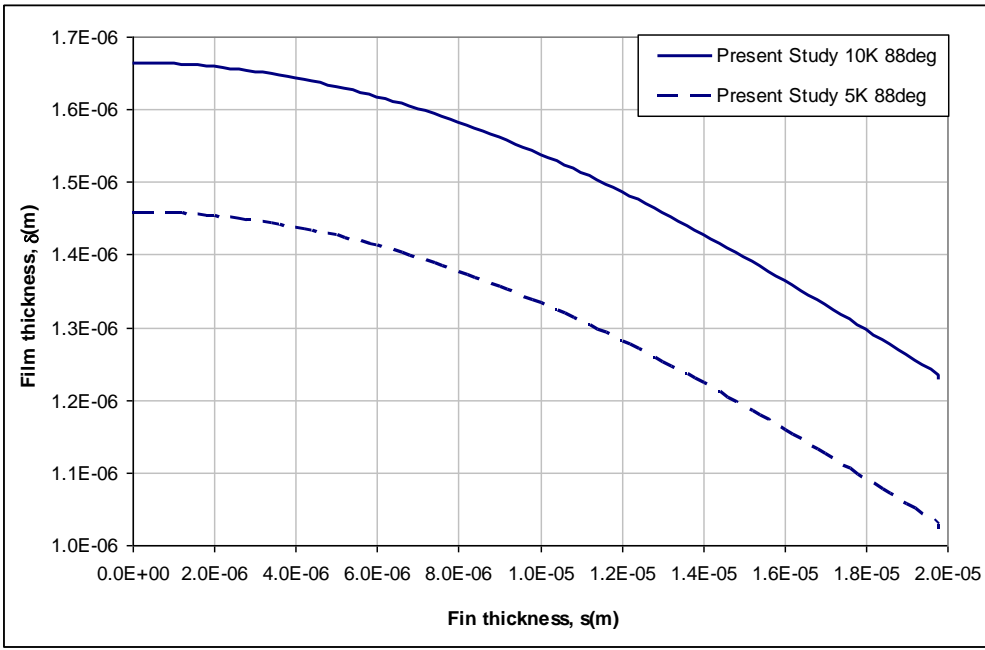


Figure 2.11: Liquid film thickness variation along the fin top for different temperature difference

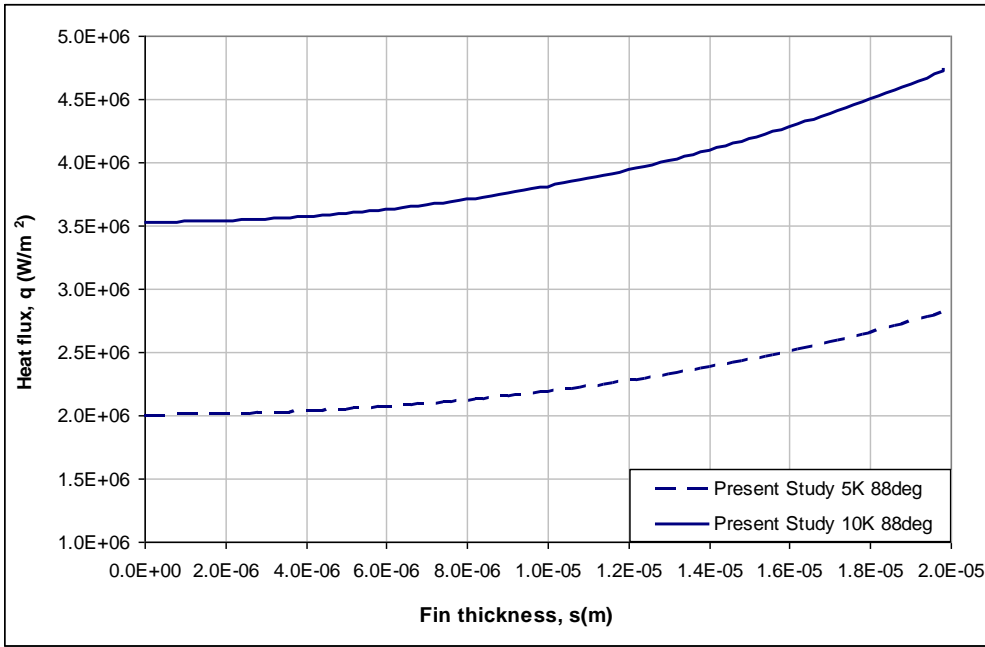


Figure 2.12: Heat flux variation along the fin top for different temperature difference

## CHAPTER 3

### SOLUTION METHODOLOGY

In the current study, a flat heat pipe with rectangular grooves along the heat pipe axis is investigated, which is presented in Figure 3.1. The bottom side of the heat pipe container has grooves and fins, above which there is a volume for vapor flow. The grooves of the heat pipe is filled with the working fluid. One end of the container is heated from bottom by a heat source, which will be called the heat source region, where the other end is cooled by a heat sink, which is called the heat sink region. In the present study heat sink is exposed to ambient environment by convection heat transfer. When the working fluid is heated by the heat source, it evaporates. This part of the heat pipe is called the evaporation region and the vapor flows to the colder side of the heat pipe, where it condenses. This colder region inside the heat pipe is called the condensation region. The condensed liquid flows through the grooves to the evaporation region. Between the heat source and sink regions, there can be a region, which has no heat transfer with the ambient, which is called the adiabatic region. Due to the symmetry of the geometry, the solution domain consists of half of the fin and groove as presented in Figure 3.1. Side walls and the upper side of the container and vapor region are not included in the solution domain. The coordinate system used for the solution domain is also shown in Figure 3.1, where the axial coordinate  $y$  starts from the condensation region and ends at the evaporation region. The transverse coordinate  $x$  is defined between two symmetry axes, which extends from the center of the fin to the center of the groove. The  $z$  coordinate starts from the exterior bottom side of the heat pipe container and extends to the top of the fin.

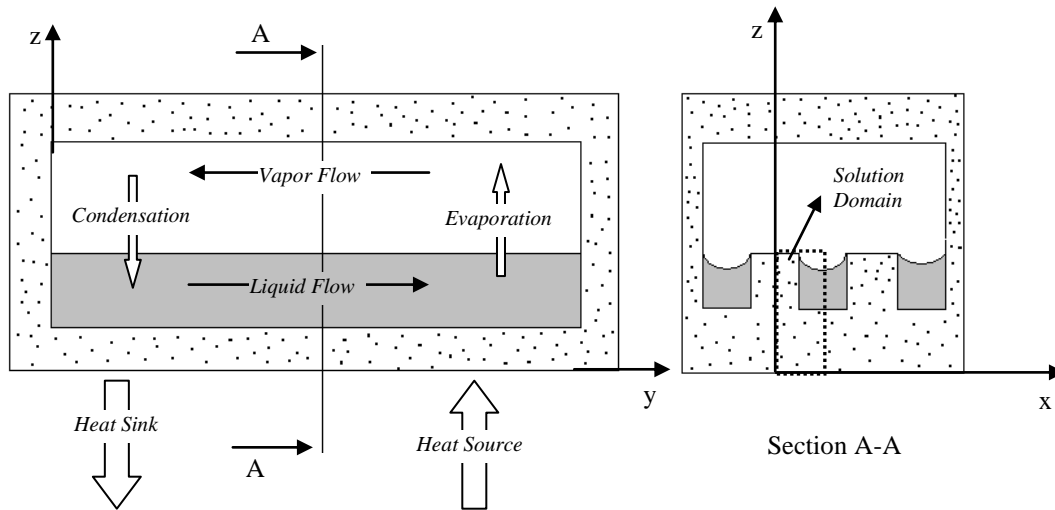


Figure 3.1: Heat and mass flow paths

A representative schematics for the current problem considering only the solution domain is given in Figure 3.2.

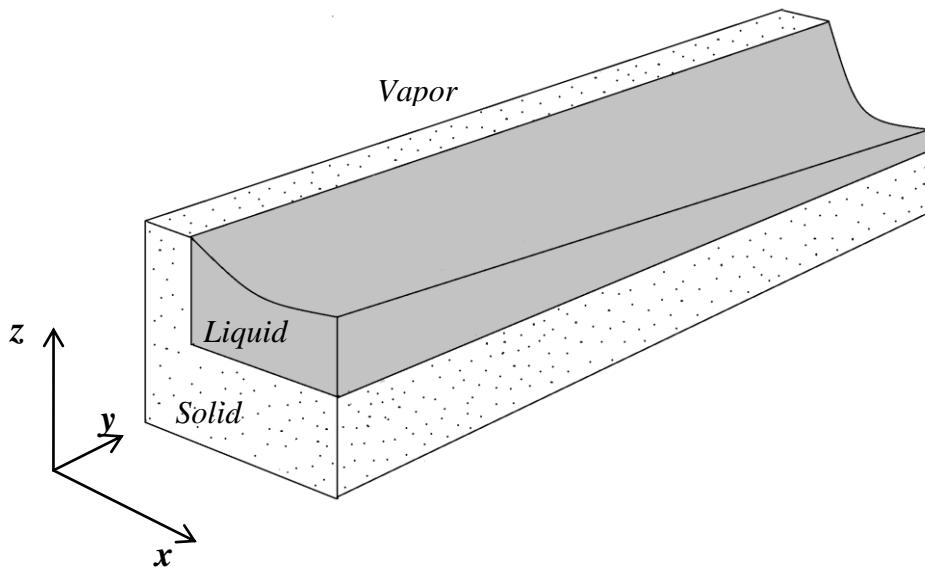


Figure 3.2: Axial variation of the liquid shape in the grooves, and the solid domain

The problem involves the solution of steady axial flow equation coupled with the steady heat transfer equation, which are combined through the phase change at the liquid–vapor interface, details of which were given in Chapter II. The simplified form of the momentum equation is written for the working fluid, which is called the liquid domain. The energy equation is solved both in working fluid and in the half of the fin, which is called the solid domain. The details of the flow and heat transfer models will be given in the following sections.

### 3.1 Flow Modeling in the Working Fluid

The main idea of a heat pipe is to create sufficient capillary force to overcome the friction losses along the heat pipe to feed the liquid to the evaporation region. A simplified form of the momentum equation along the heat pipe axis is formulated to calculate the variation of liquid–vapor interface radius along the heat pipe, which generates the capillary force necessary to drive the flow. A force balance for a unit liquid volume is given in Equation 3.1.

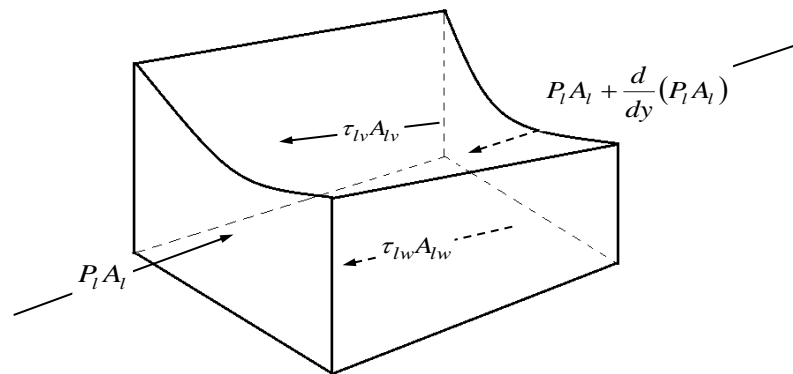


Figure 3.3: Forces acting on a fluid particle in the axial direction

$$\rho_l \frac{d}{dy} (A_l u^2) dy = - \frac{d}{dy} (A_l P_l) dy + A_{lw} \tau_{lw} + A_{lv} \tau_{lv} \quad (3.1)$$

where  $A_l$ ,  $\rho_l$ ,  $P_l$  and  $u$  represent cross-sectional area, density, pressure and velocity in axial direction in the liquid domain, respectively;  $A_{lw}$ ,  $A_{lv}$ ,  $\tau_{lw}$ ,  $\tau_{lv}$  are the cross-sectional area between liquid and groove wall interface, cross-sectional area between liquid and vapor domain interface and shear between liquid and groove wall, shear between liquid and vapor domain interface, respectively.

When phase change occurs all along the groove, the interfacial shear between the liquid and vapor can be neglected [6]. In the current study, liquid–vapor interfacial shear is not taken into account, since due to axial conduction there is a smooth transition from the condensation to the evaporation region, which means that there is a phase change all along the heat pipe axis. Pressure difference between the liquid and vapor phases of the working fluid can be written from Young–Laplace equation,

$$P_v - P_l = \frac{\sigma}{R} \quad (3.2)$$

where  $R$  is the liquid–vapor interface radius. Using the assumption that the change in vapor pressure along the heat pipe is negligible, the liquid pressure change along the heat pipe becomes,

$$\frac{dP_l}{dy} = -\sigma \frac{d}{dy} \left( \frac{1}{R} \right) \quad (3.3)$$

Equation 3.3 is substituted into Equation 3.1 to obtain the relation between the variation of the liquid velocity and the liquid–vapor interface radius along heat pipe axis.  $L_{lw}$  in Equation 3.4 represents wetted perimeter at liquid–groove wall interface. The momentum balance along the axis becomes,

$$\rho_l \frac{d}{dy} (A_l u^2) = -\sigma A_l \frac{d}{dy} \left( \frac{1}{R} \right) + L_{lw} \tau_{lw} \quad (3.4)$$

In Equation 3.4 the change in the liquid cross sectional area in the pressure term

is neglected [43]. Shear at the liquid–groove wall interface is calculated using a friction coefficient,  $f$ .

$$\tau_{lw} = \frac{1}{2}\rho u^2 f = \frac{1}{2}(\text{Re} \cdot f) \frac{\mu}{D_h} u \quad (3.5)$$

Reynolds number is based on the hydraulic diameter,  $D_h$ , which is defined by the following relation,

$$D_h = \frac{4A_l}{L_{lw}} \quad (3.6)$$

Friction coefficient,  $f$ , is calculated using the correlation given by Schneider and DeVos which is applicable for rectangular grooves without liquid–vapor interaction [38].

$$\text{Re} \cdot f = \frac{8r^2}{(1+r)^2 (1/3 - (64/\pi^5 r) \tanh \pi/2r)} \quad (3.7)$$

where  $b$  is the half groove width and  $d$  is the groove depth and  $r = d/b$ . The geometric details of the groove are given in Figure 3.4.

When the liquid interface is attached to the top corners of the groove, it permits the contact angle to vary freely so long as it remains larger than the minimum contact angle. After this value of contact angle is reached, further evaporation causes a retreat of the liquid–vapor interface without changing the contact angle. This region is referred as the “dead zone”. In this case, in a groove of uniform width, the radius of interface remains constant axially, therefore, over this range there is no variation in the capillary pressure and hence no pressure gradient to drive a flow [53]. In the current study it is assumed that the liquid contacts always at top corner of the groove and contact angle changes up to its minimum value.

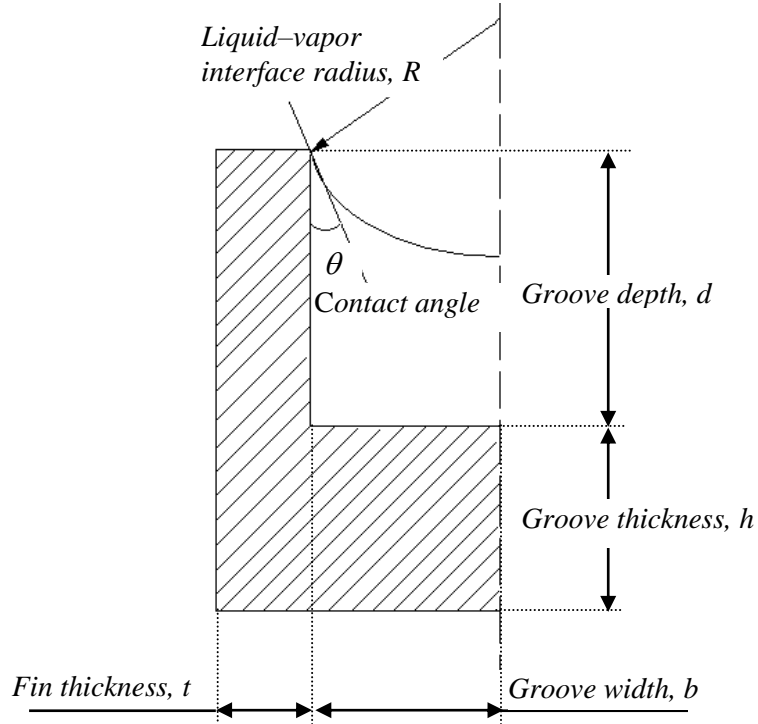


Figure 3.4: Groove geometry

Hydraulic radius and liquid cross sectional area can be found from the geometry given Equations 3.8 and 3.9,

$$A_l = 2bd - \left[ (\pi/2 - \theta) R^2 - \frac{b^2}{\tan(\pi/2 - \theta)} \right] \quad (3.8)$$

$$D_h = \frac{4 \left[ 2bd - (\pi/2 - \theta) R^2 + (b^2 / \tan(\pi/2 - \theta)) \right]}{2(b + d)} \quad (3.9)$$

Mass balance for a unit liquid volume is given in Equation 3.10, where  $\dot{m}_t$  is the total phase change mass flow rate. It is explained in Chapter II, that evaporation takes place in a small region called the micro region for evaporation. Previous studies show that micro region evaporation heat flux values are high, but since the micro region length is of the order of one micron, the overall effect

is not as high as expected. However, it is reported by Stephan and Busse [47] that evaporation from micro region constitutes 45% and along the rest of the liquid–vapor interface, called the macro region, accounts for 55% of the overall evaporation. Therefore, both micro and macro region evaporation are included into the formulation, solution procedure of macro region evaporation will be presented in Section 3.3. Phase change mass flow rate,  $\dot{m}_t$ , in Equation 3.10 includes the sum of micro and macro evaporation flow rates. Macro evaporation is calculated at the end of the heat transfer analysis, therefore the details will be explained in Section 3.3. In flow analysis, it will be mentioned as total phase change mass flow rate.

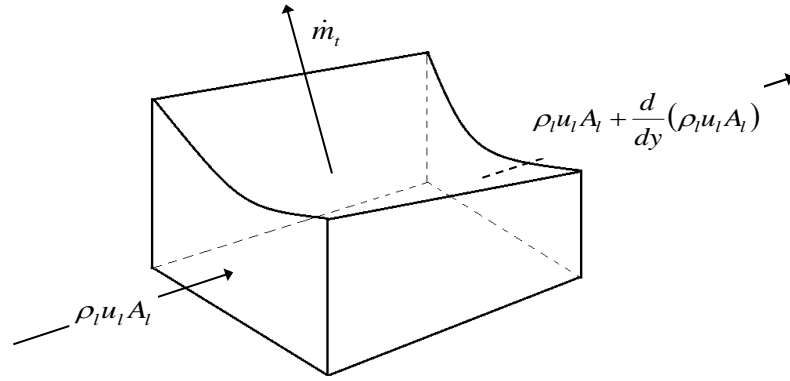


Figure 3.5: Mass balance

$$\frac{d}{dy}(\rho_l u_l A_l) dy + \dot{m}_t = 0 \quad (3.10)$$

Equations 3.4 and 3.10 are solved iteratively by secant method for liquid–vapor interface radius,  $R$ , where the velocity at the beginning of the condenser is zero. The radius at the beginning of the condenser,  $R_0$ , is defined as an initial value. The solution starts from condensation side and is integrated explicitly for each axial position. The iteration starts with an assumed value of radius for the

next axial position, which is used to calculate the liquid cross-sectional area. Total phase change mass flow rates are obtained and Equation 3.10 is solved for the average axial liquid velocity. Friction coefficient in Equation 3.7 is used to calculate shear at the liquid–groove wall for the new axial position as given in Equation 3.5. Momentum equation given in Equation 3.4 is solved for the radius. The iteration for radius continues until convergence is reached. The calculation is repeated for the next axial position. At the end of the momentum calculation axial liquid velocity and liquid–vapor interface radius distributions are obtained along the axial length of the groove.

### 3.2 Heat Transfer Modeling

Heat transfer analysis is performed in both the solid domain and the liquid domain, which is presented in Figure 3.6. Energy equation in the solid domain includes only the conduction terms, where convective terms are also included in the liquid domain. Three dimensional steady heat conduction equation is solved in the solid domain subject to the boundary conditions defined in Equations 3.11.a–d,

$$\frac{\partial^2 T}{\partial x^2} + \frac{\partial^2 T}{\partial y^2} + \frac{\partial^2 T}{\partial z^2} = 0 \quad (3.11)$$

The boundary conditions for solid domain define the interface of the heat pipe to outside environment. It is assumed that at both ends,  $y = 0$  and  $y = L$ , there is no heat transfer. There is a symmetry condition at the center of the fin and the groove,  $x = 0$  and  $x = t + b$  (Figure 3.4). Heat source region is defined by an input heat flux and heat sink region is defined by convection to the ambient, where ambient temperature and heat transfer coefficients are given as constant values,

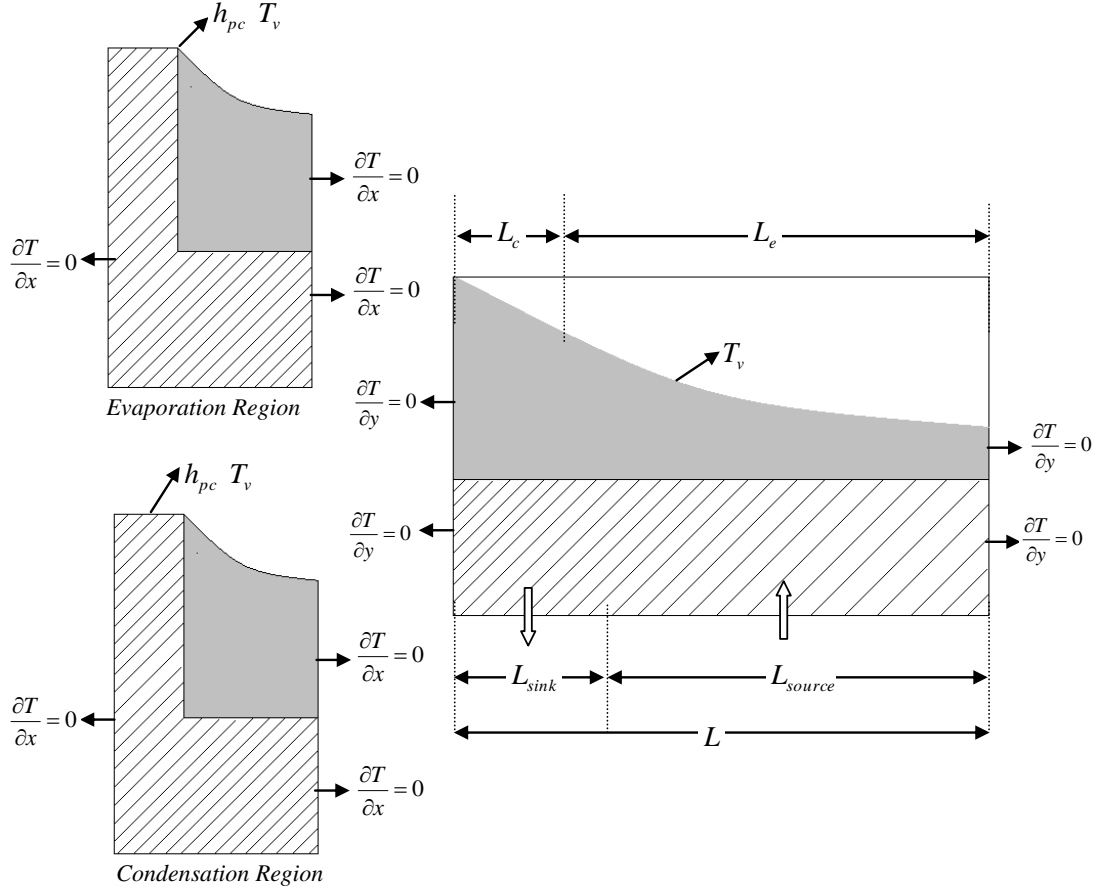


Figure 3.6: Heat transfer domain geometry with boundary conditions

$$\frac{\partial T}{\partial x} = 0 \quad \text{at} \quad x = 0; \quad x = t + b, \quad (3.11a)$$

$$\frac{\partial T}{\partial y} = 0 \quad \text{at} \quad y = 0; \quad y = L, \quad (3.11b)$$

$$\frac{\partial T}{\partial z} = q''_{in} \quad \text{at} \quad z = 0; \quad L_{source} < y < L, \quad (3.11c)$$

$$k_s \frac{\partial T}{\partial z} = h_{amb} (T - T_{amb}) \quad \text{at} \quad z = 0; \quad 0 < y < L_{sink}. \quad (3.11d)$$

Three dimensional energy equation including convective terms is given in Equation 3.12 for the liquid domain. The convection terms are included due to axial

velocity,  $u$ , and transverse velocity,  $w$ . In the flow model for the liquid domain, a lumped axial flow is considered, however, heat transfer model is three dimensional. The difference between the two models requires a detailed mass balance in the interior grid points for the liquid domain. Due to the phase change at liquid–vapor interface, a velocity component in  $z$ –direction should be taken into account.

$$u \frac{\partial T}{\partial y} + w \frac{\partial T}{\partial z} = \frac{k_l}{\rho C_{pl}} \left( \frac{\partial^2 T}{\partial x^2} + \frac{\partial^2 T}{\partial y^2} + \frac{\partial^2 T}{\partial z^2} \right) + \frac{\mu}{\rho_l C_{pl}} \Phi \quad (3.12)$$

where  $\Phi$  represent viscous dissipation. For the liquid domain, it is also assumed that at both ends,  $y = 0$  and  $y = L$ , there is no heat transfer. There is a symmetry condition at the groove center,  $x = t + b$ . At liquid–vapor interface temperature is set at the vapor temperature,  $T_v$ . Stephan and Busse [47] stated that the interface temperature at the liquid–vapor interface in the micro region is larger than the vapor saturation temperature due to change in the liquid–vapor interface radius variation. However, in meniscus or macro region the interface radius becomes constant and the temperature difference diminishes. Therefore, the temperature at liquid–vapor interface in meniscus region is defined by a constant vapor temperature in this model.

$$\frac{\partial T}{\partial x} = 0 \quad \text{at} \quad x = t + b, \quad (3.12a)$$

$$\frac{\partial T}{\partial y} = 0 \quad \text{at} \quad y = 0 \quad ; \quad y = L, \quad (3.12b)$$

$$T = T_v \quad \text{at} \quad t < x < t + b \quad ; \quad z = d + h. \quad (3.12c)$$

Phase change at the liquid–vapor interface is both related to heat transfer analysis and mass balance, since condensation and evaporation regions are differentiated by the temperature at fin top corner, where solid, liquid and vapor regions coincide. Since the thermal conductivity of the solid is approximately two orders of magnitude higher than the liquid, the temperature distribution along the

fin top is almost uniform. As mentioned micro evaporation takes place at the fin top corner location. Therefore, the temperature at fin top corner point is used as representative temperature of the solid domain for phase change analysis. The region, where the fin top corner temperature is higher than the vapor temperature is defined as the evaporation region and the rest is defined as the condensation region. According to this definition, condensation and evaporation mass fluxes are calculated using the relations obtained from the kinetic theory given in Equations 2.15 and 2.22. For heat transfer analysis the calculated mass fluxes are not directly used, but special boundary conditions are defined for fin top region in the solid domain at  $z = d + h$  and for fin top corner, where solid and liquid domain meet.

As mentioned in Chapter II, condensation takes place all along the fin top, but evaporation occurs in a small region called the micro region, which is located at the fin top corner. For the condensation region, a heat balance is written using calculated phase change mass flux to obtain an average phase change heat transfer coefficient,  $h_{pc}$  defined by Equation 3.13.  $T_w$  represents the temperature at the fin top corner point,

$$\frac{m'_c h_{lv}}{t} = h_{pc} (T_v - T_w). \quad (3.13)$$

In the evaporation region, it is assumed that evaporation heat transfer defined by  $h_{pc}$  acts along the first grid in the liquid domain at the fin top corner and the average heat transfer coefficient is calculated by Equation 3.14.

$$\frac{m'_e h_{lv}}{0.5x^*} = h_{pc} (T_w - T_v), \quad (3.14)$$

where  $x^*$  represents the length of the first grid in the liquid domain. The boundary conditions for the fin top are given in Equation 3.15a–c. In the condensation region, a convective boundary condition is defined, but for evaporation region fin top is assumed to be insulated, since there is no fluid at the fin top along the evaporation region and heat transfer between solid and vapor domain is negligible. Evaporation heat transfer is defined by a convective boundary condition

only for the fin top corner point,

$$k_s \frac{\partial T}{\partial z} = h_{pc} (T_v - T) \quad 0 < x < t \quad ; \quad z = d + h; T < T_v \quad (3.15a)$$

$$\frac{\partial T}{\partial z} = 0 \quad 0 < x < t \quad ; \quad z = d + h; T > T_v \quad (3.15b)$$

$$k_s \frac{\partial T}{\partial z} = h_{pc} (T - T_v) \quad t < x < t + x^*; \quad z = d + h; T > T_v \quad (3.15c)$$

Equations (3.11) and (3.12) are solved by finite difference method subject to the boundary conditions defined by Equations 3.11a–d, 3.12a–c and 3.15a–c. Liquid domain does not have a pre-determined shape due to the variation of the liquid–vapor interface radius along the heat pipe axis. Therefore, a coordinate transformation is applied for this region, where the transformed coordinates are defined as,

$$\lambda = x \quad (3.16a)$$

$$\eta = y \quad (3.16b)$$

$$\xi = z_0 \left( 1 + \frac{z - z_0}{\Delta d_i(y) - z_0} \Delta d_0 \right) \quad (3.16c)$$

where  $z_0$  is equal to the groove thickness,  $\Delta d_i$  is the depth at each  $x$  position along the groove and  $\Delta d_0$  is the depth of the liquid at the center of the channel  $x = t$ . Equation (3.12) can be rewritten using the new coordinates and rearranging the terms as follows,

$$\begin{aligned} u \left( \frac{\partial T}{\partial \eta} + a_0 \frac{\partial T}{\partial \xi} \right) + w \left( a_1 \frac{\partial T}{\partial \xi} \right) &= \frac{k_l}{\rho C_{pl}} \left( \frac{\partial^2 T}{\partial \lambda^2} + \frac{\partial^2 T}{\partial \eta^2} + a_2 \frac{\partial^2 T}{\partial \xi^2} \right) + \\ &\frac{k_l}{\rho C_{pl}} \left( a_3 \frac{\partial^2 T}{\partial \lambda \partial \xi} + a_4 \frac{\partial^2 T}{\partial \eta \partial \xi} + a_5 \frac{\partial T}{\partial \xi} \right) + \\ &\frac{\mu}{\rho_l C_{pl}} \Phi \end{aligned} \quad (3.17)$$

where the coefficients are defined as,

$$a_0 = \frac{\partial \xi}{\partial y} \quad (3.17a)$$

$$a_1 = \frac{\partial \xi}{\partial z} \quad (3.17b)$$

$$a_2 = \left( \frac{\partial \xi}{\partial x} \right)^2 + \left( \frac{\partial \xi}{\partial y} \right)^2 + \left( \frac{\partial \xi}{\partial z} \right)^2 \quad (3.17c)$$

$$a_3 = 2 \frac{\partial \xi}{\partial x} \quad (3.17d)$$

$$a_4 = 2 \frac{\partial \xi}{\partial y} \quad (3.17e)$$

$$a_5 = \frac{\partial^2 \xi}{\partial x^2} + \frac{\partial^2 \xi}{\partial y^2} + \frac{\partial^2 \xi}{\partial z^2} \quad (3.17f)$$

The details about the coordinate transformation are given in Appendix A.

At the solid–liquid interface the solution domain includes volumes, half of which are solid and uniform, where the other half are liquid and non-uniform. For this region Equations 3.11 and 3.12 cannot be used directly, therefore a heat balance for each volume is written explicitly. There are four different regions (i) Region I, the interface located at the bottom of the groove, (ii) Region II, the interface located at the groove bottom corner, and (iii) Region III, the interface located along the depth of the groove, and (iv) Region IV, the interface located at fin top corner, which are shown in Figure 3.7. The details of the derivation of these equations are explained in Appendix B.

Due to the skewness of the control volume in Region IV (Figure 3.7) and the difference in equations used in the bulk liquid domain and solid–liquid interface domain (Region I–IV) and to provide a transition from interface region to the bulk liquid domain, special equations using overall heat balance equations for control volumes are written for Region V, which are explained in Appendix B.

### 3.2.1 Grid generation

The first step in the solution of heat transfer equations given in Equations 3.11, 3.17 and Appendix B is the generation of grid points. There are four sub-regions for each  $x - z$  plane: (i) Region A, the lower side of the fin, (ii) Region B, the solid domain bottom of the groove, (iii) Region C, upper side of the fin, (iv) Region D, liquid domain in the groove. In each region the grid points are equally spaced along a constant coordinate line, whose definitions are given in Equations 3.18a–f. The computational grid structure in the physical domain is presented in Figure 3.7. The number of grid points in  $x$ -direction is  $m_1$  for Region A and C, where  $m - m_1$  points are defined in Region B and D. In  $z$ -direction  $k_1$  points are used in Region A and B, where the number is  $k - k_1$  in Region C and D. In the axial direction ( $y$ ) there is no difference between the four regions, where  $n$  points are defined.

$$x_i = x_{i-1} + \frac{t}{m_1 - 1} \quad (3.18a)$$

$$x_i = t + \left( x_{i-1} + \frac{b}{m - m_1} \right) \quad (3.18b)$$

$$y_j = y_{j-1} + \frac{L}{n - 1} \quad (3.18c)$$

$$z_k = z_{k-1} + \frac{z_0}{k - 1} \quad (3.18d)$$

$$z_k = z_{k-1} + \frac{z_0}{k - 1} \quad (3.18e)$$

$$z_k = z_0 + \left( z_{k-1} + \frac{(\Delta d_i)_j}{k - k_1} \right) \quad (3.18f)$$

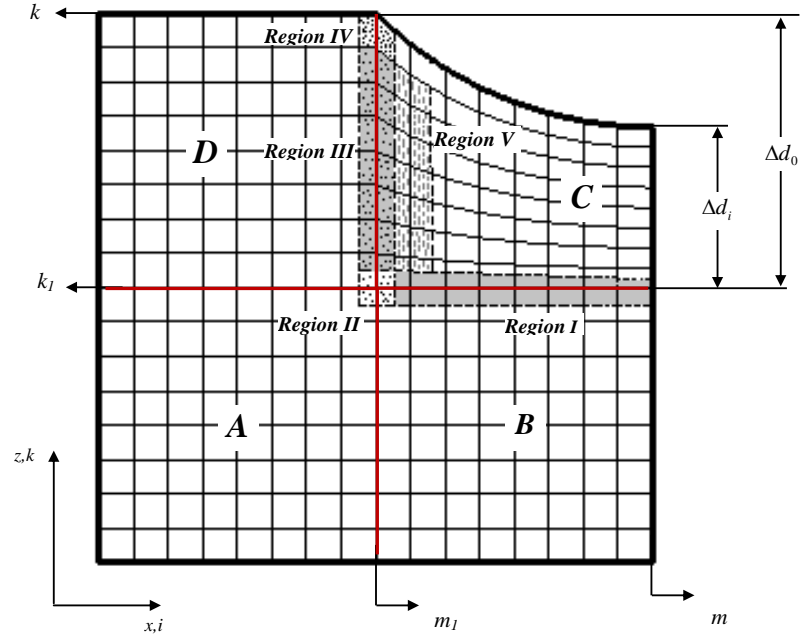


Figure 3.7: Computational grid in the physical domain at a cross-section of the channel

### 3.3 Solution Procedure

Axial momentum equation detailed in Section 3.1 in the liquid domain is coupled with the heat transfer equation detailed in Section 3.2. As explained in Chapter II, phase change mass flux equation is a function of fin top corner temperature, solid-liquid contact angle, which is related to the liquid-vapor interface radius through the geometry. Momentum equation is coupled to the phase change mass fluxes through the mass balance. The lengths of the evaporation and condensation regions along the heat pipe axis are unknown at the beginning of the solution and depend on the fin top corner temperature distribution along the heat pipe axis. All the parameters defining the problem are coupled, therefore an iterative solution procedure is applied.

The solution procedure starts with the solution of the axial momentum equa-

tion (Equation 3.4) for the distribution of liquid–vapor interface radius variation,  $R(y)$ . The input values are the liquid–vapor interface radius,  $R_0$ , the liquid velocity,  $u_0$ , at the beginning of the condensation region and the vapor temperature,  $T_v$ . Mass balance equation (Equation 3.10) is used to find axial liquid velocity,  $u(y)$ , the evaluation of which requires total phase change mass flow rates,  $\dot{m}_t$ . Total phase change mass flow rates consist of evaporation and condensation mass fluxes obtained from micro region relations (Equations 2.15 and 2.22) and from macro or meniscus region. Macro region phase change mass fluxes are calculated from the heat balance written for the liquid–vapor interface region using the temperature distribution in the liquid domain given in appendix B Section VI. For the first step of iteration, there is no calculated temperature distribution, therefore an assumed fin top corner temperature distribution along the heat pipe axis,  $T_w(y)$ , is used to calculate the micro region phase change mass flow rates and macro region phase change mass flow rates are not included in the mass balance. After liquid–vapor interface radius variation,  $R(y)$ , and liquid velocity,  $u(y)$ , values are obtained, grid points are generated as defined in Section 3.2.1 for the heat transfer analysis. The transverse velocity,  $w$ , is required at each grid point for convective terms in Equation 3.17, therefore mass balance is written for each control volume using the axial velocity distribution and phase change mass flow rates.

$$\dot{m}_i - \dot{m}_o + \dot{m}_{by} - \dot{m}_{bz} - \dot{m}_{ty} + \dot{m}_{tz} = 0 \quad (3.19)$$

where

$$\dot{m}_i = \frac{1}{2} (u_{j-1} + u_j) \rho_l A_{y_{j-\frac{1}{2}}} \quad (3.19a)$$

$$\dot{m}_o = \frac{1}{2} (u_{j+1} + u_j) \rho_l A_{y_{j+\frac{1}{2}}} \quad (3.19b)$$

$$\dot{m}_{by} = u_j \rho_l A_{bn_y} \quad (3.19c)$$

$$\dot{m}_{ty} = u_j \rho_l A_{tn_y} \quad (3.19d)$$

$A_y$  represents the cross-sectional area in the  $x-z$  plane and  $u(j)$  axial velocity in each  $y$ -position. Since the areas are different on each face due to the irregular shape of the liquid domain, they are approximated as trapezoidal areas and calculated for each control volume using the solution domain grid points. The upper and lower surfaces of the liquid control volumes are curved due to the axial variation of interface radius and the surface normal has components in the  $x$ - and  $y$ -coordinates. The area  $A_{nt_y}$  represents the projected area of the upper curved surface on the  $x-z$  plane, which is also approximated as a trapezoidal area and calculated using grid points.  $A_{nb_y}$  is the projected area of the lower curved surface. Figure 3.8 shows the mass flows into and out of the control volumes at a constant  $x$ -line on the  $y-z$  plane. The calculation starts from the bottom control volumes at the solid-liquid interface and the calculated  $\dot{m}_{tz}$  values are equated to  $\dot{m}_{bz}$  of the upper grid point. Since the grid points are defined centrally in the control volumes, average of  $\dot{m}_{bz}$  and  $\dot{m}_{tz}$  values are used in the calculation of the velocity  $w(x, y, z)$ .

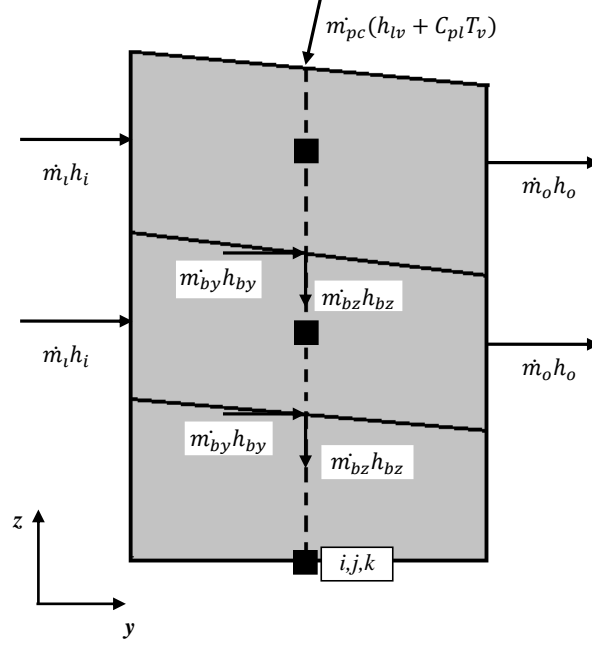


Figure 3.8: Mass balance in the liquid domain for the calculation of transverse velocity

Heat transfer equations Equation 3.11, 3.17 and heat balance equations given in Appendix B Section I–V are solved subject to the boundary conditions 3.11a–d, 3.12a–c and 3.15a–c. Since the newly obtained temperature distribution is different than the initial fin top corner temperature,  $T_w(y)$ , a successive substitution procedure is applied for  $T_w$  until convergence is reached. During temperature iterations, phase change mass flow rates from micro regions are also recalculated using new values of the fin top corner temperatures. At the end of the analysis the overall evaporated mass should be equal to condensed mass, which implicitly satisfies overall energy balance of the solution domain. Therefore, evaporation and condensation mass fluxes from macro regions are calculated using the converged temperature distribution and the mass fluxes are calculated from the energy balance written for the liquid–vapor interface or top of the liquid domain region (Appendix B, Section VI). Micro and macro region mass fluxes are integrated along the  $y$ –axis and sum of the evaporated and condensed masses are found, which are not equal until convergence. The vapor temperature is a

parameter defining the phase change mass fluxes, therefore an iteration using the secant method is carried out to equalize the masses in terms of vapor temperature,  $T_v$ . During these iterations micro region phase change mass fluxes are recalculated for new values of vapor temperature,  $T_v$ , in each iteration, which is terminated, when a set convergence criteria is satisfied.

At this point, the liquid–vapor interface radius variation,  $R(y)$ , and temperature distribution in the solid and liquid domains are not compatible, since phase change mass fluxes from micro regions are recalculated during iterations for new values of vapor temperature,  $T_v$ , and fin top corner temperature,  $T_w(y)$ . Therefore, the solution of axial momentum equation is repeated for new values of  $T_v$ ,  $T_w(y)$  and mass flow rates from macro region. This iteration procedure is repeated until the change in  $T_v$  satisfies a set convergence criteria. The solution procedure is summarized in Figure 3.9.

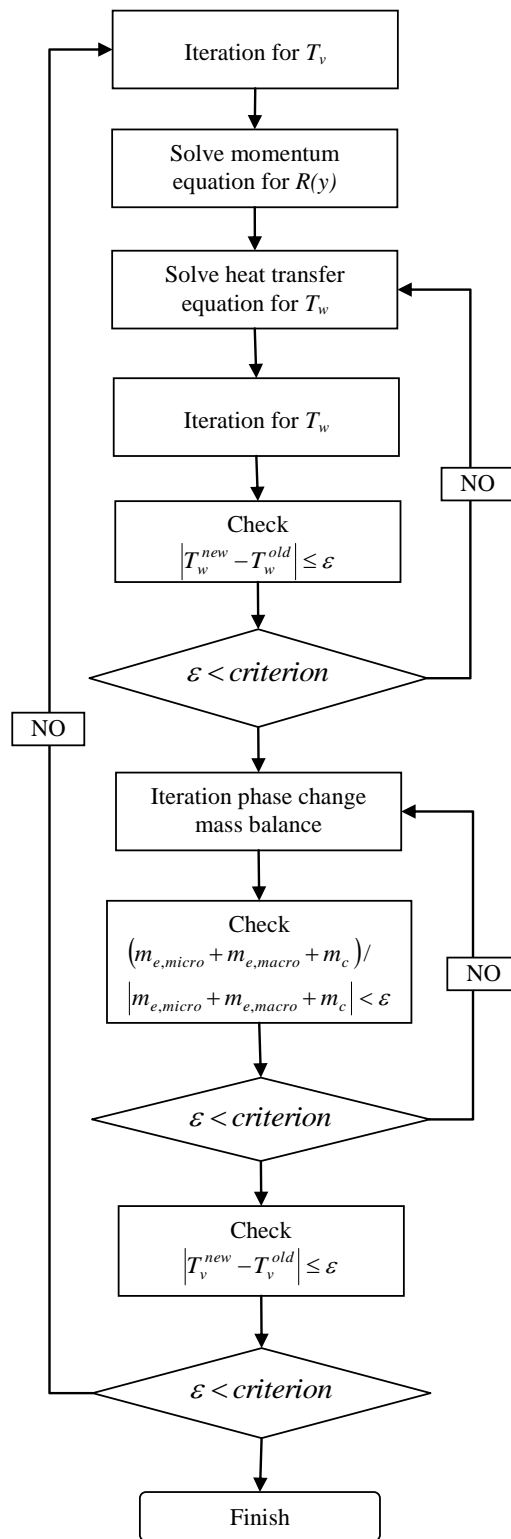


Figure 3.9: Flowchart for the solution procedure

## CHAPTER 4

### RESULTS FOR HEAT PIPE MODEL

In this chapter the results obtained for the heat pipe model will be compared with those available in the literature. In the second part a sample problem is introduced and the effect of the physical and thermal parameters will be investigated for a constant heat input. The axial variation of the temperature and liquid–vapor interface will be provided to understand the effect of various parameters on heat pipe performance. The last part includes the study of the maximum heat capacity of the heat pipe in terms of different groove width, groove depth combinations, where at the end of the evaporation region dry-out limit is reached.

#### 4.1 Validation of the Present Study

The results of the present study are compared to the experimental/numerical study of Lefevre *et al.* [6] for validation. The flat heat pipe used in the study is made of copper and the working fluid is methanol. The physical properties used in the computations are given in Table 4.1

Table 4.1: Dimension and physical properties used in validation model

Channel length	mm	230
Groove width	mm	0.2
Fin thickness	mm	0.2
Groove thickness	mm	2
Groove depth	mm	0.38
Length of heat source region	mm	190
Length of heat sink region	mm	30
Thermal conductivity of solid	W/m·K	400
Thermal conductivity of liquid	W/m·K	0.2
Latent heat of evaporation	kJ/kg	1085
Density of liquid	kg/m <sup>3</sup>	792
Dynamic viscosity of liquid	Pa·s	$3.14 \times 10^{-4}$
Specific heat of liquid	J/kg·K	2530
Surface tension	N/m	$18.5 \times 10^{-3}$
Molar mass of liquid	kg/mol	$32 \times 10^{-3}$
Molar volume of liquid	m <sup>3</sup> /mol	$42 \times 10^{-6}$
Vapor pressure	Pa	$1.31 \times 10^5$
Heat load	W/m <sup>2</sup> ·K	5000
Ambient heat transfer coefficient	W/m <sup>2</sup> ·K	2100
Ambient temperature	K	323

Two parameters are used to analyze and compare the results. The first one is the liquid–vapor interface radius variation along the heat pipe axis, which generates the driving capillary pressure. The second one is the temperature at fin top corner point where solid–liquid–vapor domains meet, which is used as a representative temperature of the heat pipe. The temperature at this location will be termed as the “edge temperature”. The results for the interface radius variation is given in Figure 4.1. The difference between the present study and the results of [6] is within 9% when convective heat transfer in the liquid domain

is not included. There is no considerable difference in the results when effect of convection is included.

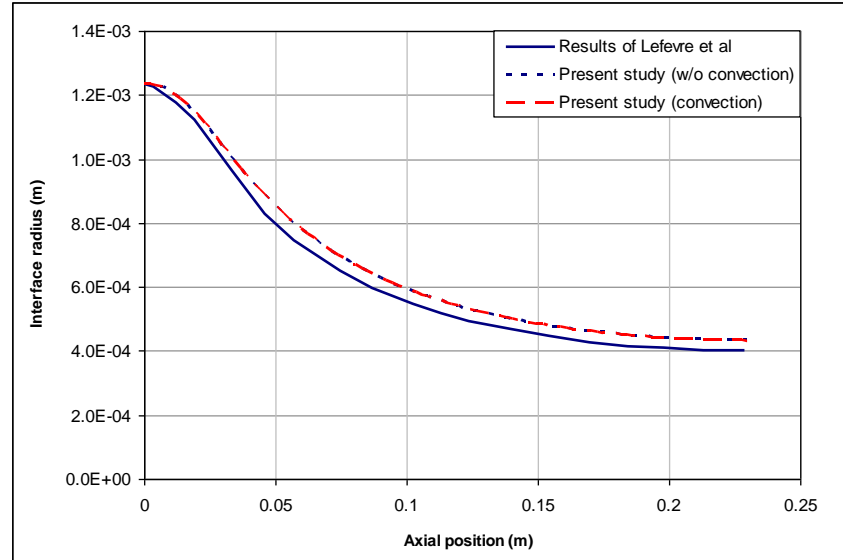


Figure 4.1: Liquid interface radius variation along the heat pipe axis

The variation of liquid velocity,  $u(y)$ , along the heat pipe axis is given in Figure 4.2. At the beginning of the condensation region the liquid velocity is zero and increases to a maximum value of 5.3 mm/s at the end of the condensation region, 4.4 cm away from the beginning of the groove. The axial liquid velocity starts to decrease due to evaporation in spite of the decrease in the liquid cross-sectional area until the end of the heat pipe axis.

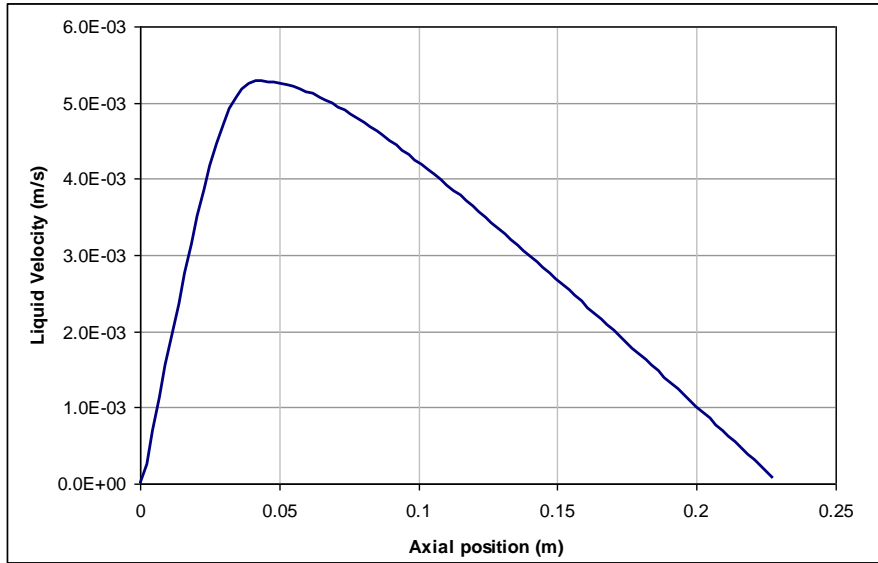


Figure 4.2: Axial liquid velocity variation along the heat pipe axis

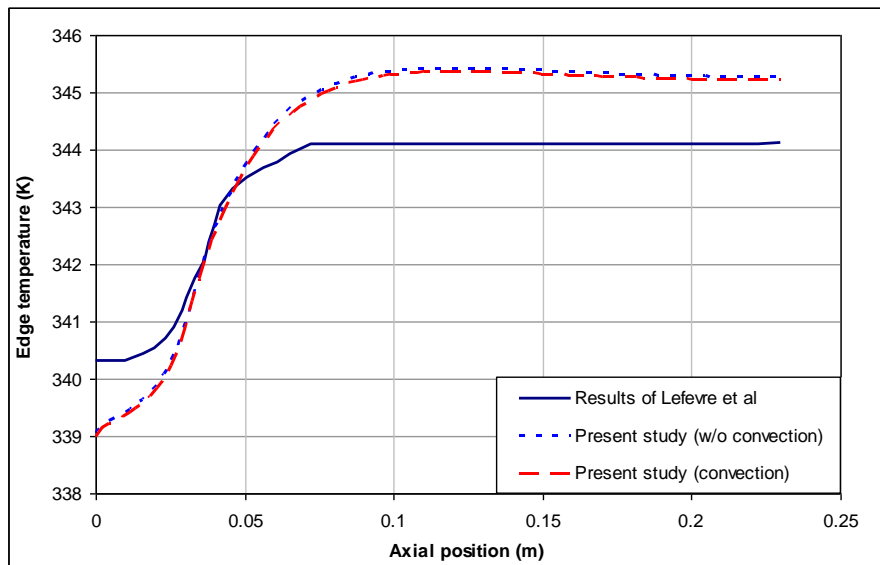


Figure 4.3: Edge temperature variation along the heat pipe axis

The edge temperature variation is given in Figure 4.3, where the difference between the present study and Lefevre *et al.* [6] is about 2 K for both with and

without liquid convection effect, where the maximum value of the difference is located in the evaporation region. Vapor temperature is given as 343 K in [6], where the corresponding values are 342.86 K and 342.83 K for the present study without liquid convection effect and including liquid convection, respectively. The temperature distribution in the solid and liquid domains is shown in Figure 4.4. The axial temperature variation is dominant and the transverse temperature distribution in the solid domain is almost uniform due to the high thermal conductivity of the solid and high value of heat pipe length to depth ratio.

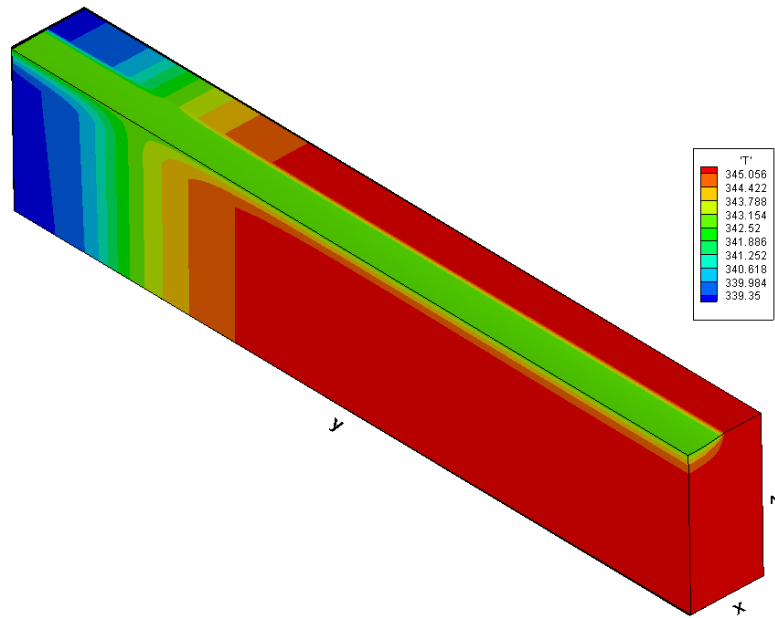


Figure 4.4: 3-D temperature distribution in the liquid and solid regions

As seen in Figure 4.3, there are two discrepancies in the edge temperature between the present study and [6], which are the temperature differences in magnitude for both in the condensation and evaporation regions and the temperature gradient in the condensation region. This condition can be the result of the thermal modeling used in the two studies. An electrical analogy is used to model the heat transfer along the heat pipe axis in [6]. Each cross-section of the heat

pipe was modeled separately, which in turn, was used to calculate the thermal resistance in the transverse direction. Conduction in solid domain was used to obtain the longitudinal resistance. The approach used in thermal modeling for heat source and sink regions are similar, where a constant heat flux was applied along the heat source region and convection boundary condition was defined for the heat sink region. At the liquid–vapor interface a convective boundary condition was defined, where the phase change heat transfer coefficient was defined from the formula derived from kinetic theory. Similar to the present study the liquid film distribution along the fin top was obtained for the condensation region and conduction through the liquid film was considered. For the evaporation region fin top surface was taken adiabatic. In [6], phase change heat transfer coefficient was a function of vapor saturation temperature and pressure, which were constant along the heat pipe axis. Therefore, a constant phase change heat transfer coefficient was used at the liquid–vapor interface for both the evaporation and condensation regions. However, in the present study phase change mass fluxes are calculated directly from kinetic theory rendering them functions of the edge temperature and the solid–liquid contact angle, which change along the heat pipe axis.

In the present study, evaporation from micro and macro regions are considered separately, where in [6] a constant phase change heat transfer coefficient was defined along the liquid–vapor interface. It is seen that coupling of micro region evaporation heat flux for the fin top corner point has a large impact on the temperature distribution along the heat pipe. In the micro region, whose length is about 1 micrometer, evaporation heat flux is obtained and it is distributed along the first control volume in the liquid phase by defining an average phase change heat transfer coefficient, whose value is approximately 1–2 orders of magnitude lower than the value calculated from the formula given in [6]. If the formula given in [6] is applied along the liquid–vapor interface, the temperature distribution at each cross-section on the  $x - z$  plane becomes more uniform and closer to the vapor temperature. For the condensation region the model used in the present study depends also on the contact angle which decreases along the heat pipe axis. As mentioned in Chapter II, condensation mass flux

decreases with decreasing contact angle. At the beginning of the condensation region, the condensation mass flux is high and solid wall temperature should be lower to increase the convective heat transfer to the ambient, which results in a temperature gradient in the condensation region.

One of the advantages of heat pipes is the reduction of the temperature difference between the heat source and heat sink regions. Same amount of heat input used in the validation study is transferred by a copper block, where the axial edge temperature variation is given in Figure 4.5. As shown in the figure the axial temperature difference increases to 138 K, whereas the corresponding difference is 7 K in the heat pipe. The heat pipe solution shows that 86% of the input heat load is transferred by phase change through the heat pipe. Therefore, by causing an approximately constant temperature region on the evaporation region, phase change results in a steeper temperature gradient in the solid, thus effectively increasing the conduction heat transfer in the solid. As a result effectively 15% of the heat input is transferred through one third of the heat pipe length by conduction, which results in 138 K temperature difference, which is consistent with the result given in Figure 4.5.

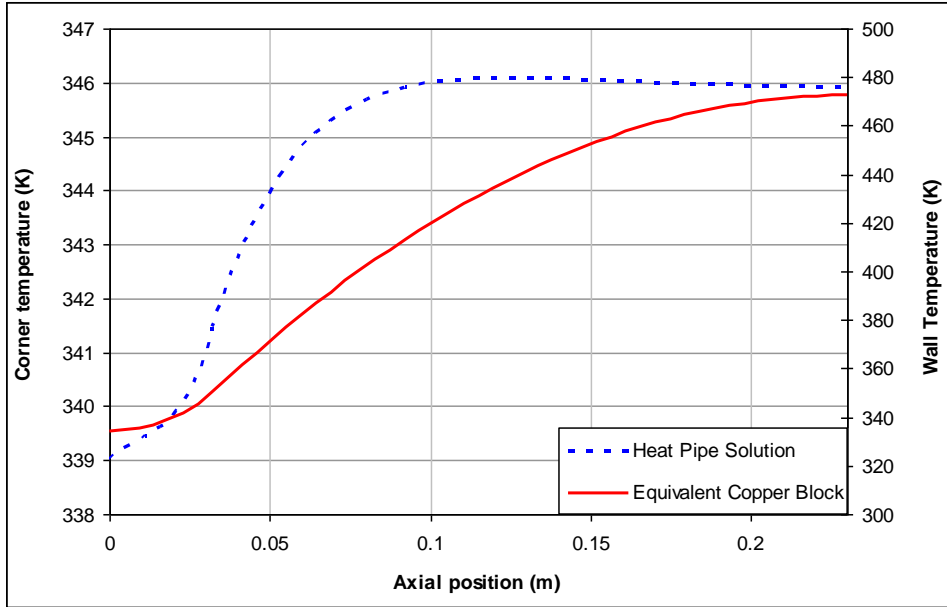


Figure 4.5: Edge temperature variation in the heat pipe and copper block

## 4.2 A Parametric Study of Heat Pipe Performance

A parametric study is conducted to understand the effect of parameters such as heat load, ambient heat transfer coefficient, the radius at the beginning of the condensation region, groove depth and width, fin thickness, the length of heat sink and source region on the liquid–vapor interface radius and the edge temperature variation for the same amount of heat input. In this case the working fluid and heat pipe material are the same as in the validation study, *i.e.* methanol and copper. The dimensions of the groove are different as given in Table 4.2. In this case the heat source region is shorter than the heat sink region. A sample problem is introduced to simulate the cooling of an electronic device on a circuit board. It is seen that heat dissipation rates of CPU’s range from 20–100 W, where the size of the device is approximately 50 mm × 50 mm. Therefore in the parametric study, a heat load of 50 W is applied on a heat source region of 50 mm × 50 mm dimension. The heat transfer coefficient with

the ambient heat transfer coefficient is taken as  $250 \text{ W/m}^2\cdot\text{K}$ , which is typically in the range of forced convection heat transfer. The ambient temperature is set at  $50^\circ\text{C}$ , which is a typical defined maximum operating ambient temperature for electronic components. The case defined in this section is taken as a baseline and the effect of the change in the parameters are explained in the following sections.

Table 4.2: Dimension and physical properties used in the parametric study

Channel length	mm	200
Groove width	mm	0.2
Fin thickness	mm	0.2
Groove thickness	mm	2
Groove depth	mm	0.4
Length of heat source region	mm	50
Length of heat sink region	mm	150
Thermal conductivity of solid	$\text{W/m}\cdot\text{K}$	400
Thermal conductivity of liquid	$\text{W/m}\cdot\text{K}$	0.2
Latent heat of evaporation	$\text{kJ/kg}$	1085
Density of liquid	$\text{kg/m}^3$	792
Dynamic viscosity of liquid	$\text{Pa}\cdot\text{s}$	$3.14 \times 10^{-4}$
Specific heat of liquid	$\text{J/kg}\cdot\text{K}$	2530
Surface tension	$\text{N/m}$	$18.5 \times 10^{-3}$
Molar mass of liquid	$\text{kg/mol}$	$32 \times 10^{-3}$
Molar volume of liquid	$\text{m}^3/\text{mol}$	$42 \times 10^{-6}$
Vapor pressure	Pa	$1.31 \times 10^5$
Heat load	$\text{W/m}^2$	20000
Ambient heat transfer coefficient	$\text{W/m}^2\cdot\text{K}$	250
Ambient temperature	K	323

### 4.2.1 The effect of ambient heat transfer coefficient

Ambient heat transfer coefficient for the baseline case is  $250\text{W}/\text{m}^2\cdot\text{K}$  as given in Table 4.2. This value is increased and decreased by 50%. As given in Figure 4.5, the change in ambient heat transfer coefficient has no considerable effect on the interface radius variation. Since the heat load is constant in all three cases, there is an equal amount of heat input for evaporation, which is the driving force for the heat transfer problem. The iterative process is terminated when the evaporation and condensation mass fluxes equalize in terms of vapor temperature. Higher vapor temperatures and consequently higher edge temperatures (Figure 4.7) are obtained for lower heat transfer coefficients. The analysis is performed to show that operating range of the heat pipe can be adjusted by changing the amount of cooling at the heat sink region.

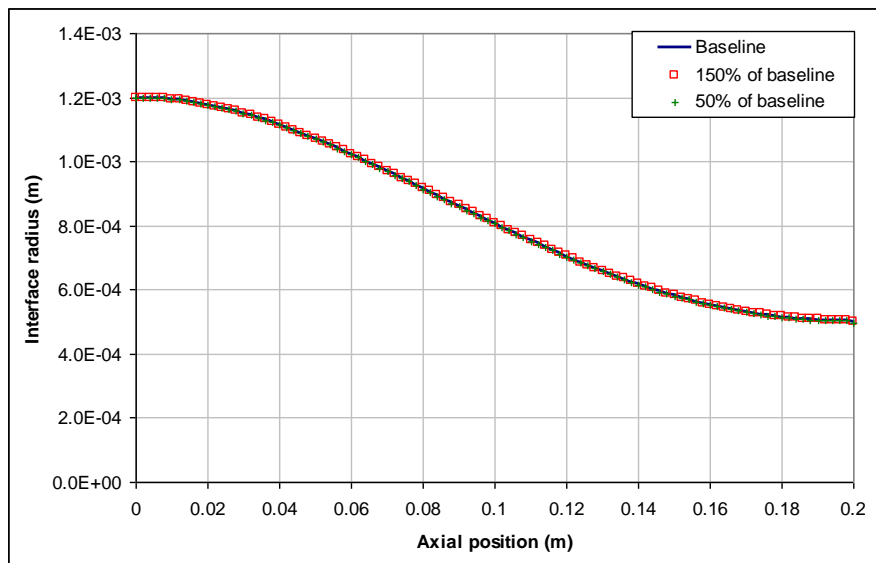


Figure 4.6: Liquid interface radius variation along the heat pipe axis for different ambient heat transfer coefficients

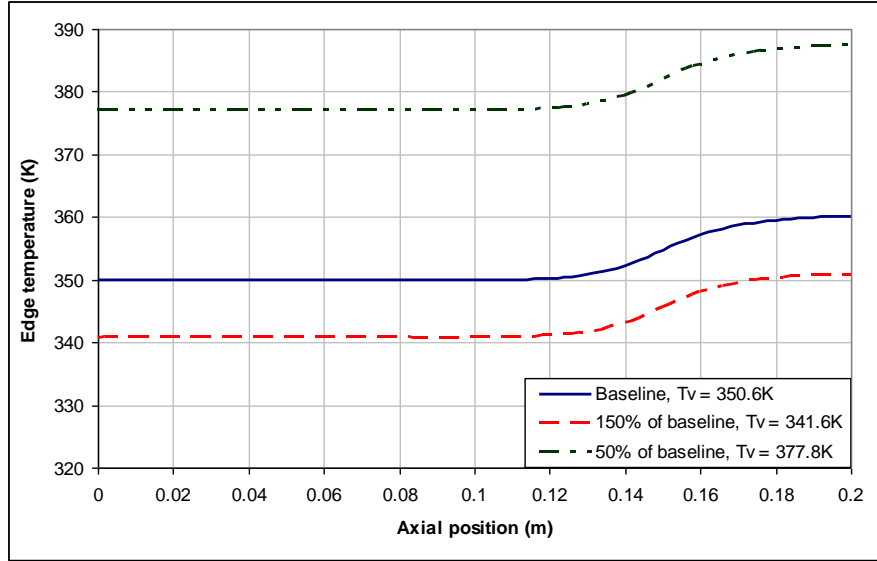


Figure 4.7: Edge temperature variation along the heat pipe axis for different ambient heat transfer coefficients

#### 4.2.2 The effect of solid thermal conductivity

Copper container is used for the baseline analysis whose thermal conductivity is  $400 \text{ W/m}\cdot\text{K}$ . The effect of the thermal conductivity is investigated by reducing the value to  $25 \text{ W/m}\cdot\text{K}$ , which is in the range of that of stainless steel. The variation of the liquid interface radius shows a similar behavior for the two cases (Figure 4.8), where input heat load is identical and consequently so is the evaporation heat transfer. For decreasing thermal conductivity of the container, the contribution of the axial heat transfer decreases and the amount of heat transfer used for phase change increases, which can be seen in the ratio of the heat transferred *via* phase change to the input heat load is 81% for the baseline copper case, which increases to 98% with low solid thermal conductivity. Some previous studies — which did not consider axial heat transfer — assumed that evaporation and condensation regions are constrained with heat source and heat sink regions. However, axial heat transfer causes a smooth transition from condensation to evaporation regions as shown in Figure 4.9. As the thermal conductivity

decreases, this effect also decreases and phase change regions become closer to heat source and sink regions. This condition can be seen as an abrupt change in the edge temperature with decreasing thermal conductivity.

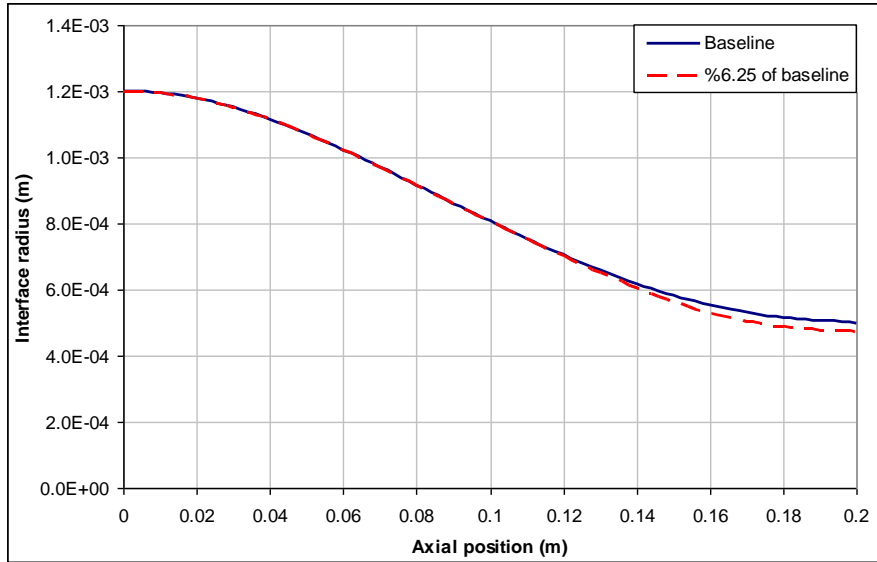


Figure 4.8: Liquid interface radius variation along the heat pipe axis for different solid thermal conductivity

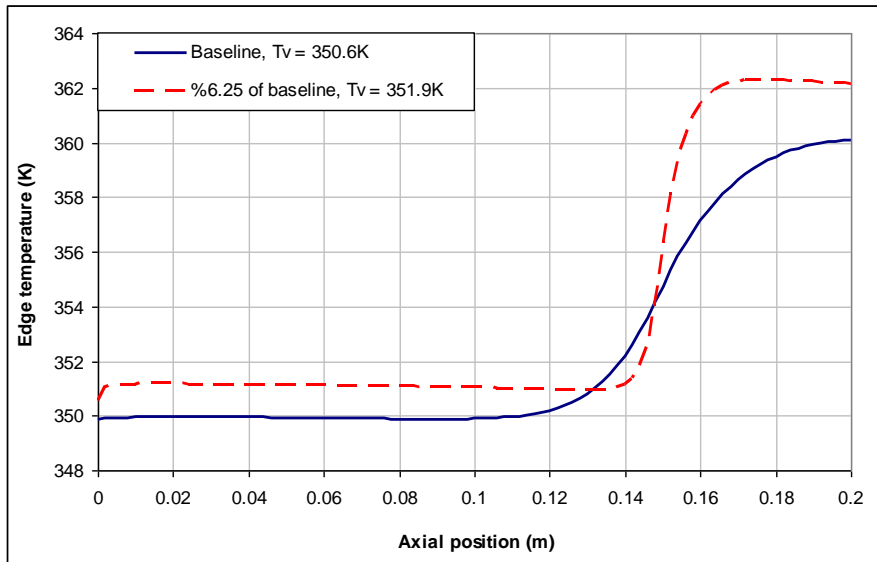


Figure 4.9: Edge temperature variation along the heat pipe axis for different solid thermal conductivity

### 4.2.3 The effect of heat load

Initial heat flux value,  $20\text{kW/m}^2$ , is decreased by 20% and 40% and increased by 20% to investigate the effect of the input heat load. As expected, higher heat loads result in more evaporation and smaller radius is obtained for the evaporation region (Figure 4.10). More evaporation leads to higher temperature differences at the heat sink region, since the same amount of fluid should condensate to satisfy the overall mass balance. Therefore, the vapor temperature ( $T_v$ ) also increases with increasing heat load. As expected, more fluid should be present for higher heat input, which is shown in Figure 4.12.

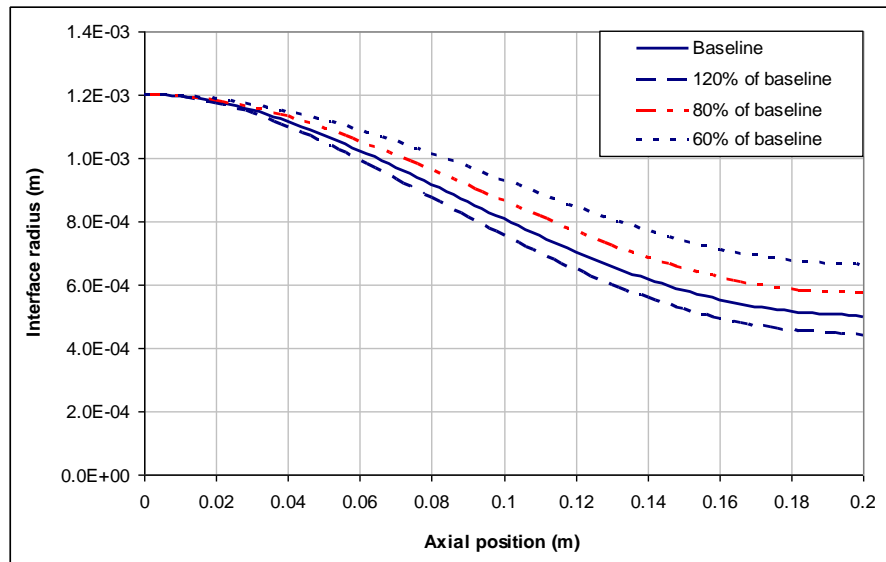


Figure 4.10: Liquid interface radius variation along the heat pipe axis for different heat load values

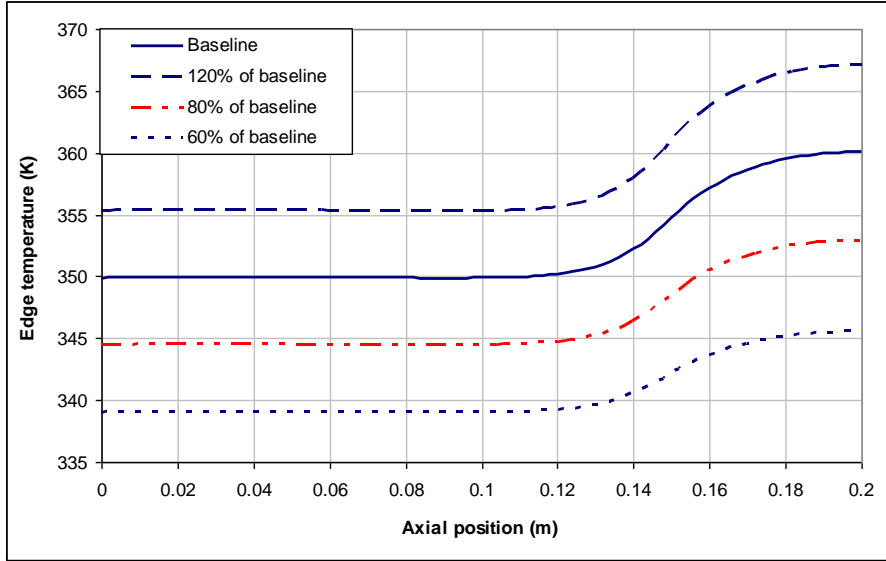


Figure 4.11: Edge temperature variation along the heat pipe axis for different heat load values

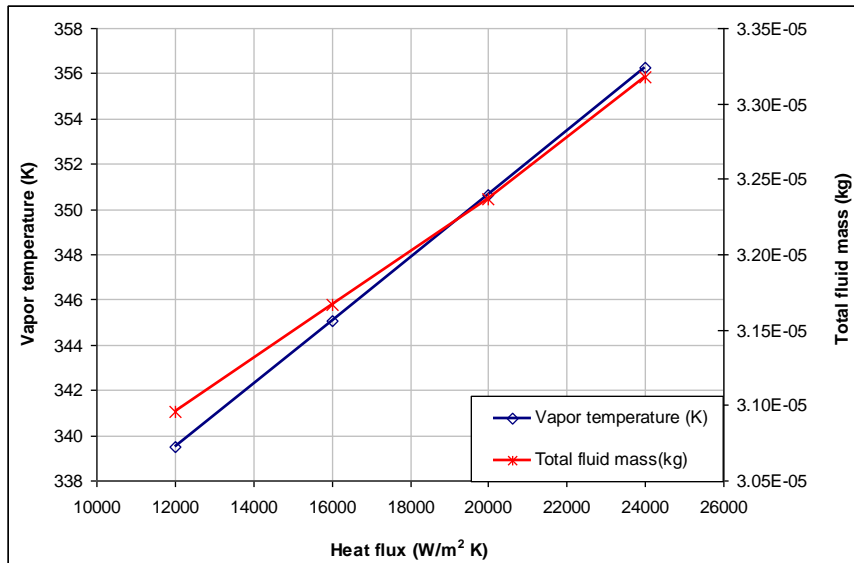


Figure 4.12: Vapor temperature and total fluid mass variation for different heat load values

#### 4.2.4 The effect of initial interface radius

The initial radius is 1200 micrometers for baseline study, which is reduced by 50% and increased by 50% and 200%. The effect of initial interface radius on the variation of the interface radius along the heat pipe is given in Figure 4.13. When the initial radius increases, the change along the heat pipe axis increases, the change is 44% for the case when the initial radius is only 50% of the baseline case; and it increases to 67% when the initial radius is 150% of the baseline case. As mentioned in Chapter II, contact angle is a parameter for phase change modeling. When the interface radius decreases, contact angle decreases, which results in lower condensation but higher evaporation mass fluxes. As the interface radius decreases heat transfer rate for condensation decreases from 0.25 W to 0.23 W. However, heat transfer rate for micro region evaporation increases from 0.06 W to 0.08 W. Therefore, approximately the same amount of heat load is used for phase change, which is about 81% of the heat input. Consequently the change in the edge temperature is not considerable and there is approximately 1 K difference, which can be seen in Figure 4.14 and there is approximately 0.8 K change in the vapor temperature as shown in Figure 4.15. It is expected that increasing initial radius will increase the amount of fluid mass. However, with increasing initial radius the fluid mass in the heat pipe decreases as shown in Figure 4.15. This effect can be explained by the condensed mass on the fin top, since smaller radii result in steeper variation of the liquid film thickness on the fin top as explained in Chapter II Figure 2.9. The integration of the liquid film thickness to calculate the liquid volume on the fin top gives higher values for steeper film thickness variation, which increases overall fluid mass in the heat pipe, even the fluid mass inside the groove decreases with decreasing radius.

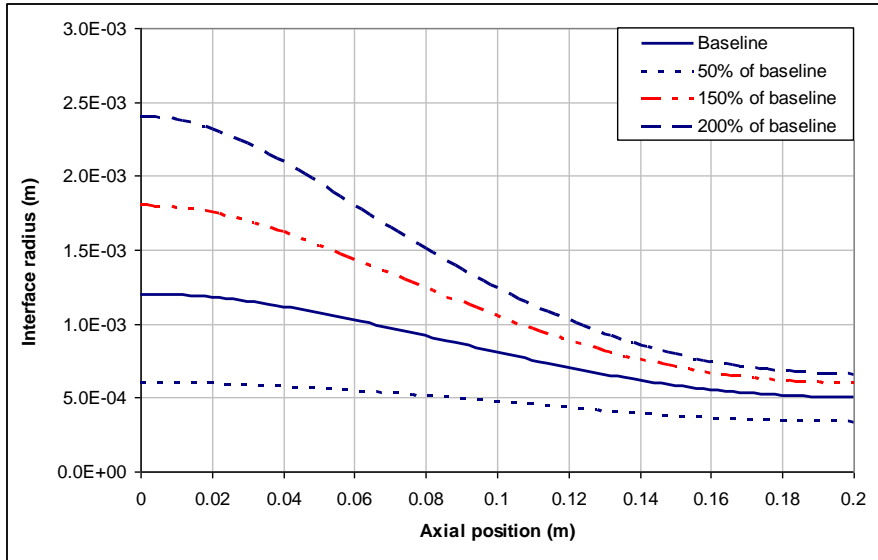


Figure 4.13: Liquid interface radius variation along the heat pipe axis for different initial radius values

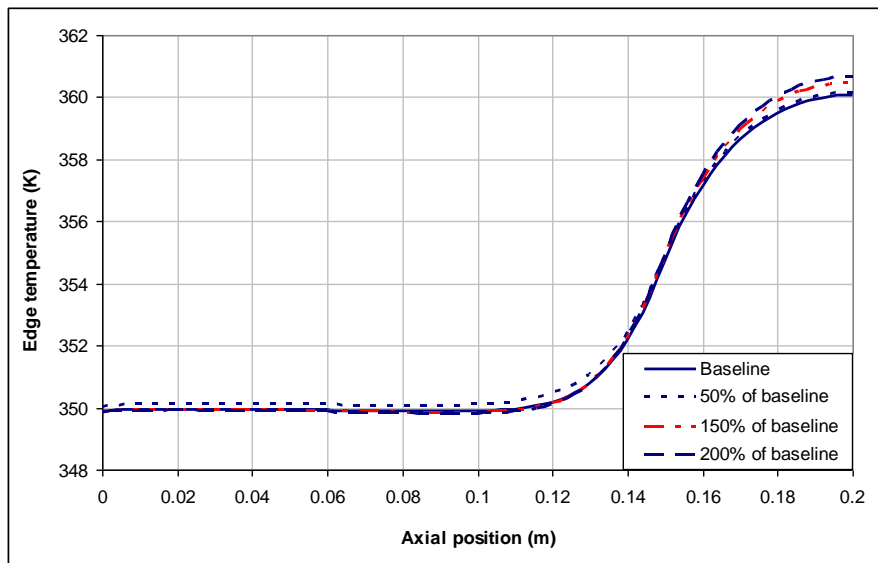


Figure 4.14: Edge temperature variation along the heat pipe axis for different initial radius values

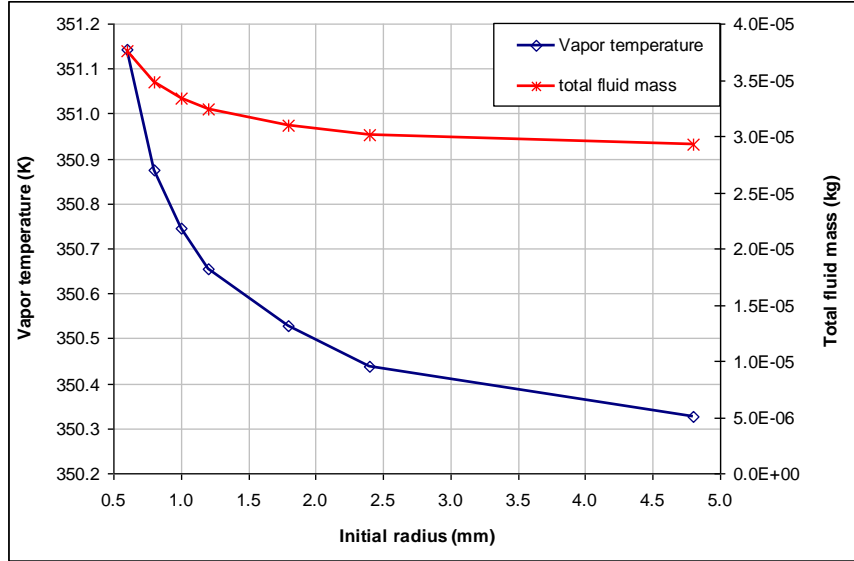


Figure 4.15: Vapor temperature and fluid mass for different initial radius values

#### 4.2.5 The effect of groove depth

Three different groove depth values are investigated, which are 300, 400 and 500 micrometers, where the depth is 400 micrometers for the baseline study. When the depth is larger, the amount of fluid in the heat pipe increases, which generates a larger thermal resistance. Fluid masses in the heat pipe vary between  $2.86 \times 10^{-5}$  kg,  $3.24 \times 10^{-5}$  kg,  $3.78 \times 10^{-5}$  kg from 300 to 500 micrometers groove depths, respectively. The ratio of the heat load for phase change to input heat load increases with decreasing groove depth, whose change is about 2% for this case. As a result, the interface radius is smaller for the 75% of the baseline case (Figure 4.16). However, the edge temperature variation gives almost same distribution for all three cases (Figure 4.17). Although, with increasing groove depths phase change heat transfer from micro region decreases, a larger proportion of the heat load is conducted through the liquid and used in the macro region evaporation. These two effects can be the reason for the approximately constant edge temperature and consequently vapor temperature (Figure 4.17),

which is approximately 350.7 K.

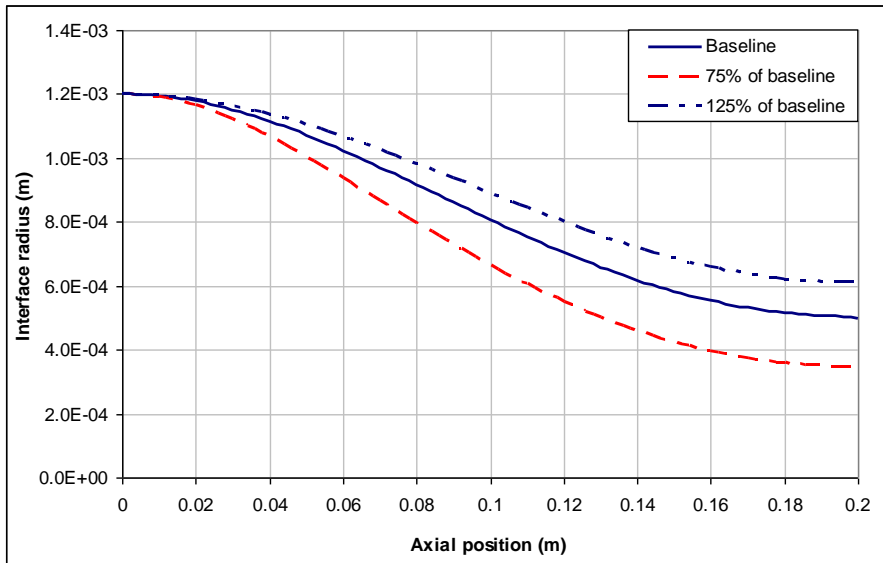


Figure 4.16: Liquid interface radius variation along the heat pipe axis for different groove depths

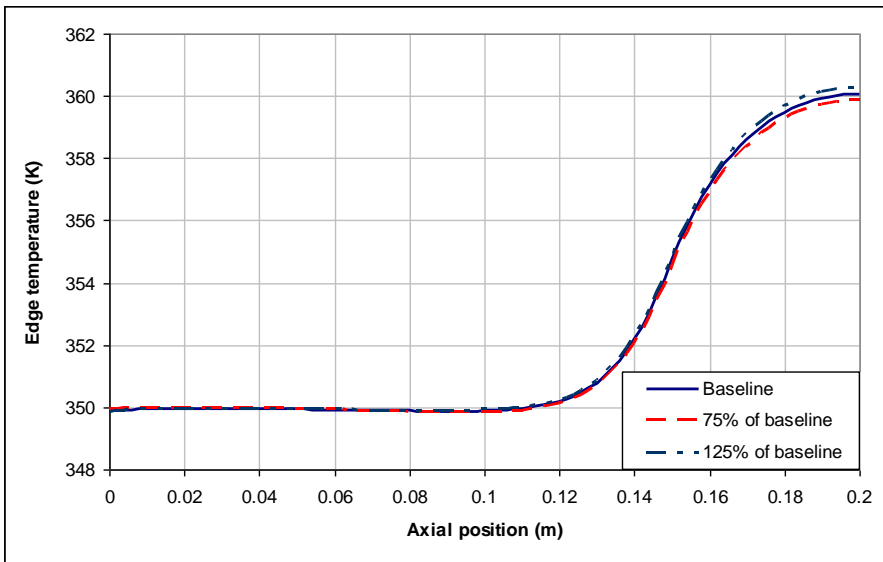


Figure 4.17: Edge temperature variation along the heat pipe axis for different groove depths

#### 4.2.6 The effect of fin thickness

The effect of fin thickness is investigated without changing the groove width, where the fin thicknesses are 400, 200 and 100 micrometers, where the 200 micrometers is used in the baseline study. As given by Zhang and Faghri [52] a decrease in fin thickness results in a thinner condensation layer on the fin top, which causes higher heat flux values and overall heat transfer depends on the integration of the flux values along the fin top. For the present case, increasing fin thickness results in an increase in the condensation heat transfer rate, which results in an increase in the evaporation heat transfer rate since the overall energy balance should be satisfied at the end of the solution procedure. The effect can be seen in the interface radius variation given in Figure 4.18. The interface radius for the fin thickness of 400 micrometers has the smallest value at the end of the heat pipe axis. Since the condensate mass on the fin top increases with increasing thickness, total fluid mass in the heat pipe has the largest value at 400 micrometers, where the values are  $6.34 \times 10^{-5}$ kg,  $3.24 \times 10^{-5}$  kg and  $2.62 \times 10^{-5}$ kg for 400, 200 and 100 micrometers, respectively. Changing fin thickness does not affect the edge temperature in the condensation region, whereas the temperature in the evaporation region has higher values for increased fin thickness (Figure 4.19). The result is compatible with increased evaporation heat transfer for larger fin thicknesses.

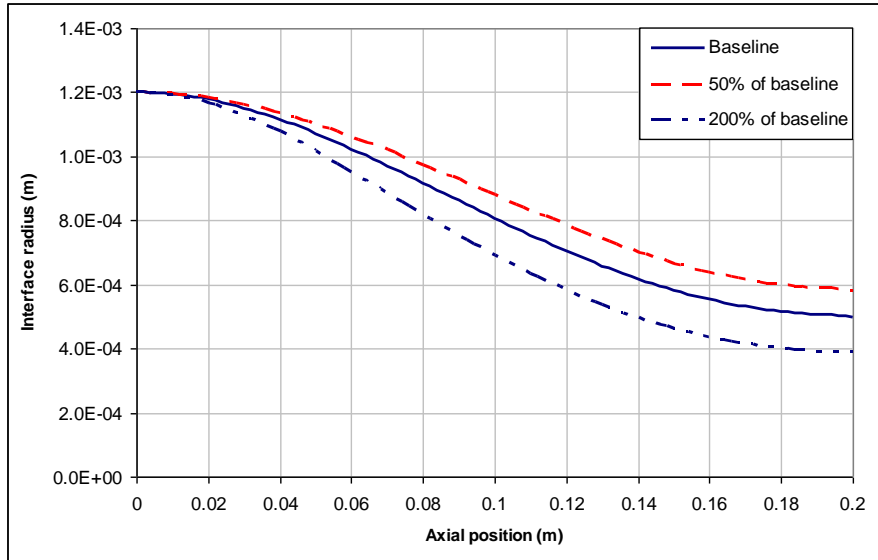


Figure 4.18: Liquid interface radius variation along the heat pipe axis for different fin thickness

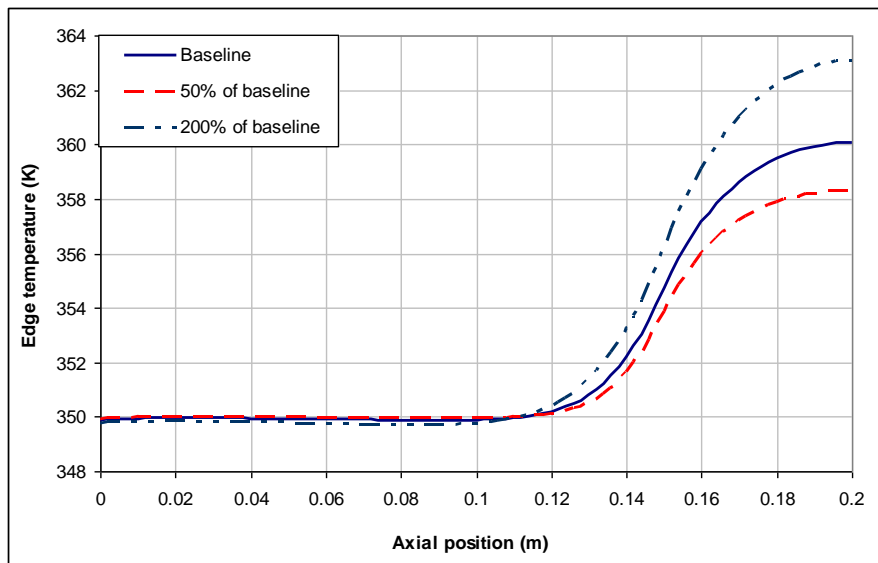


Figure 4.19: Edge temperature variation along the heat pipe axis for different fin thickness

#### 4.2.7 The effect of groove width

For this section the effect of the groove width is investigated, where the groove widths are 400, 200 and 100 micrometers, where 200 micrometers is used for the baseline study. The fluid mass inside the heat pipe is  $5.58 \times 10^{-5}$  kg,  $3.24 \times 10^{-5}$  kg,  $2.44 \times 10^{-5}$  kg for 400, 200 and 100 micrometers, respectively. Since by decreasing the groove width, the fluid mass inside the heat pipe decreases, a larger portion of the heat load is used for phase change. The ratios of the phase change heat transfer to the input heat load are 86%, 81% and 76% for 100, 200 and 400 micrometers groove widths, respectively. Due to increase in the phase change heat transfer for smaller grooves, the interface radius for 100 micrometers groove width gets the smallest value at the end of the heat pipe axis (Figure 4.20). The edge temperature variation is given in Figure 4.21, where different values of groove widths only affect the temperature in the evaporation region.

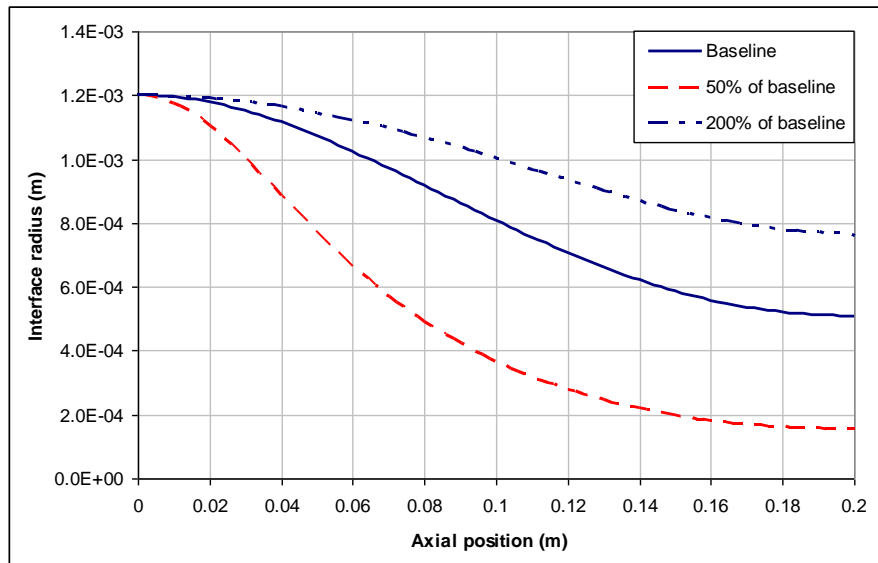


Figure 4.20: Liquid interface radius variation along the heat pipe axis for different groove width

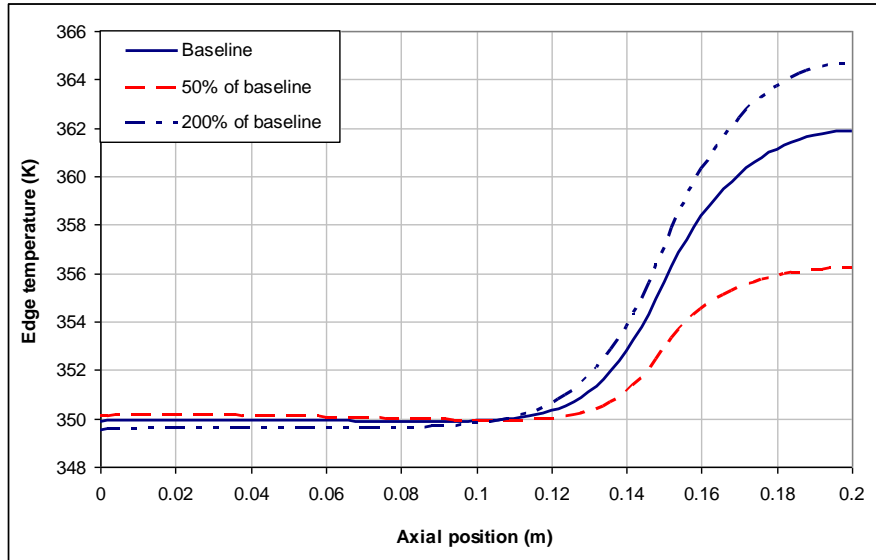


Figure 4.21: Edge temperature variation along the heat pipe axis for different groove width

#### 4.2.8 The effect of working fluid

Thermophysical properties of the working fluids define phase change characteristics and operational range of the heat pipe. To show this effect three different working fluids compatible with copper container are analyzed. The physical properties are given in Table 4.3. Latent heat of evaporation of methanol, which is the baseline for this study, is about half of that of water, therefore there is more evaporating mass in the case of methanol, whose effect can be seen in the interface radius variation given in Figure 4.22. It is expected that evaporated mass of ammonia becomes larger than methanol, since the latent heat of ammonia is lower than that of methanol. The heat flow rate used for evaporation is 0.35 W for ammonia and 0.32 W for methanol and this difference does not result in a considerable difference in the interface radius.

Table 4.3: Thermophysical properties of working fluids

		Methanol	Water	Ammonia
Thermal conductivity	W/m·K	0.2	0.67	0.36
Latent heat of evaporation	kJ/kg	1085	2308	895
Density	kg/m <sup>3</sup>	792	972	512
Dynamic viscosity	Pa·s	$3.14 \times 10^{-4}$	$3.51 \times 10^{-4}$	$8.32 \times 10^{-5}$
Surface tension	N/m	$18.51 \times 10^{-3}$	$62.69 \times 10^{-3}$	$9.6 \times 10^{-3}$
Molar mass	kg/mol	$32 \times 10^{-3}$	$18 \times 10^{-3}$	$17 \times 10^{-3}$
Molar volume	m <sup>3</sup> /mol	$42 \times 10^{-6}$	$18 \times 10^{-6}$	$33 \times 10^{-6}$
Specific heat	J/kg·K	2530	4197	5639
Vapor Pressure	Pa	$1.31 \times 10^5$	$0.47 \times 10^5$	$3.86 \times 10^6$

Thermal conductivity of the working fluid affects heat transfer in the liquid domain and temperature distribution along the heat pipe wall. Higher thermal conductivity values, as given for water here, result in a lower temperature difference between the evaporation and condensation region, which is 5 K for water and 10 K for methanol (Figure 4.23). This behavior can be also seen for ammonia, the temperature difference between the evaporation and condensation regions is reduced to 6 K.

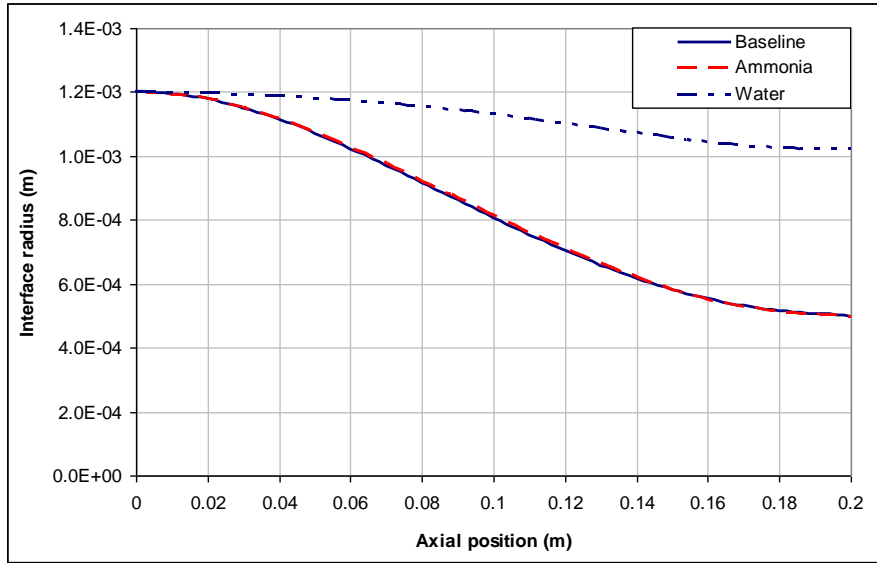


Figure 4.22: Liquid interface radius variation along the heat pipe axis for different working fluids

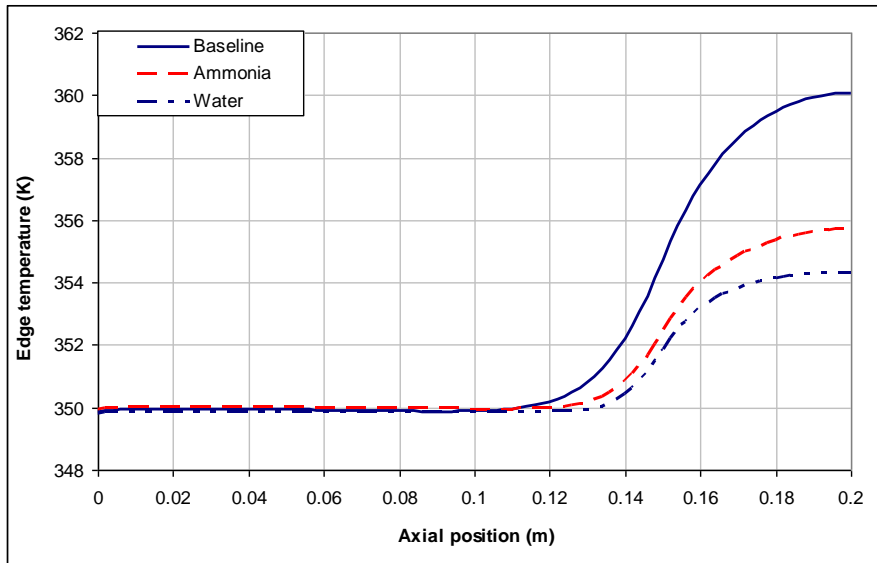


Figure 4.23: Edge temperature variation along the heat pipe axis for different working fluids

#### 4.2.9 The effect of heat source and sink region length

The effect of different heat source and heat sink lengths are studied in this section for the same total heat input. The cases are summarized in Table 4.4. Addition of an adiabatic region between the two ends increases the effectiveness of the heat pipe, where the ratio of phase change heat transfer to the heat input is 81% for baseline case, the ratio increases to 97% for a 50mm adiabatic region and 99% for a 75mm adiabatic region. The 150 mm heat source case is similar to the validation problem. For this case the interface radius is smaller at the end of the evaporation region compared to the baseline case, but it is larger than the cases with adiabatic regions as shown in Figure 4.24. The advantage of this case is the reduction in temperature difference between the evaporator and condenser sides, which is 6 K as opposed to the baseline 10 K difference (Figure 4.25). However, the ratio of phase change heat transfer to input heat is 84% and smaller than the cases with adiabatic regions.

Table 4.4: Dimensions of heat source, heat sink and adiabatic regions

	Heat Source Length (mm)	Adiabatic Region Length (mm)	Heat Sink Length (mm)
Baseline	50	–	150
50mm adiabatic region	50	50	100
75mm adiabatic region	50	75	25
150mm heat source region	150	–	50

As seen in Figure 4.25, the lengths of evaporation and condensation regions change according to the boundary conditions, which are the lengths of the heat source and heat sink in this case. In the heat pipe, there is a smooth transition

from condensation to evaporation region due to axial heat transfer and there is no definite adiabatic region in the heat pipe, eventhough at the external boundary a region with an adiabatic boundary condition is defined.

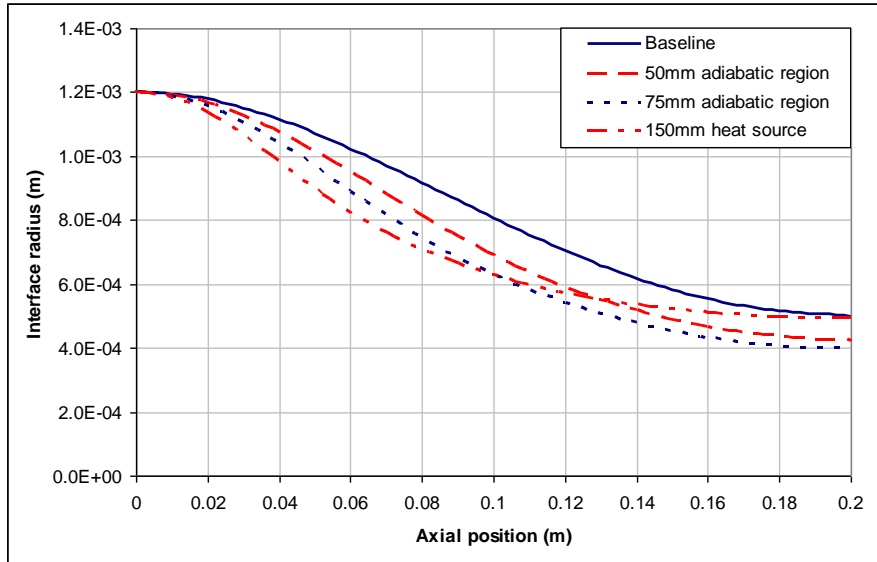


Figure 4.24: Liquid interface radius variation along the heat pipe axis for different heat sink and source lengths

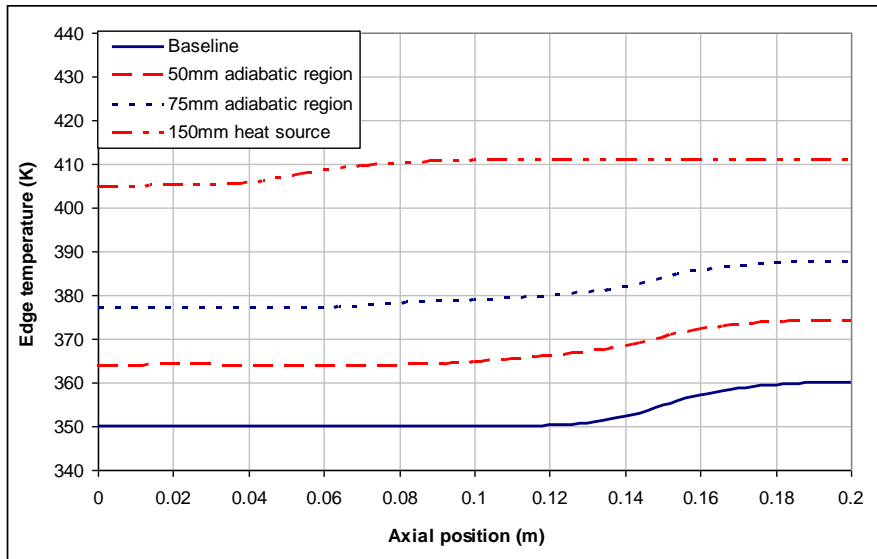


Figure 4.25: Edge temperature variation along the heat pipe axis for different heat sink and source lengths

### 4.3 Maximum Heat Capacity of the Heat Pipe

In section 4.2, a constant amount of heat load is applied and the effect of geometric and physical parameters on the interface radius and the edge temperature is studied. In this section the maximum heat capacity of the heat pipe is investigated. Since for the present model, the analysis for axial momentum starts from the condensation region and ends at the evaporation region, it is not possible to find the minimum interface radius at the end of the evaporation region directly. However, minimum radius can be defined by the geometry and solid–liquid contact angle, which is unique for a specific heat pipe material and working fluid combination,

$$R_{min} = \frac{b}{\cos \theta} \quad (4.1)$$

The contact angle is approximately 40 degrees for copper–methanol combination [6]. Therefore, the input heat load is increased gradually to obtain 40 degrees at the end of the evaporation region, when dry-out conditions starts to prevail.

#### 4.3.1 Fixed total length of fin thickness and groove width

For this analysis the baseline case has the same geometry and boundary conditions used in Section 4.2. Total length of the fin thickness and groove width is 400 micrometers, which is kept constant. Different values of groove width to fin thickness ratios are analyzed. Since the total length is constant, number of grooves is fixed for a given heat pipe size. The variation for the maximum heat flux and vapor temperature is given Figure 4.26. Maximum heat flux increases where the width to thickness ratio reaches the value of three and further increase in the ratio does not change the maximum heat transfer value, where similar behavior can be seen in the vapor temperature variation. Evaporation heat transfer rate from micro region increases until the ratio reaches the value of three, but then it starts to decrease. On the other hand, the heat transfer rate from macro evaporation continues to increase, which compensates the increasing

value of the condensation heat transfer rate. The ratio of the phase change heat transfer to the input heat load is almost constant, where the value is 81% for this section.

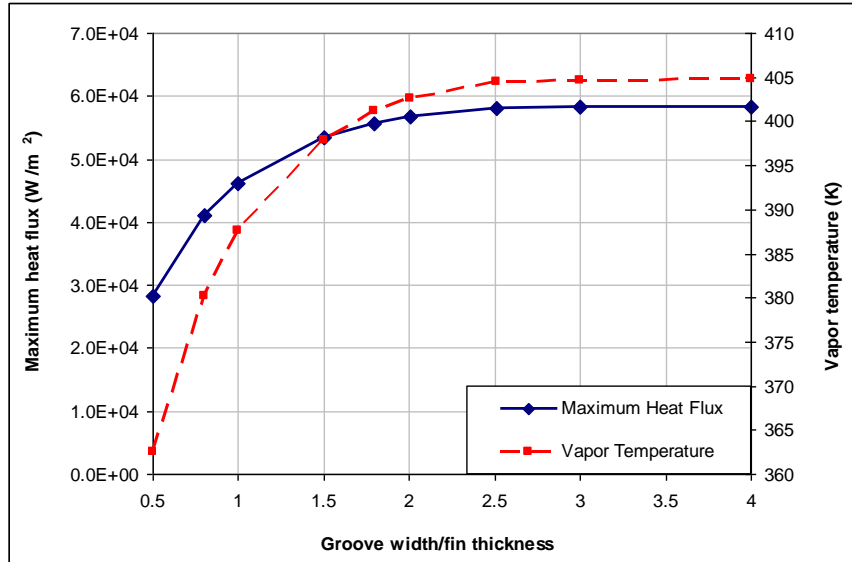


Figure 4.26: Maximum heat flux and the vapor temperature variation for different groove width to fin thickness ratios

The variation of the total fluid mass in the heat pipe is given in Figure 4.27. The overall fluid mass decreases until the ratio reaches the value of two and after that value it starts to increase. Total fluid mass includes the fluid in the groove and the condensate mass on the fin top. Increasing groove width also causes an increase in the fluid mass in the groove, however, the condensate mass on the fin top decreases. After the groove width to fin thickness ratio reaches the value of two, the increase in the groove mass dominates and the overall effect can be seen as an increase in the fluid mass. The ratio of the total fluid volume to the groove volume is also given in Figure 4.27, where increasing groove volume determines the behavior and a continued decrease in the volume ratio can be seen.

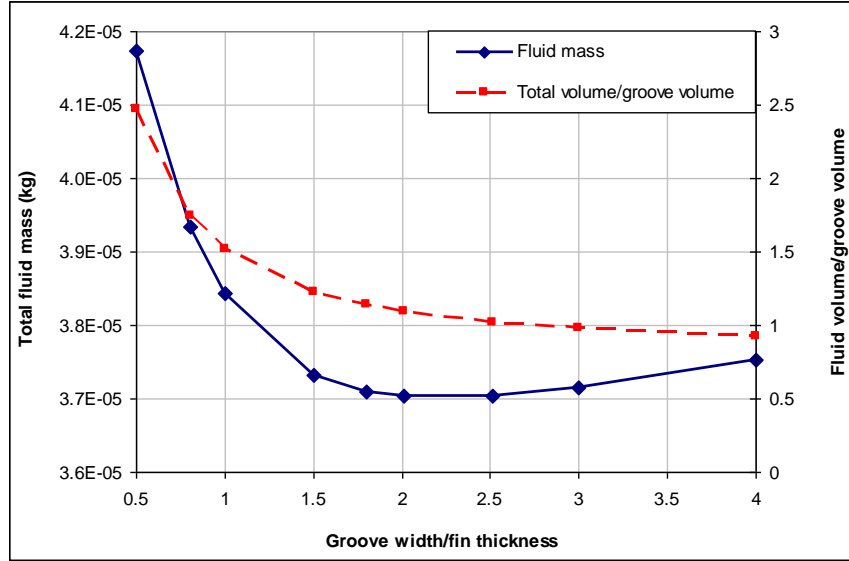


Figure 4.27: Fluid mass for different groove width to fin thickness ratios

#### 4.3.2 Effect of different groove width and depth for fixed fin thickness

In the second case, groove width and depth values are changed, where the fin thickness is taken as a constant of 200 micrometers. Groove width varies from 150 to 400 micrometers and the groove depth range is 250 to 600 micrometers. Maximum heat flux variation for different groove width and depth combinations are shown in Figures 4.28–4.30. The initial value of the liquid interface radius is also varied between 0.9 to 2.4 mm. As given in Figures 4.28–4.30 for a fixed groove width (solid lines), the increase in groove depth causes an increase in the maximum heat flux values. For a fixed groove depth value (dash lines) an increase in groove width causes an increase in the maximum heat flux to a peak value after which the maximum heat flux starts to decrease again. As the groove width increases, evaporation heat transfer from micro region decreases, whereas evaporation from macro region continues to increase and compensate condensation. After a certain value, heat transfer from macro region also starts to decrease. The decreasing ratio of the phase change heat transfer rate to the

input heat load also supports this behavior.

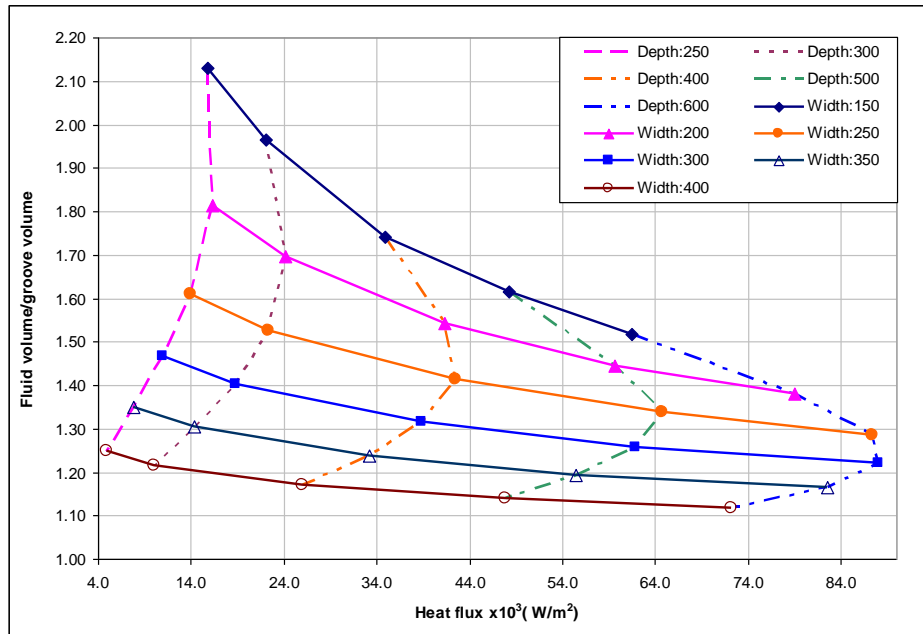


Figure 4.28: Maximum heat flux variation for different groove depths and widths for an initial radius of 0.9 mm.

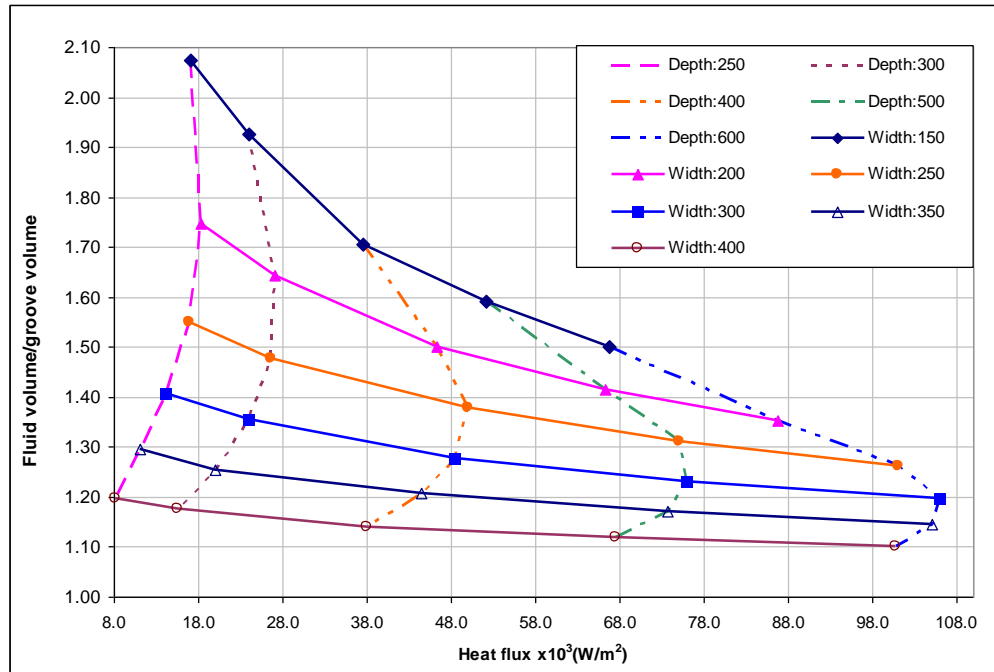


Figure 4.29: Maximum heat flux variation for different groove depths and widths for an initial radius of 1.2 mm.

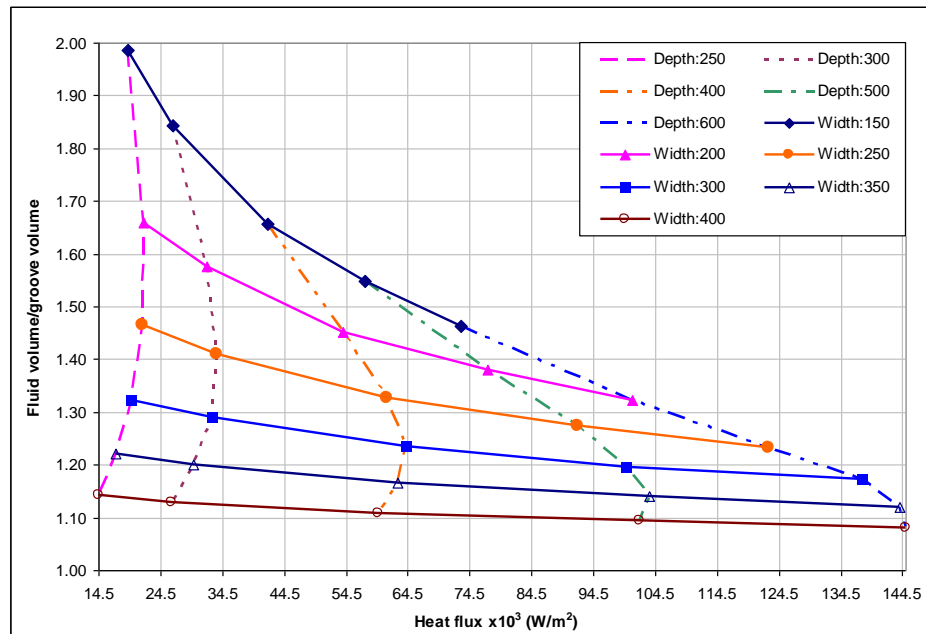


Figure 4.30: Maximum heat flux variation for different groove depths and widths for an initial radius of 2.4 mm.

The effect of the increase in the initial liquid interface radius can also be seen in Figures 4.28–4.30, where the maximum heat flux increases.

Total fluid mass variation for different groove depths, widths and initial interface radius is given in Figure 4.31. The groove depth and width is normalized by the baseline dimensions, where the groove depth is 400 micrometers and groove width is 200 micrometers. As expected, fluid mass increases as the groove depth and width increases for all values of the initial radius.

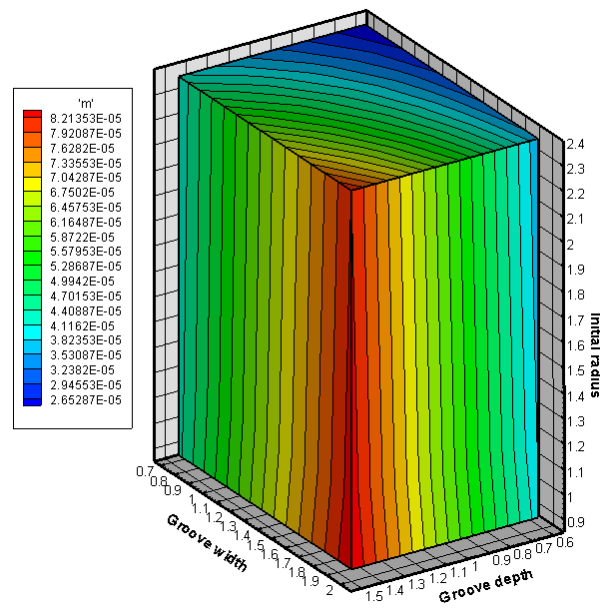


Figure 4.31: Total fluid mass variation for different groove depths and widths

Maximum heat flux and vapor temperature variation is given in Figure 4.32, where both variations show similar behavior in terms of groove depth, width and radius.

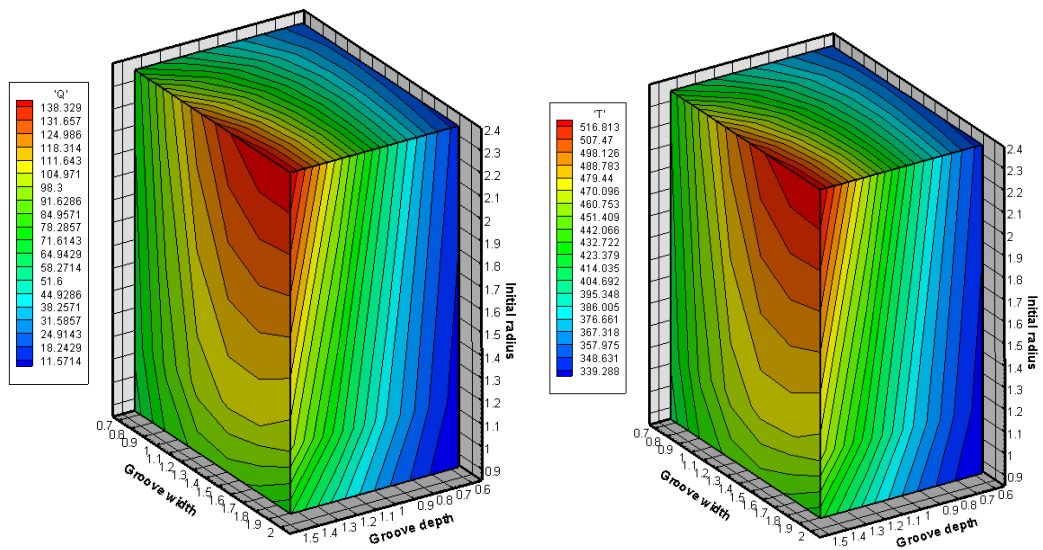


Figure 4.32: Maximum heat flux and vapor temperature variation for different groove depths and widths

Maximum heat flux variation for a constant groove depth and width values are given in Figure 4.33. The results given in Figures 4.28–4.30 can also be seen here, where for constant groove width heat flux increases with the groove depth. For a constant groove depth, as the groove width increases heat flux increases to a maximum value and starts to decrease, where higher heat flux values are obtained for deeper grooves.

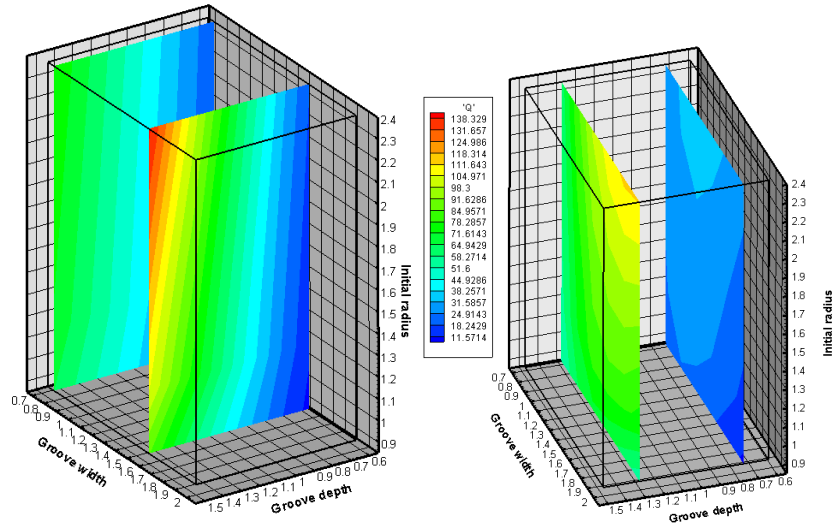


Figure 4.33: Maximum heat flux variation for constant groove depth and width values

For a practical problem, heat dissipation of an electronic component can be defined and using this constraint the size of the grooves, total fluid mass and the temperature can be found from a surface given in Figure 4.34. In another case the temperature can be the constraint and for a certain value, heat transfer capacity, size and total fluid mass can be decided from such a surface given in Figure 4.35.

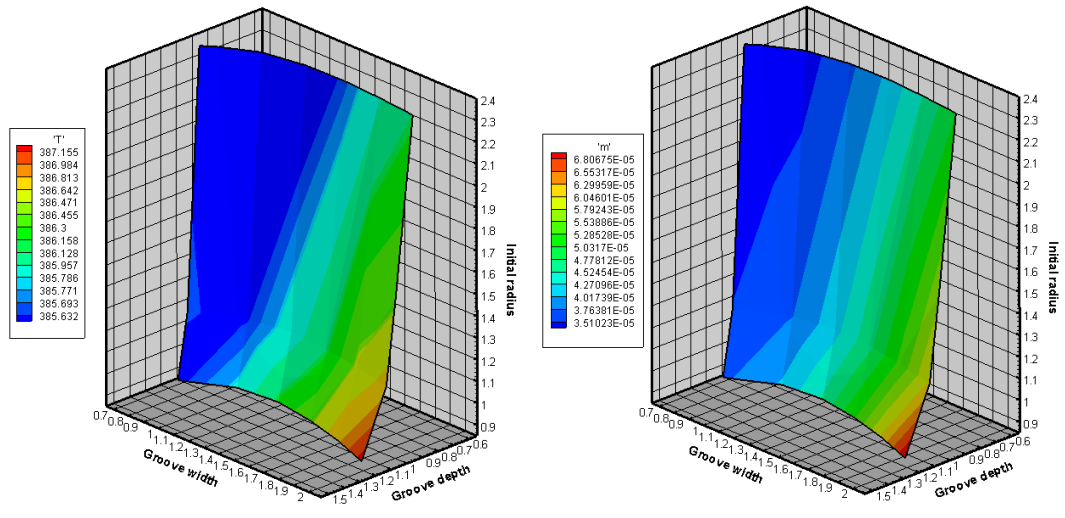


Figure 4.34: Total fluid mass and temperature variation for  $35000 \text{ W/m}^2$

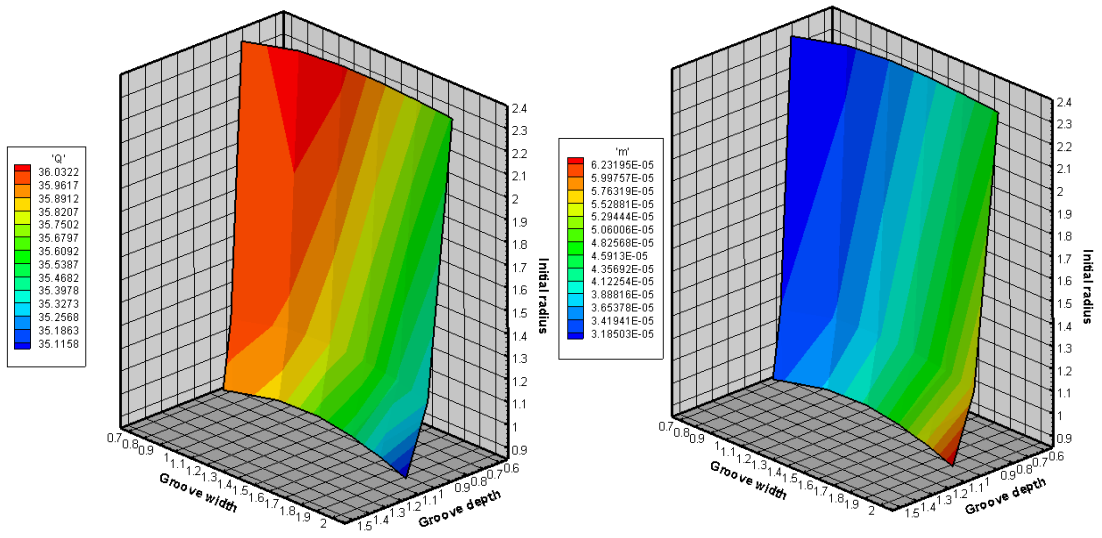


Figure 4.35: Maximum heat flux and total fluid mass distribution for vapor temperature 393 K

### 4.3.3 Effect of different heat pipe length

The effect of the heat pipe length on the maximum heat transfer capacity is investigated in this section. For this study, the length of the heat source and sink regions are taken equal, where the ratio of the heat source/sink length to the total length is set as 0.3. As given in Figure 4.36, heat transfer capacity decreases with increasing length. For longer heat pipes, solid-liquid interface shear increases and due to higher friction dry-out limit is reached for lower input heat loads. Total fluid mass increases with heat pipe length as expected, but the ratio of the total fluid volume to the groove volume decreases.

Maximum heat transfer capacity is also investigated for different values of heat source to total heat pipe length ratio, where the length of heat sink is assumed to be equal to the source. As the ratio increases, maximum heat transport capacity decreases, where the adiabatic section length decreases. This result is in line with the results given in Section 4.2.9, where decreasing adiabatic section length causes a reduction in the heat transfer rate used for phase change.

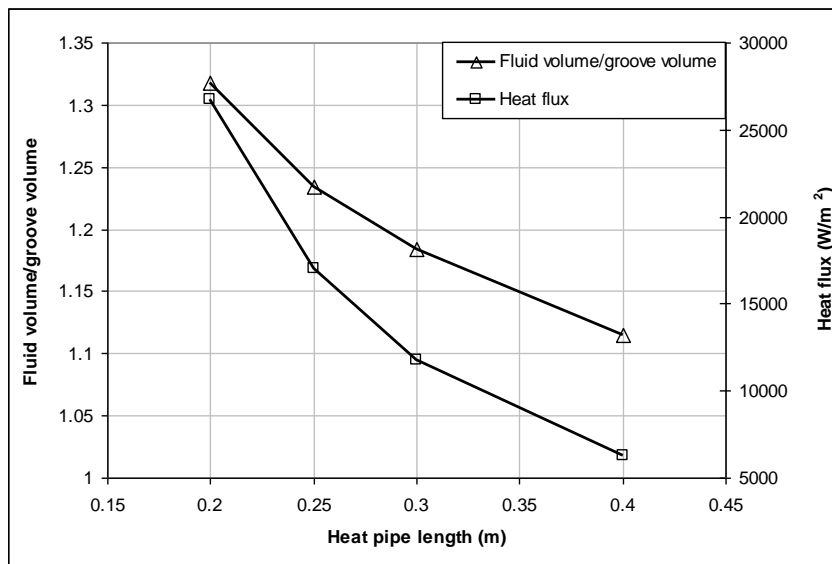


Figure 4.36: Maximum heat flux variation for different heat pipe lengths

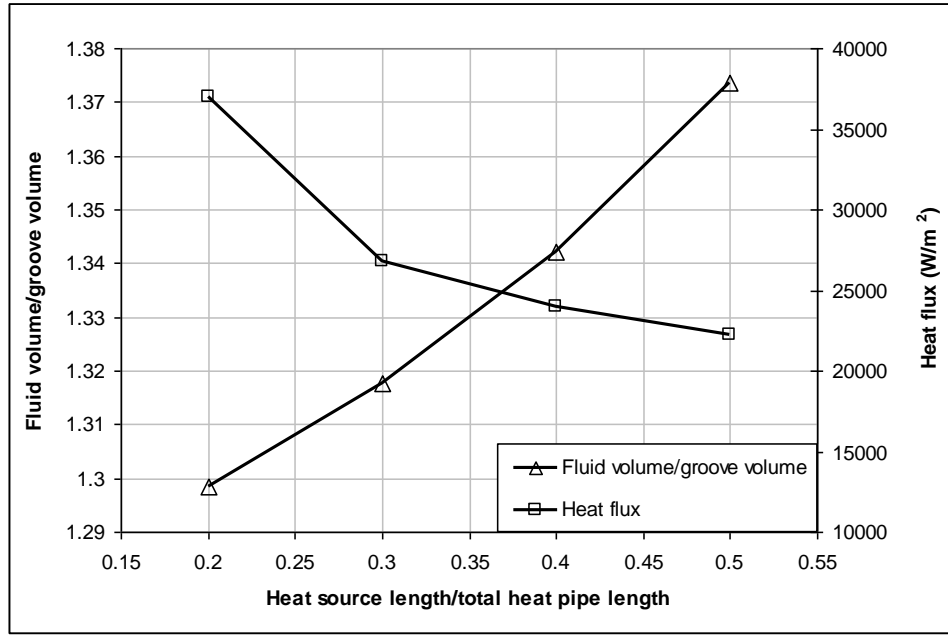


Figure 4.37: Maximum heat flux variation in terms of heat source length to heat pipe length ratio



## CHAPTER 5

### DESIGN PROBLEM

In Chapter IV a parametric study was carried out using the present heat pipe model to understand the effects of the geometric parameters and physical properties on the performance of heat pipe and to develop a methodology for the design of a flat grooved heat pipe to carry out defined operational tasks. By using the results obtained in the previous chapter, a sample problem is introduced, where the parameters will be determined according to the defined maximum operating temperature.

#### 5.1 Definition of the Design Problem

To select a heat pipe the following steps and parameters can be defined as a general procedure.

- Define heat load
- Define heat source size
- Define possible heat sink position and size
- Define heat sink cooling method and heat transfer capacity
- Define heat sink temperature
- Define operational temperature range for the component

- Define a working fluid according to operational temperature range
- Select a container compatible with the working fluid
- Determine the size of the grooves (depth, width and thickness) to operate within the defined operational temperature
- Determine the amount of fluid to be filled into the heat pipe

A sample problem is introduced to simulate the cooling of an electronic component on a circuit board. Heat dissipation rate is set as 40 W and the size of the electronic component is 40 mm×40 mm. Copper heat pipe container with methanol as the working fluid is used. Component size is a given design constraint and determines the size of the evaporation region or heat source length. A constant ambient heat transfer coefficient is defined for the heat sink region, since it is assumed that the overall cooling of the board is provided by a fixed means *e.g.* fan cooling. The ambient is at 50°C (323 K). The design objective is to operate under a defined maximum evaporation region temperature, which represents the maximum allowable operating temperature of the component. In this case the maximum allowable operating temperature used is 82° (355 K). The physical and geometric parameters are listed in Table 5.1.

Table 5.1: Dimension and physical properties used for design problem

Fixed given parameter	Channel length	mm	200
	Groove thickness	mm	1.0
	Length of heat source region	mm	40
	Heat load	W/m <sup>2</sup>	25000
	Ambient heat transfer coefficient	W/m <sup>2</sup> ·K	250
	Ambient temperature	mm	323
Physical parameters	Thermal conductivity of solid	W/m·K	400
	Thermal conductivity of liquid	W/m·K	0.2
	Latent heat of evaporation	kJ/kg	1085
	Density of liquid	kg/m <sup>3</sup>	792
	Dynamic viscosity of liquid	Pa·s	$3.14 \times 10^{-4}$
	Specific heat of liquid	J/kg·K	2530
	Surface tension	N/m	$18.5 \times 10^{-3}$
	Molar mass of liquid	kg/mol	$32 \times 10^{-3}$
	Molar volume of liquid	m <sup>3</sup> /mol	$42 \times 10^{-6}$
	Vapor pressure	Pa	$1.31 \times 10^5$
Geometric parameters used for design	Length of heat sink region	mm	100
	Groove width	mm	0.2
	Fin thickness	mm	0.2
	Groove depth	mm	0.4
	Number of grooves		50

## 5.2 Result for the Design Problem

For the sample problem it is assumed that other parameters except the physical dimension of the groove geometry is defined as given in Table 5.1. Without groove dimensions it is not possible to model the heat pipe, therefore arbitrary initial values for the groove geometry are assumed, which is the “baseline” case

for this problem. Using the baseline parameters an initial value of the edge temperature variation is obtained, which represents the operating temperature of the electronic component. The result is investigated and is used to determine how to change the other parameters. At each trial, which is called a “test case”, the changed parameters are listed in Table 5.2.

Table 5.2: Test cases for the design problem

Case	Fin Thickness (mm)	Groove width (mm)	Groove depth (mm)	Initial Radius (mm)	Heat Sink Length (mm)
Baseline	0.2	0.2	0.4	1200	100
Case1	0.25	0.15	0.4	1200	100
Case2	0.1	0.3	0.4	1200	100
Case3	0.1	0.1	0.4	1200	100
Case4	0.1	0.1	0.4	1200	160

For the baseline study the vapor temperature ( $T_v$ ) is obtained as 364 K and the edge temperature varies from 362 K to 376 K from the condensation region to the evaporation region along the heat pipe (Figure 5.2). In Case 1 fin thickness is increased from 0.2 mm to 0.25 mm, where the groove width is reduced to 0.15 mm. In chapter IV it was seen that increasing the fin thickness causes an increase in the edge temperature, but decreasing groove width results in a decrease in the edge temperature. It is seen that, this change reduces the edge temperature only by 2 K. For Case 2, the fin thickness is reduced to 0.1 mm, where the groove width is increased to 0.3 mm. In Case 2 the edge temperature in the evaporation region increased by 1 K with respect to the baseline case. In Case 3, both fin thickness and groove width are reduced to 0.1 mm, which increases the number of grooves from 50 to 100 for the fixed size electronic component. In Case 3, the edge temperature variation along the heat pipe

drops to 363–368 K. However, the result is not sufficient, because the defined design temperature of 355 K cannot be obtained. All three cases do not provide an acceptable change for the temperature. Moreover, in Chapter IV, it was seen that changing the initial radius and the the groove depth did not affect the edge temperature considerably. Therefore, the length of the heat sink region is increased to 160 mm, where adiabatic region length of 60 mm in the baseline case is also used for cooling. In section 4.2.9 it was shown that decreasing the length of adiabatic region results in a decrease in the edge temperature. The edge temperature range is reduced to 346–353 K for Case 4, which is just below the defined maximum allowable operating temperature and total fluid mass to be filled in the heat pipe is 2.9 grams.

The variation of the interface radius is given in Figure 5.1 and maximum edge temperatures for each test case are summarized in Figure 5.3.

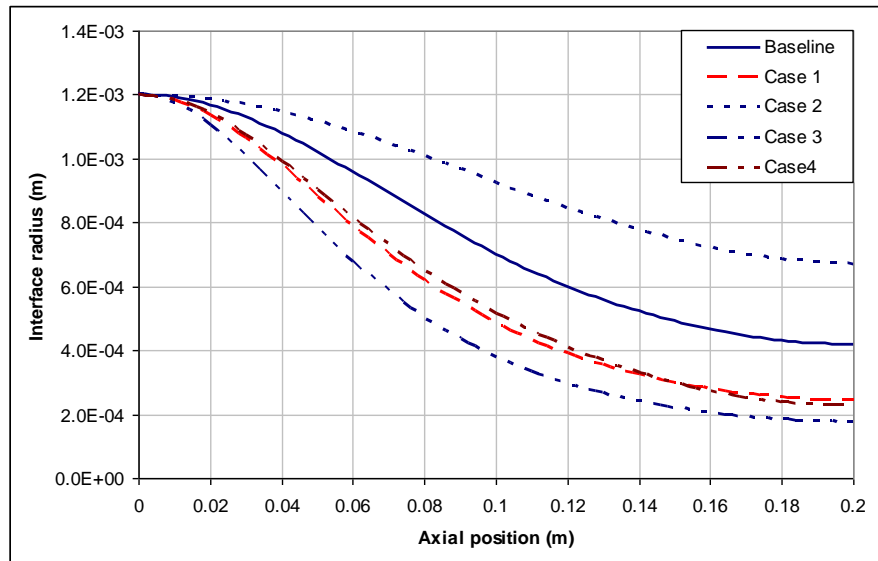


Figure 5.1: Liquid interface radius variation along heat pipe axis

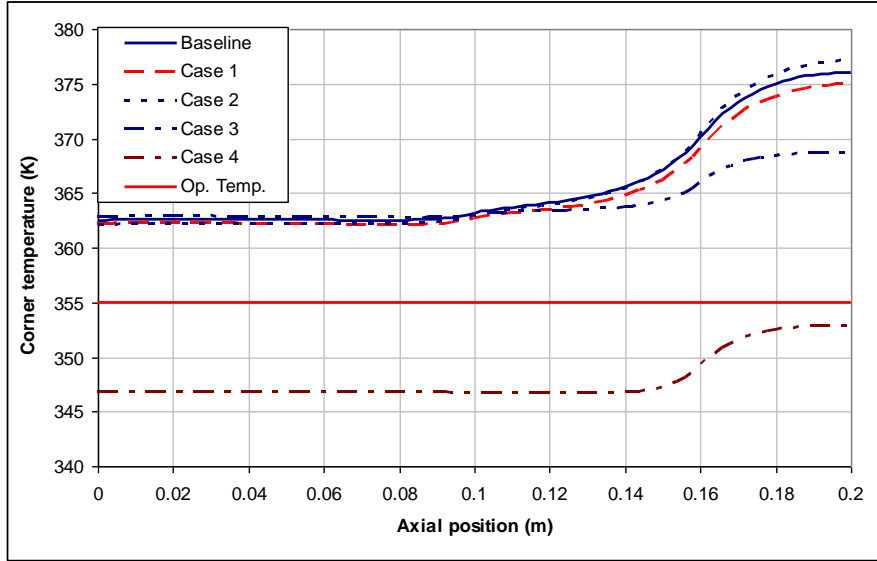


Figure 5.2: Edge temperature variation along heat pipe axis

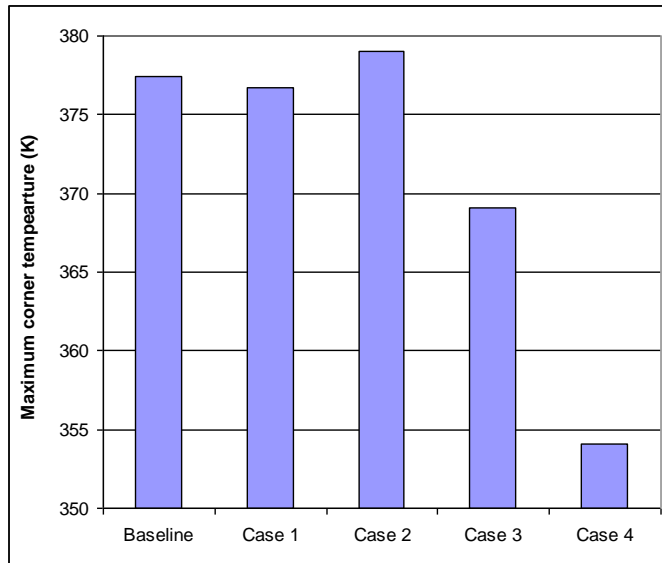


Figure 5.3: Maximum edge temperature for test cases

## CHAPTER 6

### CONCLUSION

Heat pipes take advantage of phase change to remove heat generated from a source. Therefore, they have large heat removal capacity compared to their size, which makes them preferable especially for electronics cooling applications. Studies performed on heat pipes with homogeneous wick structure used more detailed analysis both with in-house developed or commercially available codes. These studies involved two or three dimensional momentum analysis for liquid and/or vapor flow as well as heat transfer analysis in heat pipe container. In these studies evaporation/condensation mass flow rates were correlated by the heat flux at the liquid–vapor interface. However, studies on grooved heat pipes used simplifying assumptions to model liquid and/or vapor flow. Some studies included only axial heat in the analysis.

In the present study a flat micro heat pipe with rectangular cross section is investigated. Solution domain includes the heat pipe container material, solid domain, and working fluid, liquid domain. Previous studies showed that axial conduction affects evaporation and condensation regions in the heat pipe, but simplified approaches were used to model the heat transfer analysis. However, in the present study solid and liquid domains are modeled by three dimensional heat transfer equation. Phase change heat transfer from micro region is calculated using the relation obtained from kinetic theory. Moreover, phase change heat transfer from macro region is included into the analysis calculated from the heat balance at the liquid–vapor interface. It is shown that macro evaporation can account for up to 80% of the overall evaporation heat transfer. Conden-

sation from macro region is also calculated, however, it's effect on the overall condensation heat transfer is found to be at most 15%. Energy equation in the liquid domain includes both conduction and convection heat transfer, where the effect of convection is negligible similar to the findings of previous studies.

The results of the present study are validated using the results given in [6] in terms of liquid–vapor interface radius and heat pipe edge temperature variation along the heat pipe axis. The difference between two studies is found to be acceptable, where the difference is attributed to the three dimensional heat transfer analysis and phase change modeling at the liquid–vapor interface.

Due to the high thermal conductivity of the heat pipe container material, previous studies showed that a small fraction of the input heat load is transferred by conduction through the container. However, according to the present study it is found that %1–20 of the heat load is transferred by conduction inside the heat pipe container and the working fluid the magnitude of which is affected by the length of heat source and heat sink regions. The percentage can be increased by adding an adiabatic region at the outside boundary of the heat pipe between the heat source and sink regions or decreasing the thermal conductivity of the heat pipe material, which effectively reduces the contribution of the axial conduction.

In the current study the effects of physical dimensions of the heat pipe and boundary conditions are also investigated. In the first part of the study a definite amount of heat load is applied and it is not forced to reach dry-out limit, the variation of the liquid–vapor interface and heat pipe container temperature, which defines the operating range of the heat pipe is investigated. The results can be summarized as,

- Increasing heat load increases the vapor temperature and consequently higher heat pipe container temperature is obtained,
- Increasing ambient heat transfer coefficient decreases heat pipe container temperature,
- Decreasing heat pipe material thermal conductivity increases the ratio of the heat transfer by phase change and increases the heat pipe container

temperature ,

- Increasing the initial value of the liquid–vapor interface radius does not affect the container temperature and the ratio of the heat transfer by phase change, but the the interface radius change rate increases,
- Increasing groove depth decreases the ratio of the heat transfer by phase change but does not change the container temperature,
- Increasing fin thickness decreases the ratio of the heat transfer by phase change, but increases the container temperature,
- Increasing groove width decreases the ratio of the heat transfer by phase change, but increases the container temperature,
- Adding an adiabatic region or increasing it's length increase the ratio of the heat transfer by phase change.

In the second part of the study, the effect of the physical dimension of the heat pipe is investigated, where operation at the dry-out limit is forced by increasing the input heat load. In this study, the change in the maximum heat transfer capacity can be summarized as,

- For a fixed total length of fin thickness and groove width, increasing groove width increases maximum heat transfer capacity until it reaches a upper limit, where the capacity gets a constant value,
- For a constant fin thickness, increasing groove width increases the heat transfer capacity to a maximum, after which it starts to decrease,
- For a constant fin thickness and groove width, increasing groove depth increases heat capacity,
- Increasing heat pipe length decreases heat transfer capacity,
- Increasing the ratio of heat source and sink region lengths to the total length decreases heat capacity.

Present study can be also used for different groove geometries (e.g trapezoidal) and the effect of the geometry on the heat transfer capacity can be compared. The thermophysical properties of the working fluid is taken as constant values in this study, the variation of those properties with temperature can be introduced into the model, whose effect can be considerable where the vapor and the edge temperature have high values. Moreover, vapor domain and vapor core dimension can be included, which is not considered in the present model. The effect of the vapor core dimension on the flooding limit can be analyzed. Condensation modeling of the present study uses simplified modeling of the liquid film thickness, which can be improved by detailed analysis and the effect on the liquid–vapor interface can be studied. The current condensation modeling, which is also used in the previous studies, is not a mass conserving model, where the condensate fluid mass on the fin top increases along the heat pipe axis from the condensation region to the evaporation region. Moreover, the transition from the condensation to the evaporation region on the fin top is an abrupt change, where the fluid mass on the fin top at the last condensation region position is assumed to be evaporated completely at the first evaporation region position due to the phase change modeling. This condition can also affect the total fluid mass calculation, which considers both the liquid in the groove and on the fin top of the heat pipe geometry. By using more detailed condensation modeling the analysis can be improved to analyze physical phenomena through phase change region.

## REFERENCES

- [1] D. REAY P. KEW. *Theory, Design and Application*. Elsevier, 2006.
- [2] T.NGUYEN K.MASHIKO Y.SAITO V.WUTTIJUMNONG M.MOCHIZUKI. A review of heat pipe application including new opportunities. *Frontiers in Heat Pipes*, 2-013001:1–15, 2011.
- [3] B.R.BABIN G.P.PETERSON D.WU. Steady-state modeling and testing of a micro heat pipe. *Journal of Heat Transfer*, 112:595–601, 1990.
- [4] M.C.ZAGHDOUDI S.MAALEJ J.MANSOURI M.B.H.SASSI. Flat miniature heat pipes for electronics cooling: State of the art, experimental and theoretical analysis. *World Academy of Science, Engineering and Technology*, 75:880–903, 2011.
- [5] Y.WANG K.VAFAI. An experimental investigation of the thermal performance of an asymmetrical flat plate heat pipe. *International Journal of Heat and Mass Transfer*, 43:2657–2668, 2000.
- [6] F.LEFÈVRE R.RULLIÈRE G.PANDRAUD M.LALLEMAND. Prediction of the temperature field in flat plate heat pipes with micro-grooves – experimental validation. *International Journal of Heat and Mass Transfer*, 51:4083–4094, 2008.
- [7] A.FAGHRI. *Heat Pipe Science and Technology*. Taylor and Francis, 1995.
- [8] A.BEJAN A.KRAUS. *Heat Transfer Handbook*. John Wiley and Sons, 2003.
- [9] K.VAFAI W.WANG. Analysis of flow and heat transfer characteristics of an asymmetrical flat plate heat pipe. *International Journal of Heat and Mass Transfer*, 35:2087–2099, 1992.
- [10] N.ZHU K.VAFAI. Vapor and liquid flow in an asymmetrical flat plate heat pipe: A three-dimensional analytical and numerical investigation. *International Journal of Heat and Mass Transfer*, 41(1):159–174, 1998.
- [11] Y.WANG K.VAFAI. Transient characterization of flat plate heat pipes during startup and shutdown operations. *International Journal of Heat and Mass Transfer*, 43:2641–2655, 2000.

- [12] B.XIAO A.FAGHRI. A three-dimensional thermal-fluid analysis of flat heat pipes. *International Journal of Heat and Mass Transfer*, 51:3113–3126, 2008.
- [13] M.AGHVAMI A.FAGHRI. Analysis of flat heat pipes with various heating and cooling configurations. *Applied Thermal Engineering*, 3:2645–2655, 2011.
- [14] J.H.PARK H.NOH J.LEE. A numerical study on the heat pipe with switched heat source and sink for space application. *ASME Proceedings of 31st National Heat Transfer Conference*, 7:109–116, 1996.
- [15] F.LEFÈVRE M.LALLEMAND. Coupled thermal and hydrodynamic models of flat micro heat pipes for the cooling of multiple electronic components. *International Journal of Heat and Mass Transfer*, 49:1375–1383, 2006.
- [16] R.SONAN S.HARMAAND J.PELLÈ D.LEGER M.FAKÈS. Transient thermal and hydrodynamic model of flat heat pipe for the cooling of electronics components. *International Journal of Heat and Mass Transfer*, 51:6006–6017, 2008.
- [17] N.THUCHAYAPONG A.NAKANO P.SAKULCHANGSATJATAI P.TERDTON. Effect of capillary pressure on performance of a heat pipe: Numerical approach with fem. *Applied Thermal Engineering*, 32:93–99, 2012.
- [18] M.ELNAGGAR M.Z.ABDULLAH M.A.MUJEEBU. Characterization of working fluid in vertically mounted finned u-shape twin heat pipe for electronic cooling. *Energy Conversion and Management*, 62:31–39, 2012.
- [19] V.BIANCO K.VAFI O.MANCA M.SHAFI. Thermal performance of flat-shaped heat pipes using nanofluids. *International Journal of Heat and Mass Transfer*, 53:1438–1445, 2010.
- [20] G.P.PETERSON H.B.MA. Theoretical analysis of the maximum heat transport in triangular grooves: A study of idealized micro heat pipes. *Journal of Heat Transfer*, 118:731–739, 1996.
- [21] D.KHRUSTALEV A.FAGHRI. Thermal analysis of a micro heat pipe. *Journal of Heat Transfer*, 116:189–198, 1994.
- [22] M.R.KUMAR S.DASGUPTA. Modelling of evaporation from v-shaped microgrooves. *Chemical Engineer Community*, 160:225–248, 1997.
- [23] B.SUMAN S.DE S.DASGUPTA. A model of the capillary limit of a micro heat pipe and prediction of the dry-out length. *International Journal of Heat and Fluid Flow*, 26:495–505, 2005.

- [24] B.SUMAN N.HODA. Effect of variations in thermophysical properties and design parameters on the performance of a v-shaped micro grooved heat pipe. *International Journal of Heat and Mass Transfer*, 48:2090–2101, 2005.
- [25] B.SUMAN S.DE S.DASGUPTA. Transient modeling of micro-grooved heat pipe. *International Journal of Heat and Mass Transfer*, 48:1633–1646, 2005.
- [26] S.ANAND S.DE S.DASGUPTA. Experimental and theoretical study of axial dryout point for evaporation from v-shaped microgrooves. *International Journal of Heat and Mass Transfer*, 45:1535–1543, 2002.
- [27] S.K.THOMAS R.C.LYKINS K.L.YERKES. Fully developed laminar flow in trapezoidal grooves with shear stress at the liquid-vapor interface. *International Journal of Heat and Mass Transfer*, 44:3397–3412, 2001.
- [28] S.LAUNAY V.SARTRE M.LALLEMAND. Hydrodynamic and thermal study of a water-filled micro-heat-pipe array. *Journal of Thermophysics and Heat Transfer*, 18(3):358–363, 2004.
- [29] Y.M.HUNG K.TIO. Thermal analysis of optimally designed inclined micro heat pipes with axial solid wall conduction. *International Communications in Heat and Mass Transfer*, 39:1146–1153, 2012.
- [30] F.L.CHANG Y.M.HUNG. The coupled effects of working fluid and solid wall on thermal performance of micro heat pipes. *International Communications in Heat and Mass Transfer*, 73:76–87, 2014.
- [31] J.QU H.WU P.CHENG. Effects of functional surface on performance of a micro heat pipe. *International Communications in Heat and Mass Transfer*, 35:523–528, 2008.
- [32] Y.CHEN C.ZHANG M.SHI J.WUA G.P.PETERSON. Study on flow and heat transfer characteristics of heat pipe with axial omega-shaped micro grooves. *International Journal of Heat and Mass Transfer*, 52:636–643, 2009.
- [33] A.R. ANAND A.J. VEDAMURTHY S.R. CHIKKALA S. KUMAR D. KUMAR P. GUPTA. Analytical and experimental investigations on axially grooved aluminum-ethane heat pipe. *Heat Transfer Engineering*, 29(4):410–416, 2008.
- [34] S.J.KIM J.K.SEO K.H.DO. Analytical and experimental investigation on the operational characteristics and the thermal optimization of a miniature heat pipe with a grooved wick structure. *International Journal of Heat and Mass Transfer*, 46:2051–2063, 2003.
- [35] B.SUMAN. A steady state model and maximum heat transport capacity of an electrohydrodynamically augmented micro-grooved heat pipe. *International Journal of Heat and Mass Transfer*, 4:3957–3967, 2006.

- [36] Y.M.HUNG Q.SENG. Effects of geometric design on thermal performance of star-groove micro-heat pipes. *International Journal of Heat and Mass Transfer*, 54:1198–1209, 2011.
- [37] N.CHAURIS V.AYEL Y.BERTIN C.ROMESTANT D.EYSSERIC. Hydraulic modelling of a flat heat pipe with two different groove shapes and a small vapour section. *Applied Thermal Engineering*, 61:311– 326, 2013.
- [38] K.H.DO S.J.KIM S.V.GARIMELLA. A mathematical model for analyzing the thermal characteristics of a flat micro heat pipe with a grooved wick. *International Journal of Heat and Mass Transfer*, 51:4637–4650, 2008.
- [39] C.GILLOT Y.AVENAS N.CEZAC G.POUPON C.SCHAEFFER E.FOURNIER. Silicon heat pipes used as thermal spreaders. , *IEEE Transactions on Components and Packaging Technologies*, 26(2):332–339, 2003.
- [40] L.LIN R.PONNAPPAN J.LELAND. High performance miniature heat pipe. *International Journal of Heat and Mass Transfer*, 45:3131–3142, 2002.
- [41] R.RULLIÈRE F.LEFÈVRE M.LALLEMAND. Prediction of the maximum heat transfer capability of two-phase heat spreaders—experimental validation. *International Journal of Heat and Mass Transfer*, 50:1255–1262, 2007.
- [42] S.LIPS F.LEFÈVRE J.BONJOUR. Combined effects of the filling ratio and the vapour space thickness on the performance of a flat plate heat pipe. *International Journal of Heat and Mass Transfer*, 53:694–702, 2010.
- [43] S.LIPS F.LEFÈVRE J.BONJOUR. Physical mechanisms involved in grooved flat heat pipes: Experimental and numerical analyses. *International Journal of Thermal Sciences*, 50:1243–1252, 2011.
- [44] C.GILLOT A.LAR M.IVANOVA Y.AVENAS C.SCHAEFFER E.FOURNIER. Experimental study of a flat silicon heat pipe with microcapillary grooves. *Inter Society Conference on Thermal Phenomena*, page 47–50, 2004.
- [45] Y.WANG G.P.PETERSON. Investigation of a novel flat heat pipe. *Journal of Heat Transfer*, 127:165–170, 2005.
- [46] K.H.DO S.P.JANG. Effect of nanofluids on the thermal performance of a flat micro heat pipe with a rectangular grooved wick. *International Journal of Heat and Mass Transfer*, 53:2183–2192, 2010.
- [47] P.C.STEPHAN C.A.BUSSE. Analysis of the heat transfer coefficient of grooved heat pipe evaporator walls. *International Journal of Heat and Mass Transfer*, 35(2):383–391, 1992.

- [48] S.DU Y.H.ZHAO. New boundary conditions for the evaporating thin-film model in a rectangular micro channel. *International Journal of Heat and Mass Transfer*, 54:3694–3701, 2011.
- [49] R.BERTOSSI V.AYEL C.ROMESTANT Y.BERTIN Z.LATAOUI. Modeling of transfer in the microregion in axially grooved heat pipes: Comparison of fluid performances. *Heat Pipe Science and Technology, An International Journal*, 1(1):99–112, 2010.
- [50] A.J.JIAO H.B.MA J.K.CRITSER. Evaporation heat transfer characteristics of a grooved heat pipe with micro-trapezoidal grooves. *International Journal of Heat and Mass Transfer*, 50:2905–2911, 2007.
- [51] P.CHENG J.DONG S.M.THOMPSON H.B.MA. Heat transfer in bulk and thin-film fluid regions of rectangular microgroove. *Journal of Thermophysics and Heat Transfer*, 26(1):108–114, 2012.
- [52] Y.ZHANG A.FAGHRI. Numerical simulation of condensation on a capillary grooved structure. *Numerical Heat Transfer, Part A*, page 227–243, 2001.
- [53] R.H.NILSON S.W.TCHIKANDA S.K.GRIFFITHS M.J.MARTINEZ. Steady evaporating flow in rectangular microchannel. *International Journal of Heat and Mass Transfer*, 49:1603–1618, 2006.



## APPENDIX A

### DERIVATION OF ENERGY EQUATION IN THE TRANSFORMED DOMAIN

$$u \frac{\partial T}{\partial y} + w \frac{\partial T}{\partial z} = \frac{k_l}{\rho C p_l} \left( \frac{\partial^2 T}{\partial x^2} + \frac{\partial^2 T}{\partial y^2} + \frac{\partial^2 T}{\partial z^2} \right) + \frac{\mu}{\rho_l C p_l} \Phi \quad (\text{A.1})$$

The derivatives are written using chain rule.

$$\frac{\partial T}{\partial y} = \frac{\partial T}{\partial \lambda} \frac{\partial \lambda}{\partial y} + \frac{\partial T}{\partial \eta} \frac{\partial \eta}{\partial y} + \frac{\partial T}{\partial \xi} \frac{\partial \xi}{\partial y} \quad (\text{A.2})$$

$$\begin{aligned} \frac{\partial^2 T}{\partial x^2} &= \frac{\partial^2 T}{\partial \lambda^2} \left( \frac{\partial \lambda}{\partial x} \right)^2 + \frac{\partial^2 T}{\partial \eta^2} \left( \frac{\partial \eta}{\partial x} \right)^2 + \frac{\partial^2 T}{\partial \xi^2} \left( \frac{\partial \xi}{\partial x} \right)^2 + \\ &\quad \frac{\partial^2 T}{\partial \lambda \partial \eta} \left( 2 \frac{\partial \lambda}{\partial x} \frac{\partial \eta}{\partial x} \right) + \frac{\partial^2 T}{\partial \lambda \partial \xi} \left( 2 \frac{\partial \lambda}{\partial x} \frac{\partial \xi}{\partial x} \right) + \frac{\partial^2 T}{\partial \eta \partial \xi} \left( 2 \frac{\partial \eta}{\partial x} \frac{\partial \xi}{\partial x} \right) + \\ &\quad \frac{\partial T}{\partial \lambda} \left( \frac{\partial^2 \lambda}{\partial x^2} \right) + \frac{\partial T}{\partial \eta} \left( \frac{\partial^2 \eta}{\partial x^2} \right) + \frac{\partial T}{\partial \xi} \left( \frac{\partial^2 \xi}{\partial x^2} \right) \end{aligned} \quad (\text{A.3})$$

$$\begin{aligned} \frac{\partial^2 T}{\partial y^2} &= \frac{\partial^2 T}{\partial \lambda^2} \left( \frac{\partial \lambda}{\partial y} \right)^2 + \frac{\partial^2 T}{\partial \eta^2} \left( \frac{\partial \eta}{\partial y} \right)^2 + \frac{\partial^2 T}{\partial \xi^2} \left( \frac{\partial \xi}{\partial y} \right)^2 + \\ &\quad \frac{\partial^2 T}{\partial \lambda \partial \eta} \left( 2 \frac{\partial \lambda}{\partial y} \frac{\partial \eta}{\partial y} \right) + \frac{\partial^2 T}{\partial \lambda \partial \xi} \left( 2 \frac{\partial \lambda}{\partial y} \frac{\partial \xi}{\partial y} \right) + \frac{\partial^2 T}{\partial \eta \partial \xi} \left( 2 \frac{\partial \eta}{\partial y} \frac{\partial \xi}{\partial y} \right) + \\ &\quad \frac{\partial T}{\partial \lambda} \left( \frac{\partial^2 \lambda}{\partial y^2} \right) + \frac{\partial T}{\partial \eta} \left( \frac{\partial^2 \eta}{\partial y^2} \right) + \frac{\partial T}{\partial \xi} \left( \frac{\partial^2 \xi}{\partial y^2} \right) \end{aligned} \quad (\text{A.4})$$

$$\begin{aligned}
\frac{\partial^2 T}{\partial z^2} &= \frac{\partial^2 T}{\partial \lambda^2} \left( \frac{\partial \lambda}{\partial z} \right)^2 + \frac{\partial^2 T}{\partial \eta^2} \left( \frac{\partial \eta}{\partial z} \right)^2 + \frac{\partial^2 T}{\partial \xi^2} \left( \frac{\partial \xi}{\partial z} \right)^2 + \\
&\frac{\partial^2 T}{\partial \lambda \partial \eta} \left( 2 \frac{\partial \lambda}{\partial z} \frac{\partial \eta}{\partial z} \right) + \frac{\partial^2 T}{\partial \lambda \partial \xi} \left( 2 \frac{\partial \lambda}{\partial y} \frac{\partial \xi}{\partial z} \right) + \frac{\partial^2 T}{\partial \eta \partial \xi} \left( 2 \frac{\partial \eta}{\partial z} \frac{\partial \xi}{\partial z} \right) + \\
&\frac{\partial T}{\partial \lambda} \left( \frac{\partial^2 \lambda}{\partial z^2} \right) + \frac{\partial T}{\partial \eta} \left( \frac{\partial^2 \eta}{\partial z^2} \right) + \frac{\partial T}{\partial \xi} \left( \frac{\partial^2 \xi}{\partial z^2} \right)
\end{aligned} \tag{A.5}$$

The transformed coordinates are defined as follows

$$\lambda = x ; \quad \eta = y ; \quad \xi = z_0 + \frac{z}{\Delta h_i} \Delta h_0 \tag{A.6}$$

Therefore the following derivatives can be obtained directly.

$$\frac{\partial \lambda}{\partial x} = 1 ; \quad \frac{\partial \lambda}{\partial y} = 0 ; \quad \frac{\partial \lambda}{\partial z} = 0 ; \tag{A.7}$$

$$\frac{\partial \eta}{\partial x} = 0 ; \quad \frac{\partial \eta}{\partial y} = 1 ; \quad \frac{\partial \eta}{\partial z} = 0 . \tag{A.8}$$

Total derivative of each variable can be expressed in terms of and

$$dx = \frac{\partial x}{\partial \lambda} d\lambda + \frac{\partial x}{\partial \eta} d\eta + \frac{\partial x}{\partial \xi} d\xi ; \tag{A.9}$$

$$dy = \frac{\partial y}{\partial \lambda} d\lambda + \frac{\partial y}{\partial \eta} d\eta + \frac{\partial y}{\partial \xi} d\xi ; \tag{A.10}$$

$$dz = \frac{\partial z}{\partial \lambda} d\lambda + \frac{\partial z}{\partial \eta} d\eta + \frac{\partial z}{\partial \xi} d\xi . \tag{A.11}$$

Equations A.11-13 are rearranged to give,

$$d\lambda = \frac{1}{\det \mathbf{J}} [a_1 dx + a_2 dy + a_3 dz] \tag{A.12}$$

$$d\eta = \frac{1}{\det \mathbf{J}} [b_1 dx + b_2 dy + b_3 dz] \quad (\text{A.13})$$

$$d\xi = \frac{1}{\det \mathbf{J}} [c_1 dx + c_2 dy + c_3 dz] \quad (\text{A.14})$$

where the coefficients are,

$$\begin{aligned} a_1 &= \frac{\partial y}{\partial \eta} \frac{\partial z}{\partial \xi} - \frac{\partial y}{\partial \xi} \frac{\partial z}{\partial \eta} & a_2 &= \frac{\partial x}{\partial \xi} \frac{\partial z}{\partial \eta} - \frac{\partial x}{\partial \eta} \frac{\partial z}{\partial \xi} & a_3 &= \frac{\partial x}{\partial \eta} \frac{\partial y}{\partial \xi} - \frac{\partial x}{\partial \xi} \frac{\partial y}{\partial \eta} \\ b_1 &= \frac{\partial y}{\partial \xi} \frac{\partial z}{\partial \lambda} - \frac{\partial y}{\partial \lambda} \frac{\partial z}{\partial \xi} & b_2 &= \frac{\partial x}{\partial \lambda} \frac{\partial z}{\partial \xi} - \frac{\partial x}{\partial \xi} \frac{\partial z}{\partial \lambda} & b_3 &= \frac{\partial x}{\partial \xi} \frac{\partial y}{\partial \lambda} - \frac{\partial x}{\partial \lambda} \frac{\partial y}{\partial \xi} \\ c_1 &= \frac{\partial y}{\partial \lambda} \frac{\partial z}{\partial \eta} - \frac{\partial y}{\partial \eta} \frac{\partial z}{\partial \lambda} & c_2 &= \frac{\partial x}{\partial \eta} \frac{\partial z}{\partial \lambda} - \frac{\partial x}{\partial \lambda} \frac{\partial z}{\partial \eta} & c_3 &= \frac{\partial x}{\partial \lambda} \frac{\partial y}{\partial \eta} - \frac{\partial x}{\partial \eta} \frac{\partial y}{\partial \lambda} \end{aligned}$$

where  $\mathbf{J}$  is the determinant of the Jacobian matrix and is defined as,

$$\det \mathbf{J} = d_1 \frac{\partial x}{\partial \lambda} - d_2 \frac{\partial x}{\partial \eta} + d_3 \frac{\partial x}{\partial \xi} \quad (\text{A.15})$$

where

$$d_1 = \frac{\partial y}{\partial \eta} \frac{\partial z}{\partial \xi} - \frac{\partial z}{\partial \eta} \frac{\partial y}{\partial \xi} \quad d_2 = \frac{\partial y}{\partial \lambda} \frac{\partial z}{\partial \xi} - \frac{\partial z}{\partial \lambda} \frac{\partial y}{\partial \xi} \quad d_3 = \frac{\partial y}{\partial \lambda} \frac{\partial z}{\partial \eta} - \frac{\partial z}{\partial \lambda} \frac{\partial y}{\partial \eta}$$

The Jacobian matrix is defined by,

$$\begin{vmatrix} \frac{\partial \lambda}{\partial x} & \frac{\partial \lambda}{\partial y} & \frac{\partial \lambda}{\partial z} \\ \frac{\partial \eta}{\partial x} & \frac{\partial \eta}{\partial y} & \frac{\partial \eta}{\partial z} \\ \frac{\partial \xi}{\partial x} & \frac{\partial \xi}{\partial y} & \frac{\partial \xi}{\partial z} \end{vmatrix} \quad (\text{A.16})$$

Using Equations A.9 and A.10 and A.18 following relations are derived.

$$\frac{\partial x}{\partial \lambda} = 1 ; \quad \frac{\partial y}{\partial \lambda} = 0 ; \quad \frac{\partial z}{\partial \lambda} = 0 ; \quad (\text{A.17})$$

$$\frac{\partial x}{\partial \eta} = 0 ; \quad \frac{\partial y}{\partial \eta} = 1 ; \quad \frac{\partial z}{\partial \eta} = 0. \quad (\text{A.18})$$

Coordinate derivatives becomes

$$\frac{\partial \lambda}{\partial x} = 1 ; \quad \frac{\partial \lambda}{\partial y} = 0 ; \quad \frac{\partial \lambda}{\partial z} = 0 ; \quad (\text{A.19})$$

$$\frac{\partial \eta}{\partial x} = 0 ; \quad \frac{\partial \eta}{\partial y} = 1 ; \quad \frac{\partial \eta}{\partial z} = 0 ; \quad (\text{A.20})$$

$$\frac{\partial \xi}{\partial x} = -\frac{\partial z}{\partial \lambda} / \frac{\partial z}{\partial \xi} ; \quad \frac{\partial \xi}{\partial y} = -\frac{\partial z}{\partial \eta} / \frac{\partial z}{\partial \xi} ; \quad \frac{\partial \xi}{\partial z} = 1 / \frac{\partial z}{\partial \xi} \quad (\text{A.21})$$

$$\frac{\partial^2 \lambda}{\partial x^2} = 0 ; \quad \frac{\partial^2 \lambda}{\partial y^2} = 0 ; \quad \frac{\partial^2 \lambda}{\partial z^2} = 0 ; \quad (\text{A.22})$$

$$\frac{\partial^2 \eta}{\partial x^2} = 0 ; \quad \frac{\partial^2 \eta}{\partial y^2} = 0 ; \quad \frac{\partial^2 \eta}{\partial z^2} = 0 . \quad (\text{A.23})$$

$$\begin{aligned} \frac{\partial^2 \xi}{\partial x^2} &= e_1 \left( \frac{\partial z}{\partial \xi} \right)^{-1} + e_2 \left( \frac{\partial z}{\partial \xi} \right)^{-2} + e_3 \left( \frac{\partial z}{\partial \xi} \right)^{-3} \\ \frac{\partial^2 \xi}{\partial y^2} &= f_1 \left( \frac{\partial z}{\partial \xi} \right)^{-1} + f_2 \left( \frac{\partial z}{\partial \xi} \right)^{-2} + f_3 \left( \frac{\partial z}{\partial \xi} \right)^{-3} \\ \frac{\partial^2 \xi}{\partial z^2} &= g_1 \left( \frac{\partial z}{\partial \xi} \right)^{-3} \end{aligned} \quad (\text{A.24})$$

where

$$\begin{aligned}
e_1 &= -\frac{\partial^2 z}{\partial \lambda^2}; & e_2 &= 2\frac{\partial z}{\partial \lambda} \frac{\partial^2 \lambda}{\partial \xi \partial z}; & e_3 &= -\frac{\partial^2 z}{\partial \xi^2} \left(\frac{\partial z}{\partial \lambda}\right)^2; \\
f_1 &= -\frac{\partial^2 z}{\partial \eta^2}; & f_2 &= 2\frac{\partial z}{\partial \eta} \frac{\partial^2 \eta}{\partial \xi \partial z}; & f_3 &= -\frac{\partial^2 z}{\partial \xi^2} \left(\frac{\partial z}{\partial \eta}\right)^2; \\
g_1 &= \frac{\partial^2 z}{\partial \xi^2}.
\end{aligned}$$

Final form of Equation A.1 becomes

$$\begin{aligned}
u \left( \frac{\partial T}{\partial \eta} + h_0 \frac{\partial T}{\partial \xi} \right) + w \left( h_1 \frac{\partial T}{\partial \xi} \right) &= \frac{k_l}{\rho C_{pl}} \left( \frac{\partial^2 T}{\partial \lambda^2} + \frac{\partial^2 T}{\partial \eta^2} + h_2 \frac{\partial^2 T}{\partial \xi^2} \right) + \\
&\frac{k_l}{\rho C_{pl}} \left( h_3 \frac{\partial^2 T}{\partial \lambda \partial \xi} + h_4 \frac{\partial^2 T}{\partial \eta \partial \xi} + h_5 \frac{\partial T}{\partial \xi} \right) + \\
&\frac{\mu}{\rho l C_{pl}} \Phi
\end{aligned} \tag{A.25}$$

where the coefficients are defined as,

$$\begin{aligned}
h_0 &= \frac{\partial \xi}{\partial y} \\
h_1 &= \frac{\partial \xi}{\partial z} \\
h_2 &= \left( \frac{\partial \xi}{\partial x} \right)^2 + \left( \frac{\partial \xi}{\partial y} \right)^2 + \left( \frac{\partial \xi}{\partial z} \right)^2 \\
h_3 &= 2 \frac{\partial \xi}{\partial x} \\
h_4 &= 2 \frac{\partial \xi}{\partial y} \\
h_5 &= \frac{\partial^2 \xi}{\partial x^2} + \frac{\partial^2 \xi}{\partial y^2} + \frac{\partial^2 \xi}{\partial z^2}
\end{aligned}$$



## APPENDIX B

### ENERGY BALANCE EQUATIONS AT THE INTERFACES

For the interface grid points between solid and liquid domain, finite difference form of the energy balance equations are given for the four subregions. The indices  $i, j$  and  $k$  represent the grid node points in  $x, y$  and  $z$ -directions in the solid domain and  $\lambda, \eta$  and  $\xi$ -directions in the transformed liquid domain. The representative figures are given to show the heat flux definitions, where only heat balance in  $x - z$  plane is shown.

Heat flow rates in solid domain are defined as,

$$q''_{x_s} A_x = k_s A_x \frac{\partial T}{\partial x} \quad (\text{B.1})$$

$$q''_{y_s} A_y = k_s A_y \frac{\partial T}{\partial y} \quad (\text{B.2})$$

$$q''_{z_s} A_z = k_s A_z \frac{\partial T}{\partial z} \quad (\text{B.3})$$

Heat flow rates in liquid domain are defined in transformed coordinates. The cross-sectional area  $A_x$  is in  $y-z$  plane,  $A_y$  in  $x-z$  plane, which are approximated as trapezoidal areas and calculated for each grid point using the solution domain grid points.  $A_z$  is the projected area on  $x - y$  plane.

$$q''_{x_l} A_x = k_l A_x \left( \frac{\partial T}{\partial \lambda} + \frac{\partial T}{\partial \xi} \frac{\partial \xi}{\partial x} \right) \quad (\text{B.4})$$

$$q''_{y_l} A_y = k_l A_y \left( \frac{\partial T}{\partial \eta} + \frac{\partial T}{\partial \xi} \frac{\partial \xi}{\partial y} \right) \quad (\text{B.5})$$

$$q''_{z_l} A_z = k_l A_z \left( \frac{\partial T}{\partial \xi} \frac{\partial \xi}{\partial z} \right) \quad (\text{B.6})$$

For the general case for a liquid control volume, the upper and lower surfaces are curved and the surface normal has components in  $x$  and  $y$ -coordinates. The areas  $A_{nt_x}$  and  $A_{nt_y}$  represent projected areas of the upper curved surface on  $y - z$  plane and  $x - z$  plane respectively, which are also approximated as trapezoidal areas and calculated using grid points.  $A_{nb_x}$  and  $A_{nb_y}$  are projected areas of the lower curved surface.

$$q''_{nt_x} A_{nt_x} = k_l A_{nt_x} \left( \frac{\partial T}{\partial \lambda} + \frac{\partial T}{\partial \xi} \frac{\partial \xi}{\partial x} \right) \quad (\text{B.7})$$

$$q''_{nt_y} A_{nt_y} = k_l A_{nt_y} \left( \frac{\partial T}{\partial \eta} + \frac{\partial T}{\partial \xi} \frac{\partial \xi}{\partial y} \right) \quad (\text{B.8})$$

$$q''_{nb_x} A_{nb_x} = k_l A_{nb_x} \left( \frac{\partial T}{\partial \lambda} + \frac{\partial T}{\partial \xi} \frac{\partial \xi}{\partial x} \right) \quad (\text{B.9})$$

$$q''_{nb_y} A_{nb_y} = k_l A_{nb_y} \left( \frac{\partial T}{\partial \eta} + \frac{\partial T}{\partial \xi} \frac{\partial \xi}{\partial y} \right) \quad (\text{B.10})$$

## B.1 Energy Balance for Region I

Region I is defined at the interface along the bottom of the groove. The heat fluxes on each surface is shown in Figure B.1

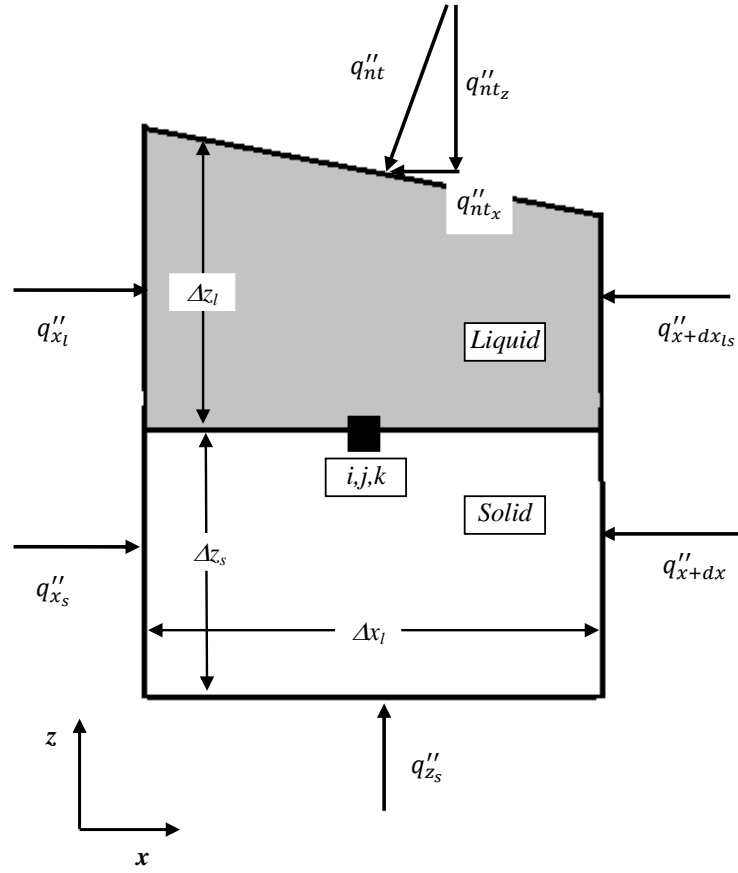


Figure B.1: Energy balance for Region I

For this region  $\dot{Q}_{nb_x}$  and  $\dot{Q}_{nb_y}$  are not defined, since this part of the control volume is solid. Finite difference forms of Equations B.1–3 and B.4–8 become,

$$\dot{Q}_{i-\frac{1}{2},j,k} = k_s \frac{\Delta z_s}{2} \Delta y \frac{T_{i-1,j,k} - T_{i,j,k}}{\Delta x_l} \quad (\text{B.11})$$

$$\dot{Q}_{i+\frac{1}{2},j,k} = k_s \frac{\Delta z_s}{2} \Delta y \frac{T_{i+1,j,k} - T_{i,j,k}}{\Delta x_l} \quad (\text{B.12})$$

$$\dot{Q}_{i,j-\frac{1}{2},k} = k_s \frac{\Delta z_s}{2} \Delta x_l \frac{T_{i,j-1,k} - T_{i,j,k}}{\Delta y} \quad (\text{B.13})$$

$$\dot{Q}_{i,j+\frac{1}{2},k} = k_s \frac{\Delta z_s}{2} \Delta x_l \frac{T_{i,j+1,k} - T_{i,j,k}}{\Delta y} \quad (\text{B.14})$$

$$\dot{Q}_{i,j,k-\frac{1}{2}} = k_s \Delta x_l \Delta y \frac{T_{i,j,k-1} - T_{i,j,k}}{\Delta z_s} \quad (\text{B.15})$$

For Region I the coordinate derivatives  $\partial\xi/\partial x$  and  $\partial\xi/\partial y$  are zero due to the solid domain interface. As opposed to solid domain the areas  $A_x$ ,  $A_y$  are changing along the coordinate axes, therefore they are defined by indices  $i$  and  $j$ . Same notation is used also for  $A_{nt_x}$  and  $A_{nt_y}$ . Finite difference forms of the Equations B.4–6 become,

$$\dot{Q}_{i-\frac{1}{2},j,k} = k_l A_{x_{i-\frac{1}{2}}} \frac{\partial T}{\partial \lambda} = k_l A_{x_{i-\frac{1}{2}}} \frac{T_{i-1,j,k} - T_{i,j,k}}{\Delta \lambda} \quad (\text{B.16})$$

$$\dot{Q}_{i+\frac{1}{2},j,k} = k_l A_{x_{i+\frac{1}{2}}} \frac{\partial T}{\partial \lambda} = k_l A_{x_{i+\frac{1}{2}}} \frac{T_{i+1,j,k} - T_{i,j,k}}{\Delta \lambda} \quad (\text{B.17})$$

$$\dot{Q}_{i,j-\frac{1}{2},k} = k_l A_{y_{j-\frac{1}{2}}} \frac{\partial T}{\partial \eta} = k_l A_{y_{j-\frac{1}{2}}} \frac{T_{i,j-1,k} - T_{i,j,k}}{\Delta \eta} \quad (\text{B.18})$$

$$\dot{Q}_{i,j+\frac{1}{2},k} = k_l A_{y_{j+\frac{1}{2}}} \frac{\partial T}{\partial \eta} = k_l A_{y_{j+\frac{1}{2}}} \frac{T_{i,j+1,k} - T_{i,j,k}}{\Delta \eta} \quad (\text{B.19})$$

$$\dot{Q}_{i,j,k+\frac{1}{2}} = k_l A_z \frac{\partial T}{\partial \xi} \frac{\partial \xi}{\partial z} = k_l A_z \frac{T_{i,j,k+1} - T_{i,j,k}}{\Delta \xi} \left( \frac{\partial \xi}{\partial z} \right)_{i,j,k+\frac{1}{2}} \quad (\text{B.20})$$

Heat flow rates on the upper curved surface is defined by

$$\dot{Q}_{nt_x} = k_l A_{nt_x} \left[ \left( \frac{\partial T}{\partial \lambda} \right)_{i,j,k+\frac{1}{2}} + \left( \frac{\partial T}{\partial \xi} \frac{\partial \xi}{\partial x} \right)_{i,j,k+\frac{1}{2}} \right] \quad (\text{B.21})$$

$$\dot{Q}_{nt_y} = k_l A_{nt_y} \left[ \left( \frac{\partial T}{\partial \eta} \right)_{i,j,k+\frac{1}{2}} + \left( \frac{\partial T}{\partial \xi} \frac{\partial \xi}{\partial y} \right)_{i,j,k+\frac{1}{2}} \right] \quad (\text{B.22})$$

where

$$\left(\frac{\partial T}{\partial \lambda}\right)_{i,j,k+\frac{1}{2}} = \frac{1}{2} \left[ \frac{T_{i+1,j,k} - T_{i-1,j,k}}{2\Delta\lambda} + \frac{T_{i+1,j,k+1} - T_{i-1,j,k+1}}{2\Delta\lambda} \right] \quad (\text{B.23})$$

$$\left(\frac{\partial T}{\partial \xi} \frac{\partial \xi}{\partial x}\right)_{i,j,k+\frac{1}{2}} = \frac{T_{i,j,k+1} - T_{i,j,k}}{\Delta\xi} \frac{1}{2} \left[ \left(\frac{\partial \xi}{\partial x}\right)_{i,j,k} + \left(\frac{\partial \xi}{\partial x}\right)_{i,j,k+1} \right] \quad (\text{B.24})$$

$$\left(\frac{\partial T}{\partial \eta}\right)_{i,j,k+\frac{1}{2}} = \frac{1}{2} \left[ \frac{T_{i,j+1,k} - T_{i,j-1,k}}{2\Delta\eta} + \frac{T_{i,j+1,k+1} - T_{i,j-1,k+1}}{2\Delta\eta} \right] \quad (\text{B.25})$$

$$\left(\frac{\partial T}{\partial \xi} \frac{\partial \xi}{\partial y}\right)_{i,j,k+\frac{1}{2}} = \frac{T_{i,j,k+1} - T_{i,j,k}}{\Delta\xi} \frac{1}{2} \left[ \left(\frac{\partial \xi}{\partial y}\right)_{i,j,k} + \left(\frac{\partial \xi}{\partial y}\right)_{i,j,k+1} \right] \quad (\text{B.26})$$

The convective terms are obtained from net enthalpy flow into the control volume given in Figure B.2.

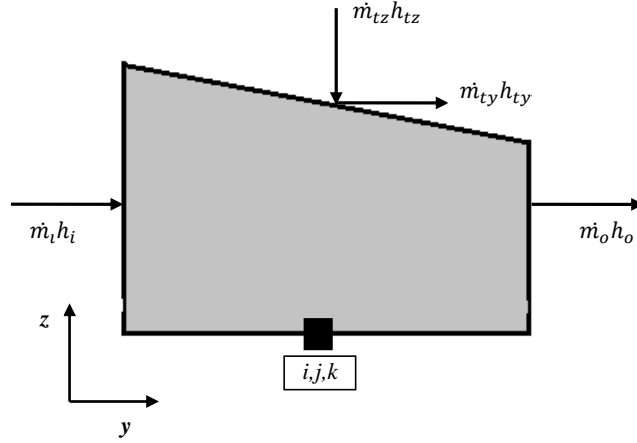


Figure B.2: Enthalpy flow to Region I

$$\dot{m}_i h_i - \dot{m}_o h_o - \dot{m}_{ty} h_{ty} + \dot{m}_{tz} h_{tz} = 0 \quad (\text{B.27})$$

Enthalpy is defined assuming constant  $C_{pl}$  as  $h = C_{pl} (T - T_{ref})$  and mass flow rates and temperature values are calculated as below.

$$\dot{m}_i = \frac{1}{2} (u_{j-1} + u_j) \rho_l A_{y_{j-\frac{1}{2}}}$$

$$T_i = \frac{1}{2} (T_{i,j,k} + T_{i,j-1,k})$$

$$\dot{m}_o = \frac{1}{2} (u_{j+1} + u_j) \rho_l A_{y_{j+\frac{1}{2}}}$$

$$T_o = \frac{1}{2} (T_{i,j,k} + T_{i,j+1,k})$$

$$\dot{m}_{ty} = u_j \rho_l A_{nt_y}$$

$$T_{ty} = \frac{1}{2} (T_{i,j,k} + T_{i,j,k+1})$$

$$\dot{m}_{tz} = -\dot{m}_i + \dot{m}_o + \dot{m}_{ty}$$

$$T_{tz} = \frac{1}{2} (T_{i,j,k} + T_{i,j,k+1})$$

## B.2 Energy Balance for Region II

Region II is located at the bottom groove corner as shown in Figure B.3. One fourth of the control volume is in the liquid domain and the rest is in the solid domain. The difference for this region comes from the area definition with respect to Region I.

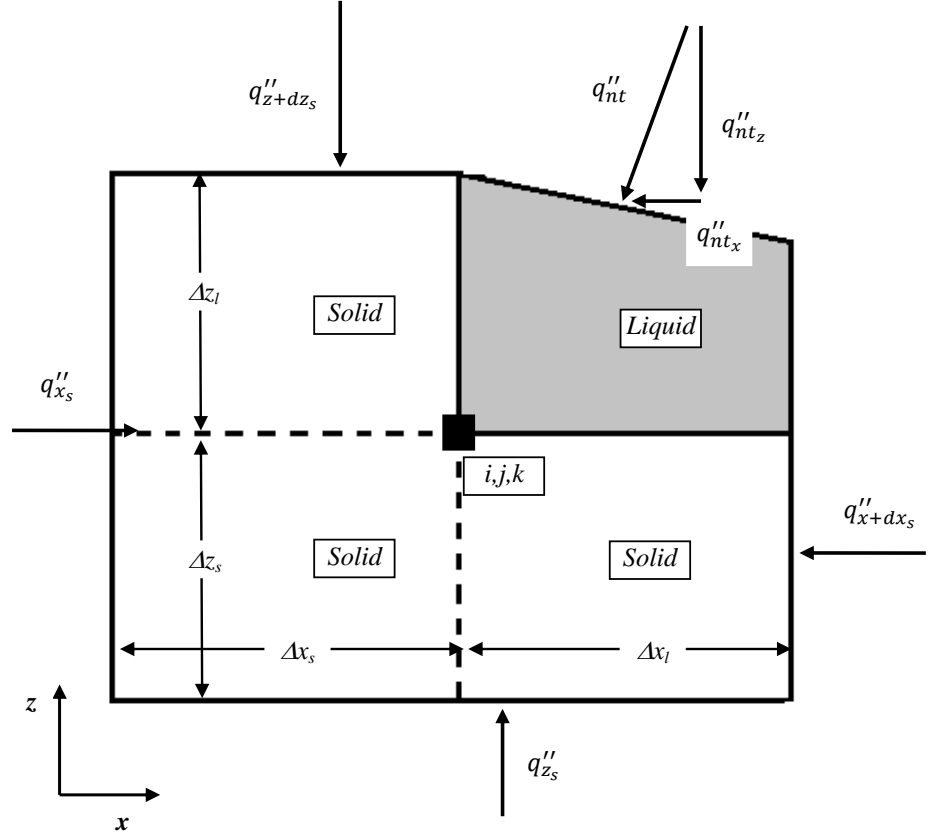


Figure B.3: Heat balance for Region II

$$\dot{Q}_{i-\frac{1}{2},j,k} = k_s \frac{\Delta z_s + \Delta z_l}{2} \Delta y \frac{T_{i-1,j,k} - T_{i,j,k}}{\Delta x_l} \quad (\text{B.28})$$

$$\dot{Q}_{i+\frac{1}{2},j,k} = k_s \frac{\Delta z_s}{2} \Delta y \frac{T_{i+1,j,k} - T_{i,j,k}}{\Delta x_l} \quad (\text{B.29})$$

$$\dot{Q}_{i,j-\frac{1}{2},k} = k_s \left( \frac{\Delta x_s + \Delta x_l}{2} \frac{\Delta z_s}{2} + \frac{\Delta x_s}{2} \frac{\Delta z_l}{2} \right) \frac{T_{i,j-1,k} - T_{i,j,k}}{\Delta y} \quad (\text{B.30})$$

$$\dot{Q}_{i,j+\frac{1}{2},k} = k_s \left( \frac{\Delta x_s + \Delta x_l}{2} \frac{\Delta z_s}{2} + \frac{\Delta x_s}{2} \frac{\Delta z_l}{2} \right) \frac{T_{i,j+1,k} - T_{i,j,k}}{\Delta y} \quad (\text{B.31})$$

$$\dot{Q}_{i,j,k-\frac{1}{2}} = k_s \frac{\Delta x_s + \Delta x_l}{2} \Delta y \frac{T_{i,j,k-1} - T_{i,j,k}}{\Delta z_l} \quad (\text{B.32})$$

$$\dot{Q}_{i,j,k+\frac{1}{2}} = k_s \frac{\Delta x_s}{2} \Delta y \frac{T_{i,j,k+1} - T_{i,j,k}}{\Delta z_s} \quad (\text{B.33})$$

For Region II the coordinate derivatives  $\partial\xi/\partial x$  and  $\partial\xi/\partial y$  are zero and  $\partial\xi/\partial z = 1$  due to the solid domain interface. Finite difference forms of the Equations B.4–7 become,

$$\dot{Q}_{i+\frac{1}{2},j,k} = k_l A_{x_{i+\frac{1}{2}}} \frac{\partial T}{\partial \lambda} = k_l A_{x_{i+\frac{1}{2}}} \frac{T_{i+1,j,k} - T_{i,j,k}}{\Delta \lambda} \quad (\text{B.34})$$

$$\dot{Q}_{i,j-\frac{1}{2},k} = k_l A_{y_{j-\frac{1}{2}}} \frac{\partial T}{\partial \eta} = k_l A_{y_{j-\frac{1}{2}}} \frac{T_{i,j-1,k} - T_{i,j,k}}{\Delta \eta} \quad (\text{B.35})$$

$$\dot{Q}_{i,j+\frac{1}{2},k} = k_l A_{y_{j+\frac{1}{2}}} \frac{\partial T}{\partial \eta} = k_l A_{y_{j+\frac{1}{2}}} \frac{T_{i,j+1,k} - T_{i,j,k}}{\Delta \eta} \quad (\text{B.36})$$

$$\dot{Q}_{i,j,k+\frac{1}{2}} = k_l A_z \frac{\partial T}{\partial \xi} = k_l A_z \frac{T_{i,j,k+1} - T_{i,j,k}}{\Delta \xi} \quad (\text{B.37})$$

Only the  $x$ -component of the  $\dot{Q}_{nt}$  is defined, since the surface normal at the grid point  $i, j, k + \frac{1}{2}$  is located on the solid line, where there is no variation in  $y$ -direction. Heat flow rates on the upper curved surface is defined by

$$\dot{Q}_{nt_x} = k_l A_{nt_x} \left[ \left( \frac{\partial T}{\partial \lambda} \right)_{i,j,k+\frac{1}{2}} + \left( \frac{\partial T}{\partial \xi} \frac{\partial \xi}{\partial x} \right)_{i,j,k+\frac{1}{2}} \right] \quad (\text{B.38})$$

where

$$\left( \frac{\partial T}{\partial \lambda} \right)_{i,j,k+\frac{1}{2}} = \frac{1}{2} \left[ \frac{T_{i+1,j,k} - T_{i,j,k}}{\Delta \lambda} + \frac{T_{i+1,j,k+1} - T_{i,j,k+1}}{\Delta \lambda} \right] \quad (\text{B.39})$$

$$\left( \frac{\partial T}{\partial \xi} \frac{\partial \xi}{\partial x} \right)_{i,j,k+\frac{1}{2}} = \frac{T_{i,j,k+1} - T_{i,j,k}}{\Delta \xi} \frac{1}{2} \left[ \left( \frac{\partial \xi}{\partial x} \right)_{i,j,k} + \left( \frac{\partial \xi}{\partial x} \right)_{i,j,k+1} \right] \quad (\text{B.40})$$

The convective terms are obtained from net enthalpy flow into the control volume given in Figure B.4. same as for Region I.

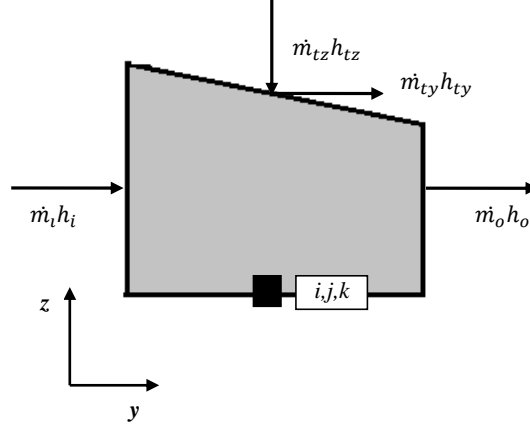


Figure B.4: Enthalpy flow to Region II

$$\dot{m}_i h_i - \dot{m}_o h_o - \dot{m}_{ty} h_{ty} + \dot{m}_{tz} h_{tz} = 0 \quad (\text{B.41})$$

$$\dot{m}_i = \frac{1}{2} (u_{j-1} + u_j) \rho_l A_{y_{j-\frac{1}{2}}} \quad T_i = \frac{1}{2} (T_{i,j,k} + T_{i,j-1,k})$$

$$\dot{m}_o = \frac{1}{2} (u_{j+1} + u_j) \rho_l A_{y_{j+\frac{1}{2}}} \quad T_o = \frac{1}{2} (T_{i,j,k} + T_{i,j+1,k})$$

$$\dot{m}_{ty} = u_j \rho_l A_{t_{ny}} \quad T_{ty} = \frac{1}{2} (T_{i,j,k} + T_{i,j,k+1})$$

$$\dot{m}_{tz} = -\dot{m}_i + \dot{m}_o + \dot{m}_{ty} \quad T_{tz} = \frac{1}{2} (T_{i,j,k} + T_{i,j,k+1})$$

### B.3 Energy Balance for Region III

Region III is located along the depth of the groove, where half of the control volume is in the solid and the other half is located in the liquid domain.

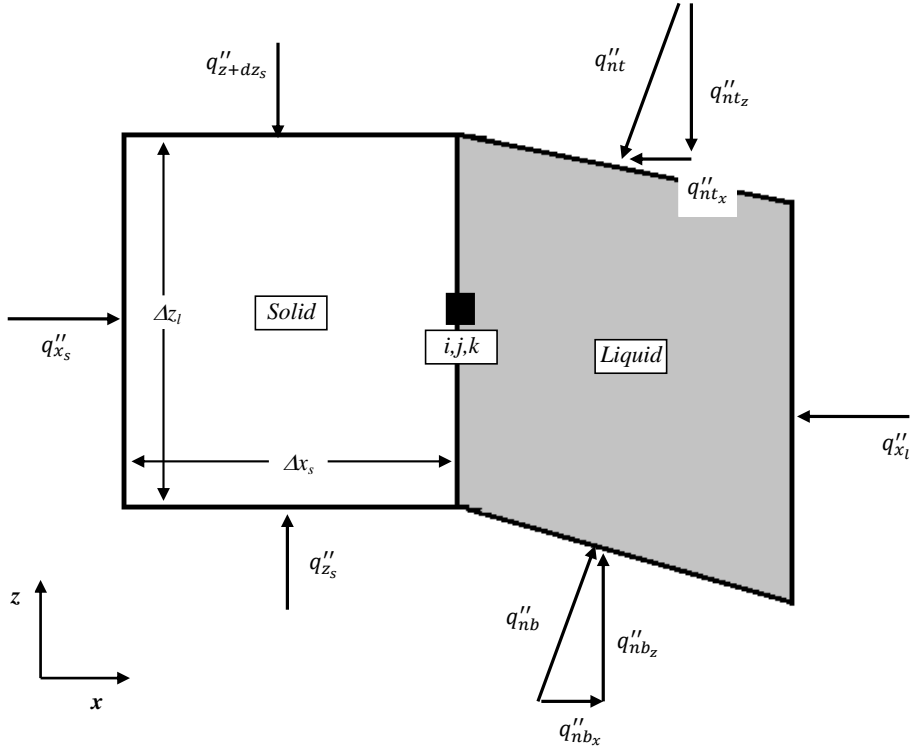


Figure B.5: Heat balance for Region III

$$\dot{Q}_{i-\frac{1}{2},j,k} = k_s A_x \frac{\partial T}{\partial x} = k_s \Delta z_l \Delta y \frac{T_{i-1,j,k} - T_{i,j,k}}{\Delta x_l} \quad (\text{B.42})$$

$$\dot{Q}_{i,j-\frac{1}{2},k} = k_s A_y \frac{\partial T}{\partial y} = k_s \frac{\Delta x_s}{2} \Delta z_l \frac{T_{i,j-1,k} - T_{i,j,k}}{\Delta y} \quad (\text{B.43})$$

$$\dot{Q}_{i,j+\frac{1}{2},k} = k_s A_y \frac{\partial T}{\partial y} = k_s \frac{\Delta x_s}{2} \Delta z_l \frac{T_{i,j+1,k} - T_{i,j,k}}{\Delta y} \quad (\text{B.44})$$

$$\dot{Q}_{i,j,k-\frac{1}{2}} = k_s A_z \frac{\partial T}{\partial z} = k_s \frac{\Delta x_s}{2} \Delta y \frac{T_{i,j,k-1} - T_{i,j,k}}{\Delta z_l} \quad (\text{B.45})$$

$$\dot{Q}_{i,j,k+\frac{1}{2}} = k_s A_z \frac{\partial T}{\partial z} = k_s \frac{\Delta x_s}{2} \Delta y \frac{T_{i,j,k+1} - T_{i,j,k}}{\Delta z_s} \quad (\text{B.46})$$

Similar to Region II, in Region III the coordinate derivative  $\partial\xi/\partial y$  is zero and  $\partial\xi/\partial z = 1$  due to the solid domain interface.

$$\dot{Q}_{i+\frac{1}{2},j,k} = k_l A_{x_{i+\frac{1}{2}}} \left[ \left( \frac{\partial T}{\partial \lambda} \right)_{i+\frac{1}{2},j,k} + \left( \frac{\partial T}{\partial \xi} \frac{\partial \xi}{\partial x} \right)_{i+\frac{1}{2},j,k} \right] \quad (\text{B.47})$$

where

$$\left( \frac{\partial T}{\partial \lambda} \right)_{i+\frac{1}{2},j,k} = \frac{T_{i+1,j,k} - T_{i,j,k}}{\Delta \lambda} \quad (\text{B.48})$$

$$\begin{aligned} \left( \frac{\partial T}{\partial \xi} \frac{\partial \xi}{\partial x} \right)_{i+\frac{1}{2},j,k} &= \frac{1}{2} \left[ \frac{T_{i,j,k+1} - T_{i,j,k-1}}{2\Delta \xi} + \frac{T_{i+1,j,k+1} - T_{i+1,j,k-1}}{2\Delta \xi} \right] \\ &+ \frac{1}{2} \left[ \left( \frac{\partial \xi}{\partial x} \right)_{i,j,k} + \left( \frac{\partial \xi}{\partial x} \right)_{i+1,j,k} \right] \end{aligned} \quad (\text{B.49})$$

$$\dot{Q}_{i,j-\frac{1}{2},k} = k_l A_{y_{j-\frac{1}{2}}} \frac{\partial T}{\partial \eta} = k_l A_{y_{j-\frac{1}{2}}} \frac{T_{i,j-1,k} - T_{i,j,k}}{\Delta \eta} \quad (\text{B.50})$$

$$\dot{Q}_{i,j+\frac{1}{2},k} = k_l A_{y_{j+\frac{1}{2}}} \frac{\partial T}{\partial \eta} = k_l A_{y_{j+\frac{1}{2}}} \frac{T_{i,j+1,k} - T_{i,j,k}}{\Delta \eta} \quad (\text{B.51})$$

$$\dot{Q}_{i,j,k-\frac{1}{2}} = k_l A_z \frac{\partial T}{\partial \xi} = k_l A_z \frac{T_{i,j,k-1} - T_{i,j,k}}{\Delta \xi} \quad (\text{B.52})$$

$$\dot{Q}_{i,j,k+\frac{1}{2}} = k_l A_z \frac{\partial T}{\partial \xi} = k_l A_z \frac{T_{i,j,k+1} - T_{i,j,k}}{\Delta \xi} \quad (\text{B.53})$$

For Region III both  $\dot{Q}_{nt}$  and  $\dot{Q}_{nb}$  are considered.

$$\dot{Q}_{nt_x} = k_l A_{nt_x} \left[ \left( \frac{\partial T}{\partial \lambda} \right)_{i,j,k+\frac{1}{2}} + \left( \frac{\partial T}{\partial \xi} \frac{\partial \xi}{\partial x} \right)_{i,j,k+\frac{1}{2}} \right] \quad (\text{B.54})$$

$$\dot{Q}_{nb_x} = k_l A_{nb_x} \left[ \left( \frac{\partial T}{\partial \lambda} \right)_{i,j,k-\frac{1}{2}} + \left( \frac{\partial T}{\partial \xi} \frac{\partial \xi}{\partial x} \right)_{i,j,k-\frac{1}{2}} \right] \quad (\text{B.55})$$

where

$$\left(\frac{\partial T}{\partial \lambda}\right)_{i,j,k+\frac{1}{2}} = \frac{1}{2} \left[ \frac{T_{i+1,j,k} - T_{i,j,k}}{\Delta \lambda} + \frac{T_{i+1,j,k+1} - T_{i,j,k+1}}{\Delta \lambda} \right] \quad (\text{B.56})$$

$$\left(\frac{\partial T}{\partial \xi} \frac{\partial \xi}{\partial x}\right)_{i,j,k+\frac{1}{2}} = \frac{T_{i,j,k+1} - T_{i,j,k}}{\Delta \xi} \frac{1}{2} \left[ \left(\frac{\partial \xi}{\partial x}\right)_{i,j,k} + \left(\frac{\partial \xi}{\partial x}\right)_{i,j,k+1} \right] \quad (\text{B.57})$$

$$\left(\frac{\partial T}{\partial \lambda}\right)_{i,j,k-\frac{1}{2}} = \frac{1}{2} \left[ \frac{T_{i,j,k} - T_{i+1,j,k}}{\Delta \lambda} + \frac{T_{i,j,k-1} - T_{i+1,j,k-1}}{\Delta \lambda} \right] \quad (\text{B.58})$$

$$\left(\frac{\partial T}{\partial \xi} \frac{\partial \xi}{\partial x}\right)_{i,j,k-\frac{1}{2}} = \frac{T_{i,j,k-1} - T_{i,j,k}}{\Delta \xi} \frac{1}{2} \left[ \left(\frac{\partial \xi}{\partial x}\right)_{i,j,k} + \left(\frac{\partial \xi}{\partial x}\right)_{i,j,k-1} \right] \quad (\text{B.59})$$

The convective terms are obtained from net enthalpy flow into the control volume given in Figure B.6.

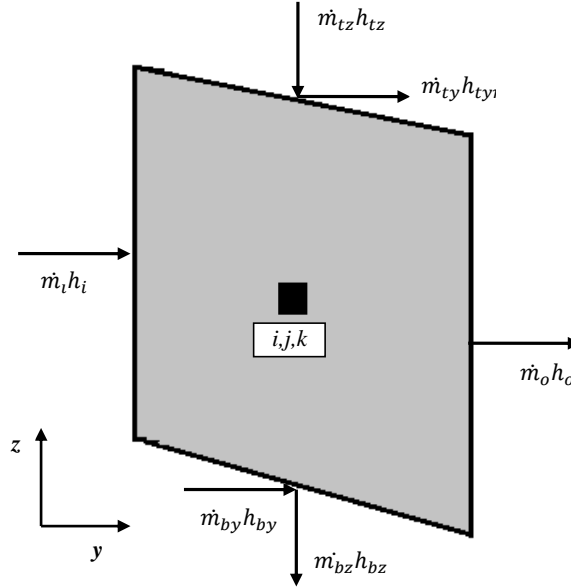


Figure B.6: Enthalpy flow to Region III

$$\dot{m}_i h_i - \dot{m}_o h_o - \dot{m}_{ty} h_{ty} + \dot{m}_{tz} h_{tz} + \dot{m}_{by} h_{by} - \dot{m}_{bz} h_{bz} = 0 \quad (\text{B.60})$$

$$\begin{aligned}
\dot{m}_i &= \frac{1}{2} (u_{j-1} + u_j) \rho_l A_{y_{j-\frac{1}{2}}} & T_i &= \frac{1}{2} (T_{i,j,k} + T_{i,j-1,k}) \\
\dot{m}_o &= \frac{1}{2} (u_{j+1} + u_j) \rho_l A_{y_{j+\frac{1}{2}}} & T_o &= \frac{1}{2} (T_{i,j,k} + T_{i,j+1,k}) \\
\dot{m}_{ty} &= u_j \rho_l A_{tn_y} & T_{ty} &= \frac{1}{2} (T_{i,j,k} + T_{i,j,k+1}) \\
\dot{m}_{tz} &= -\dot{m}_i + \dot{m}_o + \dot{m}_{ty} - \dot{m}_{by} + \dot{m}_{bz} & T_{tz} &= \frac{1}{2} (T_{i,j,k} + T_{i,j,k+1}) \\
\dot{m}_{by} &= u_j \rho_l A_{bn_y} & T_{by} &= \frac{1}{2} (T_{i,j,k} + T_{i,j,k-1}) \\
\dot{m}_{bz} &= (-\dot{m}_{tz})_{k-\frac{1}{2}} & T_{bz} &= \frac{1}{2} (T_{i,j,k} + T_{i,j,k-1})
\end{aligned}$$

#### B.4 Energy Balance for Region IV

Region IV is at fin top corner, where upper surface is liquid–vapor interface and includes phase change as given in Figure B.7.

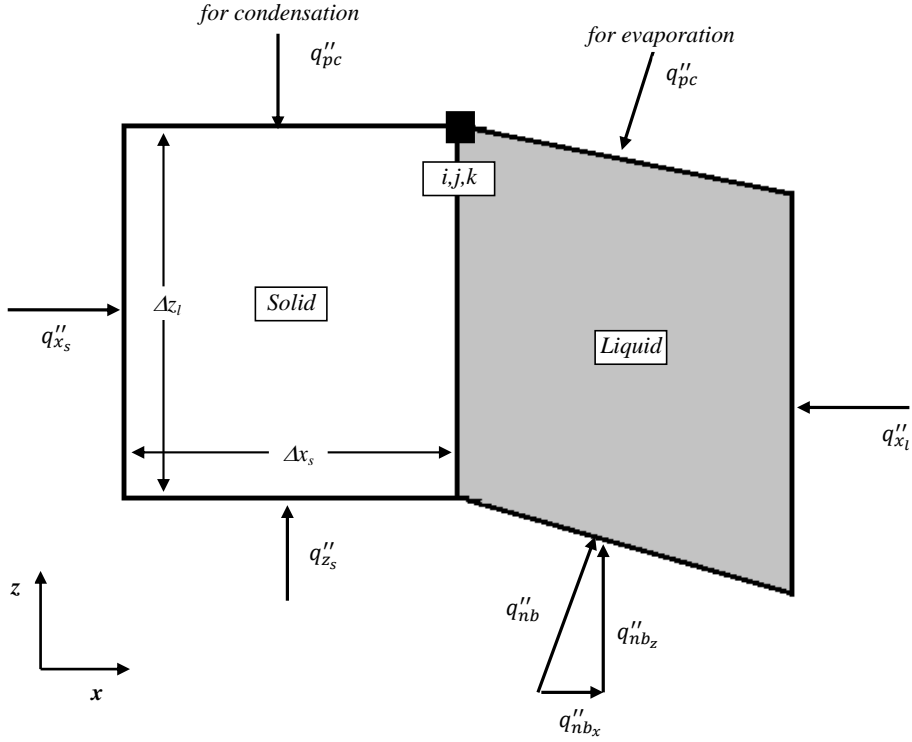


Figure B.7: Heat balance for Region IV

Heat flow rates in solid domain are defined as,

$$\dot{Q}_{i-\frac{1}{2},j,k} = k_s \frac{\Delta z_l}{2} \Delta y \frac{T_{i-1,j,k} - T_{i,j,k}}{\Delta x_s} \quad (\text{B.61})$$

$$\dot{Q}_{i,j-\frac{1}{2},k} = k_s \frac{\Delta x_s}{2} \frac{\Delta z_l}{2} \frac{T_{i,j-1,k} - T_{i,j,k}}{\Delta y} \quad (\text{B.62})$$

$$\dot{Q}_{i,j+\frac{1}{2},k} = k_s \frac{\Delta x_s}{2} \frac{\Delta z_l}{2} \frac{T_{i,j+1,k} - T_{i,j,k}}{\Delta y} \quad (\text{B.63})$$

$$\dot{Q}_{i,j,k-\frac{1}{2}} = k_s \frac{\Delta x_s}{2} \Delta y \frac{T_{i,j,k-1} - T_{i,j,k}}{\Delta z_l} \quad (\text{B.64})$$

For condensation region, phase change is defined by a convection boundary condition on the upper surface in the solid domain, whereas for evaporation region,

this surface is assumed to be insulated, where  $\dot{Q}_{pc}$  is taken as zero.

$$\dot{Q}_{i,j,k} = \dot{Q}_{pc} = h_{pc} \frac{\Delta x_s}{2} \Delta y (T_v - T_{i,j,k}) \quad (\text{B.65})$$

For Region IV the coordinate derivatives  $\partial\xi/\partial y$  is zero and  $\partial\xi/\partial z = 1$  due to the solid domain interface. Finite difference forms of the Equations B.4–8 become,

$$\dot{Q}_{i+\frac{1}{2},j,k} = k_l A_{x_{i+\frac{1}{2}}} \left[ \left( \frac{\partial T}{\partial \lambda} \right)_{i+\frac{1}{2},j,k} + \left( \frac{\partial T}{\partial \xi} \frac{\partial \xi}{\partial x} \right)_{i+\frac{1}{2},j,k} \right] \quad (\text{B.66})$$

where

$$\left( \frac{\partial T}{\partial \lambda} \right)_{i+\frac{1}{2},j,k} = \frac{T_{i+1,j,k} - T_{i,j,k}}{\Delta \lambda} \quad (\text{B.67})$$

$$\begin{aligned} \left( \frac{\partial T}{\partial \xi} \frac{\partial \xi}{\partial x} \right)_{i+\frac{1}{2},j,k} &= \frac{1}{2} \left[ \frac{T_{i,j,k} - T_{i,j,k-1}}{\Delta \xi} + \frac{T_{i+1,j,k} - T_{i+1,j,k-1}}{\Delta \xi} \right] \\ &+ \frac{1}{2} \left[ \left( \frac{\partial \xi}{\partial x} \right)_{i,j,k} + \left( \frac{\partial \xi}{\partial x} \right)_{i+1,j,k} \right] \end{aligned} \quad (\text{B.68})$$

$$\dot{Q}_{i,j-\frac{1}{2},k} = k_l A_{y_{j-\frac{1}{2}}} \frac{\partial T}{\partial \eta} = k_l A_{y_{j-\frac{1}{2}}} \frac{T_{i,j-1,k} - T_{i,j,k}}{\Delta \eta} \quad (\text{B.69})$$

$$\dot{Q}_{i,j+\frac{1}{2},k} = k_l A_{y_{j+\frac{1}{2}}} \frac{\partial T}{\partial \eta} = k_l A_{y_{j+\frac{1}{2}}} \frac{T_{i,j+1,k} - T_{i,j,k}}{\Delta \eta} \quad (\text{B.70})$$

$$\dot{Q}_{i,j,k-\frac{1}{2}} = k_l A_z \frac{\partial T}{\partial \xi} = k_l A_z \frac{T_{i,j,k-1} - T_{i,j,k}}{\Delta \xi} \quad (\text{B.71})$$

In region IV for evaporation region it is assumed that  $\dot{Q}_{nt}$  is equal to the phase change heat transfer and approximated with convection boundary condition.

$$\dot{Q}_{nt} = \dot{Q}_{pc} = h_{pc} \frac{\Delta x_l}{2} \Delta y (T_{i,j,k} - T_v) \quad (\text{B.72})$$

At the lower surface of the liquid domain

$$\dot{Q}_{nb_x} = k_l A_{nb_x} \left[ \left( \frac{\partial T}{\partial \lambda} \right)_{i,j,k-\frac{1}{2}} + \left( \frac{\partial T}{\partial \xi} \frac{\partial \xi}{\partial x} \right)_{i,j,k-\frac{1}{2}} \right] \quad (\text{B.73})$$

where

$$\left( \frac{\partial T}{\partial \lambda} \right)_{i,j,k-\frac{1}{2}} = \frac{1}{2} \left[ \frac{T_{i,j,k} - T_{i+1,j,k}}{\Delta \lambda} + \frac{T_{i,j,k-1} - T_{i+1,j,k-1}}{\Delta \lambda} \right] \quad (\text{B.74})$$

$$\left( \frac{\partial T}{\partial \xi} \frac{\partial \xi}{\partial x} \right)_{i,j,k-\frac{1}{2}} = \frac{T_{i,j,k-1} - T_{i,j,k}}{\Delta \xi} \frac{1}{2} \left[ \left( \frac{\partial \xi}{\partial x} \right)_{i,j,k} + \left( \frac{\partial \xi}{\partial x} \right)_{i,j,k-1} \right] \quad (\text{B.75})$$

The convective terms are obtained from net enthalpy flow into the control volume given in Figure B.8.

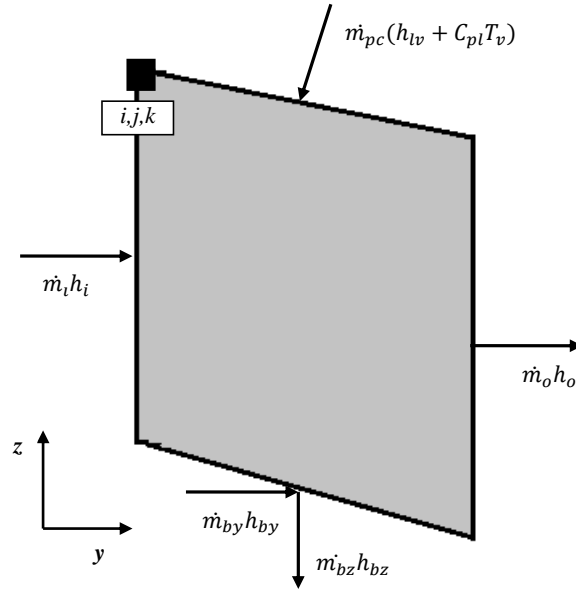


Figure B.8: Enthalpy flow to Region IV

$$\dot{m}_i h_i - \dot{m}_o h_o + \dot{m}_{by} h_{by} - \dot{m}_{bz} h_{bz} + \dot{m}_{pc} (h_{lv} + T_v) = 0 \quad (\text{B.76})$$

$\dot{m}_{pc}$  represent phase change mass flow rate for both condensation and evaporation and calculated by a mass balance defined as below.

$$\dot{m}_i = \frac{1}{2} (u_{j-1} + u_j) \rho_l A_{y_{j-\frac{1}{2}}}$$

$$T_i = \frac{1}{2} (T_{i,j,k} + T_{i,j-1,k})$$

$$\dot{m}_o = \frac{1}{2} (u_{j+1} + u_j) \rho_l A_{y_{j+\frac{1}{2}}}$$

$$T_o = \frac{1}{2} (T_{i,j,k} + T_{i,j+1,k})$$

$$\dot{m}_{by} = u_j \rho_l A_{b_{n_y}}$$

$$T_{by} = \frac{1}{2} (T_{i,j,k} + T_{i,j,k-1})$$

$$\dot{m}_{bz} = (-\dot{m}_{tz})_{k-\frac{1}{2}}$$

$$T_{bz} = \frac{1}{2} (T_{i,j,k} + T_{i,j,k-1})$$

$$\dot{m}_{pc} = -\dot{m}_i + \dot{m}_o - \dot{m}_{by} + \dot{m}_{bz}$$

Since  $\dot{m}_{pc} h_{lv}$  is considered in overall energy balance, it is not included again in convective terms.

## B.5 Energy Balance for Region V

Region V is located fully in the liquid domain, where the heat fluxes on each face are shown in Figure B.9.

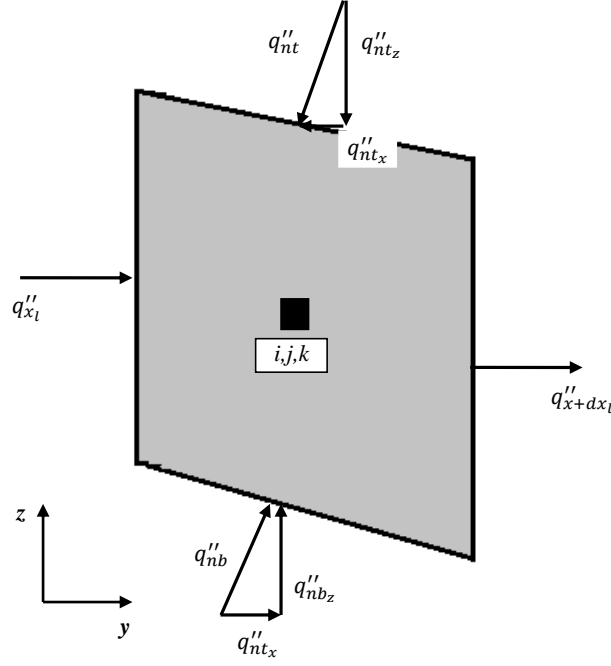


Figure B.9: Heat balance for Region V

Finite difference forms of the Equations B.4–10 become,

$$\dot{Q}_{i-\frac{1}{2},j,k} = k_l A_{x_{i-\frac{1}{2}}} \left[ \left( \frac{\partial T}{\partial \lambda} \right)_{i-\frac{1}{2},j,k} + \left( \frac{\partial T}{\partial \xi} \frac{\partial \xi}{\partial x} \right)_{i-\frac{1}{2},j,k} \right] \quad (\text{B.77})$$

$$\dot{Q}_{i+\frac{1}{2},j,k} = k_l A_{x_{i+\frac{1}{2}}} \left[ \left( \frac{\partial T}{\partial \lambda} \right)_{i+\frac{1}{2},j,k} + \left( \frac{\partial T}{\partial \xi} \frac{\partial \xi}{\partial x} \right)_{i+\frac{1}{2},j,k} \right] \quad (\text{B.78})$$

$$\dot{Q}_{i,j-\frac{1}{2},k} = k_l A_{y_{j-\frac{1}{2}}} \left[ \left( \frac{\partial T}{\partial \eta} \right)_{i,j-\frac{1}{2},k} + \left( \frac{\partial T}{\partial \xi} \frac{\partial \xi}{\partial y} \right)_{i,j-\frac{1}{2},k} \right] \quad (\text{B.79})$$

$$\dot{Q}_{i,j+\frac{1}{2},k} = k_l A_{y_{j+\frac{1}{2}}} \left[ \left( \frac{\partial T}{\partial \eta} \right)_{i,j+\frac{1}{2},k} + \left( \frac{\partial T}{\partial \xi} \frac{\partial \xi}{\partial y} \right)_{i,j+\frac{1}{2},k} \right] \quad (\text{B.80})$$

$$\dot{Q}_{i,j,k-\frac{1}{2}} = k_l A_z \frac{\partial T}{\partial \xi} \left( \frac{\partial \xi}{\partial z} \right)_{i,j,k-\frac{1}{2}} = k_l A_z \frac{T_{i,j,k-1} - T_{i,j,k}}{\Delta \xi} \left( \frac{\partial \xi}{\partial z} \right)_{i,j,k-\frac{1}{2}} \quad (\text{B.81})$$

$$\dot{Q}_{i,j,k+\frac{1}{2}} = k_l A_z \frac{\partial T}{\partial \xi} \left( \frac{\partial \xi}{\partial z} \right)_{i,j,k+\frac{1}{2}} = k_l A_z \frac{T_{i,j,k+1} - T_{i,j,k}}{\Delta \xi} \left( \frac{\partial \xi}{\partial z} \right)_{i,j,k+\frac{1}{2}} \quad (\text{B.82})$$

where

$$\left( \frac{\partial T}{\partial \lambda} \right)_{i-\frac{1}{2},j,k} = \frac{T_{i-1,j,k} - T_{i,j,k}}{\Delta \lambda} \quad (\text{B.83})$$

$$\left( \frac{\partial T}{\partial \lambda} \right)_{i+\frac{1}{2},j,k} = \frac{T_{i+1,j,k} - T_{i,j,k}}{\Delta \lambda} \quad (\text{B.84})$$

$$\left( \frac{\partial T}{\partial \eta} \right)_{i,j-\frac{1}{2},k} = \frac{T_{i,j-1,k} - T_{i,j,k}}{\Delta \eta} \quad (\text{B.85})$$

$$\left( \frac{\partial T}{\partial \eta} \right)_{i,j+\frac{1}{2},k} = \frac{T_{i,j+1,k} - T_{i,j,k}}{\Delta \eta} \quad (\text{B.86})$$

$$\begin{aligned} \left( \frac{\partial T}{\partial \xi} \frac{\partial \xi}{\partial x} \right)_{i-\frac{1}{2},j,k} &= \frac{1}{2} \left[ \frac{T_{i,j,k-1} - T_{i,j,k+1}}{2\Delta \xi} + \frac{T_{i-1,j,k-1} - T_{i-1,j,k+1}}{2\Delta \xi} \right] \\ &+ \frac{1}{2} \left[ \left( \frac{\partial \xi}{\partial x} \right)_{i,j,k} + \left( \frac{\partial \xi}{\partial x} \right)_{i-1,j,k} \right] \end{aligned} \quad (\text{B.87})$$

$$\begin{aligned} \left( \frac{\partial T}{\partial \xi} \frac{\partial \xi}{\partial x} \right)_{i+\frac{1}{2},j,k} &= \frac{1}{2} \left[ \frac{T_{i,j,k+1} - T_{i,j,k-1}}{2\Delta \xi} + \frac{T_{i+1,j,k+1} - T_{i+1,j,k-1}}{2\Delta \xi} \right] \\ &+ \frac{1}{2} \left[ \left( \frac{\partial \xi}{\partial x} \right)_{i,j,k} + \left( \frac{\partial \xi}{\partial x} \right)_{i+1,j,k} \right] \end{aligned} \quad (\text{B.88})$$

$$\begin{aligned} \left( \frac{\partial T}{\partial \xi} \frac{\partial \xi}{\partial y} \right)_{i,j-\frac{1}{2},k} &= \frac{1}{2} \left[ \frac{T_{i,j,k-1} - T_{i,j,k+1}}{2\Delta \xi} + \frac{T_{i,j-1,k-1} - T_{i,j-1,k+1}}{2\Delta \xi} \right] \\ &+ \frac{1}{2} \left[ \left( \frac{\partial \xi}{\partial y} \right)_{i,j,k} + \left( \frac{\partial \xi}{\partial y} \right)_{i,j-1,k} \right] \end{aligned} \quad (\text{B.89})$$

$$\begin{aligned} \left( \frac{\partial T}{\partial \xi} \frac{\partial \xi}{\partial y} \right)_{i,j+\frac{1}{2},k} &= \frac{1}{2} \left[ \frac{T_{i,j,k+1} - T_{i,j,k-1}}{2\Delta\xi} + \frac{T_{i,j+1,k+1} - T_{i,j+1,k-1}}{2\Delta\xi} \right] \\ &+ \frac{1}{2} \left[ \left( \frac{\partial \xi}{\partial y} \right)_{i,j,k} + \left( \frac{\partial \xi}{\partial y} \right)_{i,j+1,k} \right] \end{aligned} \quad (\text{B.90})$$

At the lower surface of the liquid domain

$$\dot{Q}_{nb_x} = k_l A_{nb_x} \left[ \left( \frac{\partial T}{\partial \lambda} \right)_{i,j,k-\frac{1}{2}} + \left( \frac{\partial T}{\partial \xi} \frac{\partial \xi}{\partial x} \right)_{i,j,k-\frac{1}{2}} \right] \quad (\text{B.91})$$

$$\dot{Q}_{nb_y} = k_l A_{nb_y} \left[ \left( \frac{\partial T}{\partial \eta} \right)_{i,j,k-\frac{1}{2}} + \left( \frac{\partial T}{\partial \xi} \frac{\partial \xi}{\partial y} \right)_{i,j,k-\frac{1}{2}} \right] \quad (\text{B.92})$$

where

$$\left( \frac{\partial T}{\partial \lambda} \right)_{i,j,k-\frac{1}{2}} = \frac{1}{2} \left[ \frac{T_{i-1,j,k} - T_{i+1,j,k}}{2\Delta\lambda} + \frac{T_{i-1,j,k-1} - T_{i+1,j,k-1}}{2\Delta\lambda} \right] \quad (\text{B.93})$$

$$\left( \frac{\partial T}{\partial \xi} \frac{\partial \xi}{\partial x} \right)_{i,j,k-\frac{1}{2}} = \frac{T_{i,j,k-1} - T_{i,j,k}}{\Delta\xi} \frac{1}{2} \left[ \left( \frac{\partial \xi}{\partial x} \right)_{i,j,k} + \left( \frac{\partial \xi}{\partial x} \right)_{i,j,k-1} \right] \quad (\text{B.94})$$

$$\left( \frac{\partial T}{\partial \eta} \right)_{i,j,k-\frac{1}{2}} = \frac{1}{2} \left[ \frac{T_{i,j-1,k} - T_{i,j+1,k}}{2\Delta\eta} + \frac{T_{i,j-1,k-1} - T_{i,j+1,k-1}}{2\Delta\eta} \right] \quad (\text{B.95})$$

$$\left( \frac{\partial T}{\partial \xi} \frac{\partial \xi}{\partial y} \right)_{i,j,k-\frac{1}{2}} = \frac{T_{i,j,k-1} - T_{i,j,k}}{\Delta\xi} \frac{1}{2} \left[ \left( \frac{\partial \xi}{\partial y} \right)_{i,j,k} + \left( \frac{\partial \xi}{\partial y} \right)_{i,j,k-1} \right] \quad (\text{B.96})$$

At the upper surface of the liquid domain

$$\dot{Q}_{nt_x} = k_l A_{nt_x} \left[ \left( \frac{\partial T}{\partial \lambda} \right)_{i,j,k+\frac{1}{2}} + \left( \frac{\partial T}{\partial \xi} \frac{\partial \xi}{\partial x} \right)_{i,j,k+\frac{1}{2}} \right] \quad (\text{B.97})$$

$$\dot{Q}_{nt_y} = k_l A_{nt_y} \left[ \left( \frac{\partial T}{\partial \eta} \right)_{i,j,k+\frac{1}{2}} + \left( \frac{\partial T}{\partial \xi} \frac{\partial \xi}{\partial y} \right)_{i,j,k+\frac{1}{2}} \right] \quad (\text{B.98})$$

where

$$\left(\frac{\partial T}{\partial \lambda}\right)_{i,j,k+\frac{1}{2}} = \frac{1}{2} \left[ \frac{T_{i+1,j,k} - T_{i-1,j,k}}{2\Delta\lambda} + \frac{T_{i+1,j,k+1} - T_{i-1,j,k+1}}{2\Delta\lambda} \right] \quad (\text{B.99})$$

$$\left(\frac{\partial T}{\partial \xi} \frac{\partial \xi}{\partial x}\right)_{i,j,k+\frac{1}{2}} = \frac{T_{i,j,k+1} - T_{i,j,k}}{\Delta\xi} \frac{1}{2} \left[ \left(\frac{\partial \xi}{\partial x}\right)_{i,j,k} + \left(\frac{\partial \xi}{\partial x}\right)_{i,j,k+1} \right] \quad (\text{B.100})$$

$$\left(\frac{\partial T}{\partial \eta}\right)_{i,j,k+\frac{1}{2}} = \frac{1}{2} \left[ \frac{T_{i,j+1,k} - T_{i,j-1,k}}{2\Delta\eta} + \frac{T_{i,j+1,k+1} - T_{i,j-1,k+1}}{2\Delta\eta} \right] \quad (\text{B.101})$$

$$\left(\frac{\partial T}{\partial \xi} \frac{\partial \xi}{\partial y}\right)_{i,j,k+\frac{1}{2}} = \frac{T_{i,j,k+1} - T_{i,j,k}}{\Delta\xi} \frac{1}{2} \left[ \left(\frac{\partial \xi}{\partial y}\right)_{i,j,k} + \left(\frac{\partial \xi}{\partial y}\right)_{i,j,k+1} \right] \quad (\text{B.102})$$

The convective terms are obtained from net enthalpy flow into the control volume given in Figure B.10.

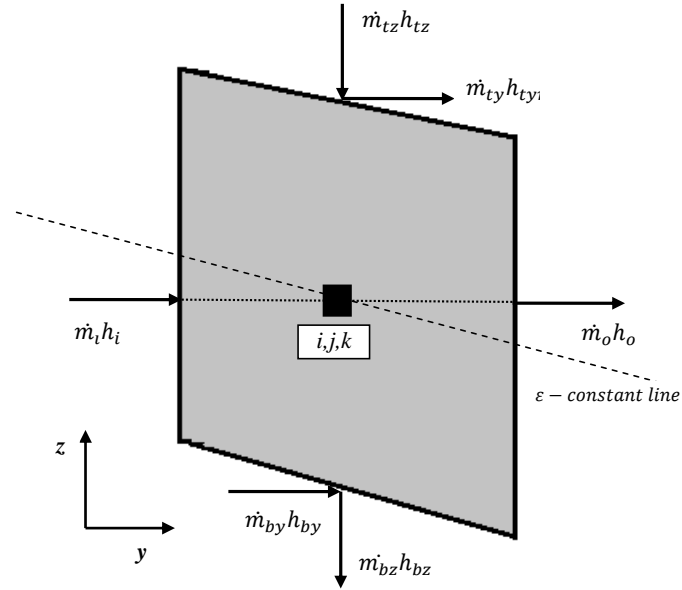


Figure B.10: Enthalpy flow to Region V

$$\dot{m}_i h_i - \dot{m}_o h_o - \dot{m}_{ty} h_{ty} + \dot{m}_{tz} h_{tz} + \dot{m}_{by} h_{by} - \dot{m}_{bz} h_{bz} = 0 \quad (\text{B.103})$$

For Region V  $\partial\xi/\partial y$  term is not zero, therefore inflow and outflow temperatures are interpolated.

$$\dot{m}_i = \frac{1}{2} (u_{j-1} + u_j) \rho_l A_{y_{j-\frac{1}{2}}} \quad T_i = T_{i,j-\frac{1}{2},k} + s_1 \left( T_{i,j-\frac{1}{2},k} - T_{i,j-\frac{1}{2},k-\frac{1}{2}} \right)$$

$$\dot{m}_o = \frac{1}{2} (u_{j+1} + u_j) \rho_l A_{y_{j+\frac{1}{2}}} \quad T_o = T_{i,j+\frac{1}{2},k} + s_2 \left( T_{i,j+\frac{1}{2},k} - T_{i,j+\frac{1}{2},k+\frac{1}{2}} \right)$$

$$\dot{m}_{ty} = u_j \rho_l A_{tn_y} \quad T_{ty} = \frac{1}{2} (T_{i,j,k} + T_{i,j,k+1})$$

$$\dot{m}_{tz} = -\dot{m}_i + \dot{m}_o + \dot{m}_{ty} - \dot{m}_{by} + \dot{m}_{bz} \quad T_{tz} = \frac{1}{2} (T_{i,j,k} + T_{i,j,k+1})$$

$$\dot{m}_{by} = u_j \rho_l A_{bn_y} \quad T_{by} = \frac{1}{2} (T_{i,j,k} + T_{i,j,k-1})$$

$$\dot{m}_{bz} = (-\dot{m}_{tz})_{k-\frac{1}{2}} \quad T_{bz} = \frac{1}{2} (T_{i,j,k} + T_{i,j,k-1})$$

where

$$s_1 = \frac{z_{i,j,k} - z_{i,j-\frac{1}{2},k}}{z_{i,j-\frac{1}{2},k} - z_{i,j-\frac{1}{2},k-\frac{1}{2}}}$$

$$s_2 = \frac{z_{i,j,k} - z_{i,j+\frac{1}{2},k}}{z_{i,j+\frac{1}{2},k} - z_{i,j+\frac{1}{2},k+\frac{1}{2}}}$$

## B.6 Energy Balance for Liquid–Vapor Interface

Heat balance equation for the top region, liquid–vapor interface in the liquid domain is written to calculate the phase change mass flow rates for both condensation and evaporation from macro region.

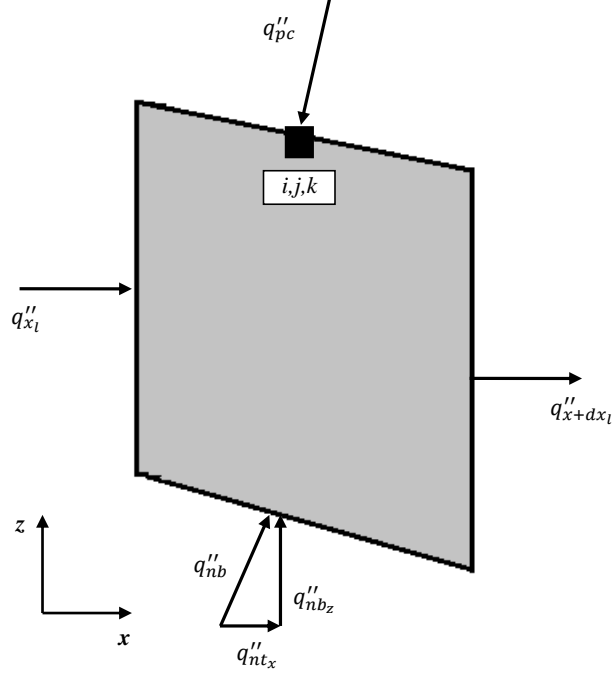


Figure B.11: Heat balance at the liquid–vapor interface

$$\dot{Q}_{i-\frac{1}{2},j,k} = k_l A_{x_{i-\frac{1}{2}}} \left[ \left( \frac{\partial T}{\partial \lambda} \right)_{i-\frac{1}{2},j,k} + \left( \frac{\partial T}{\partial \xi} \frac{\partial \xi}{\partial x} \right)_{i-\frac{1}{2},j,k} \right] \quad (\text{B.104})$$

$$\dot{Q}_{i+\frac{1}{2},j,k} = k_l A_{x_{i+\frac{1}{2}}} \left[ \left( \frac{\partial T}{\partial \lambda} \right)_{i+\frac{1}{2},j,k} + \left( \frac{\partial T}{\partial \xi} \frac{\partial \xi}{\partial x} \right)_{i+\frac{1}{2},j,k} \right] \quad (\text{B.105})$$

$$\dot{Q}_{i,j-\frac{1}{2},k} = k_l A_{y_{j-\frac{1}{2}}} \left[ \left( \frac{\partial T}{\partial \eta} \right)_{i,j-\frac{1}{2},k} + \left( \frac{\partial T}{\partial \xi} \frac{\partial \xi}{\partial y} \right)_{i,j-\frac{1}{2},k} \right] \quad (\text{B.106})$$

$$\dot{Q}_{i,j+\frac{1}{2},k} = k_l A_{y_{j+\frac{1}{2}}} \left[ \left( \frac{\partial T}{\partial \eta} \right)_{i,j+\frac{1}{2},k} + \left( \frac{\partial T}{\partial \xi} \frac{\partial \xi}{\partial y} \right)_{i,j+\frac{1}{2},k} \right] \quad (\text{B.107})$$

$$\dot{Q}_{i,j,k-\frac{1}{2}} = k_l A_z \frac{\partial T}{\partial \xi} \left( \frac{\partial \xi}{\partial z} \right)_{i,j,k-\frac{1}{2}} = k_l A_z \frac{T_{i,j,k-1} - T_{i,j,k}}{\Delta \xi} \left( \frac{\partial \xi}{\partial z} \right)_{i,j,k-\frac{1}{2}} \quad (\text{B.108})$$

where

$$\left(\frac{\partial T}{\partial \lambda}\right)_{i-\frac{1}{2},j,k} = \frac{T_{i-1,j,k} - T_{i,j,k}}{\Delta \lambda} \quad (\text{B.109})$$

$$\left(\frac{\partial T}{\partial \lambda}\right)_{i+\frac{1}{2},j,k} = \frac{T_{i+1,j,k} - T_{i,j,k}}{\Delta \lambda} \quad (\text{B.110})$$

$$\left(\frac{\partial T}{\partial \eta}\right)_{i,j-\frac{1}{2},k} = \frac{T_{i,j-1,k} - T_{i,j,k}}{\Delta \eta} \quad (\text{B.111})$$

$$\left(\frac{\partial T}{\partial \eta}\right)_{i,j+\frac{1}{2},k} = \frac{T_{i,j+1,k} - T_{i,j,k}}{\Delta \eta} \quad (\text{B.112})$$

$$\begin{aligned} \left(\frac{\partial T}{\partial \xi} \frac{\partial \xi}{\partial x}\right)_{i-\frac{1}{2},j,k} &= \frac{1}{2} \left[ \frac{T_{i,j,k-1} - T_{i,j,k+1}}{2\Delta \xi} + \frac{T_{i-1,j,k-1} - T_{i-1,j,k+1}}{2\Delta \xi} \right] \\ &+ \frac{1}{2} \left[ \left(\frac{\partial \xi}{\partial x}\right)_{i,j,k} + \left(\frac{\partial \xi}{\partial x}\right)_{i-1,j,k} \right] \end{aligned} \quad (\text{B.113})$$

$$\begin{aligned} \left(\frac{\partial T}{\partial \xi} \frac{\partial \xi}{\partial x}\right)_{i+\frac{1}{2},j,k} &= \frac{1}{2} \left[ \frac{T_{i,j,k+1} - T_{i,j,k-1}}{2\Delta \xi} + \frac{T_{i+1,j,k+1} - T_{i+1,j,k-1}}{2\Delta \xi} \right] \\ &+ \frac{1}{2} \left[ \left(\frac{\partial \xi}{\partial x}\right)_{i,j,k} + \left(\frac{\partial \xi}{\partial x}\right)_{i+1,j,k} \right] \end{aligned} \quad (\text{B.114})$$

$$\begin{aligned} \left(\frac{\partial T}{\partial \xi} \frac{\partial \xi}{\partial y}\right)_{i,j-\frac{1}{2},k} &= \frac{1}{2} \left[ \frac{T_{i,j,k-1} - T_{i,j,k+1}}{2\Delta \xi} + \frac{T_{i,j-1,k-1} - T_{i,j-1,k+1}}{2\Delta \xi} \right] \\ &+ \frac{1}{2} \left[ \left(\frac{\partial \xi}{\partial y}\right)_{i,j,k} + \left(\frac{\partial \xi}{\partial y}\right)_{i,j-1,k} \right] \end{aligned} \quad (\text{B.115})$$

$$\begin{aligned} \left(\frac{\partial T}{\partial \xi} \frac{\partial \xi}{\partial y}\right)_{i,j+\frac{1}{2},k} &= \frac{1}{2} \left[ \frac{T_{i,j,k+1} - T_{i,j,k-1}}{2\Delta \xi} + \frac{T_{i,j+1,k+1} - T_{i,j+1,k-1}}{2\Delta \xi} \right] \\ &+ \frac{1}{2} \left[ \left(\frac{\partial \xi}{\partial y}\right)_{i,j,k} + \left(\frac{\partial \xi}{\partial y}\right)_{i,j+1,k} \right] \end{aligned} \quad (\text{B.116})$$

At the lower surface of the liquid domain

$$\dot{Q}_{nb_x} = k_l A_{nb_x} \left[ \left( \frac{\partial T}{\partial \lambda} \right)_{i,j,k-\frac{1}{2}} + \left( \frac{\partial T}{\partial \xi} \frac{\partial \xi}{\partial x} \right)_{i,j,k-\frac{1}{2}} \right] \quad (\text{B.117})$$

$$\dot{Q}_{nb_y} = k_l A_{nb_y} \left[ \left( \frac{\partial T}{\partial \eta} \right)_{i,j,k-\frac{1}{2}} + \left( \frac{\partial T}{\partial \xi} \frac{\partial \xi}{\partial y} \right)_{i,j,k-\frac{1}{2}} \right] \quad (\text{B.118})$$

where

$$\left( \frac{\partial T}{\partial \lambda} \right)_{i,j,k-\frac{1}{2}} = \frac{1}{2} \left[ \frac{T_{i-1,j,k} - T_{i+1,j,k}}{2\Delta\lambda} + \frac{T_{i-1,j,k-1} - T_{i+1,j,k-1}}{2\Delta\lambda} \right] \quad (\text{B.119})$$

$$\left( \frac{\partial T}{\partial \xi} \frac{\partial \xi}{\partial x} \right)_{i,j,k-\frac{1}{2}} = \frac{T_{i,j,k-1} - T_{i,j,k}}{\Delta\xi} \frac{1}{2} \left[ \left( \frac{\partial \xi}{\partial x} \right)_{i,j,k} + \left( \frac{\partial \xi}{\partial x} \right)_{i,j,k-1} \right] \quad (\text{B.120})$$

$$\left( \frac{\partial T}{\partial \eta} \right)_{i,j,k-\frac{1}{2}} = \frac{1}{2} \left[ \frac{T_{i,j-1,k} - T_{i,j+1,k}}{2\Delta\eta} + \frac{T_{i,j-1,k-1} - T_{i,j+1,k-1}}{2\Delta\eta} \right] \quad (\text{B.121})$$

$$\left( \frac{\partial T}{\partial \xi} \frac{\partial \xi}{\partial y} \right)_{i,j,k-\frac{1}{2}} = \frac{T_{i,j,k-1} - T_{i,j,k}}{\Delta\xi} \frac{1}{2} \left[ \left( \frac{\partial \xi}{\partial y} \right)_{i,j,k} + \left( \frac{\partial \xi}{\partial y} \right)_{i,j,k-1} \right] \quad (\text{B.122})$$

The convective terms are obtained from net enthalpy flow into the control volume given in Figure B.12.

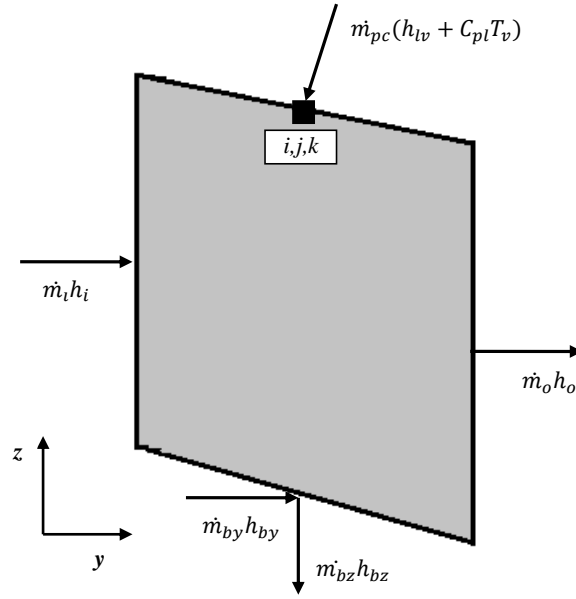


Figure B.12: Enthalpy flow at the liquid–vapor interface

$$\dot{m}_i h_i - \dot{m}_o h_o + \dot{m}_{by} h_{by} - \dot{m}_{bz} h_{bz} + \dot{m}_{pc} (h_{lv} + C_{pl} T_v) = 0 \quad (\text{B.123})$$

$$\dot{m}_i = \frac{1}{2} (u_{j-1} + u_j) \rho_l A_{y_{j-\frac{1}{2}}}$$

$$T_i = \frac{1}{2} (T_{i,j,k} + T_{i,j-1,k})$$

$$\dot{m}_o = \frac{1}{2} (u_{j+1} + u_j) \rho_l A_{y_{j+\frac{1}{2}}}$$

$$T_o = \frac{1}{2} (T_{i,j,k} + T_{i,j+1,k})$$

$$\dot{m}_{by} = u_j \rho_l A_{bn_y}$$

$$T_{by} = \frac{1}{2} (T_{i,j,k} + T_{i,j,k-1})$$

$$\dot{m}_{bz} = (-\dot{m}_{tz})_{k-\frac{1}{2}}$$

$$T_{bz} = \frac{1}{2} (T_{i,j,k} + T_{i,j,k-1})$$

From overall energy balance mass flow rate for phase change,  $\dot{m}_{pc}$ , can be calculated as given.

$$\begin{aligned}
& \dot{Q}_{net} + \dot{m}_i C_{p_i} (T_i - T_v) - \dot{m}_o C_{p_i} (T_o - T_v) + \\
& \dot{m}_{by} C_{p_i} (T_{by} - T_v) - \dot{m}_{bz} (T_{bz} - T_v) + \dot{m}_{pc} h_{lv} = 0 \quad (\text{B.124})
\end{aligned}$$



# CURRICULUM VITAE

## PERSONAL INFORMATION

**Surname, Name:** ODABAŞI, Gülnihal

**Nationality:** Turkish (TC)

**Date and Place of Birth:** 1972, Ankara

**Marital Status:** Single

**Phone:** (533)2592750

**Fax:** —

## EDUCATION

Degree	Institution	Year of Graduation
M.S.	METU	1997
B.S.	METU	1995
High School	Ankara Anatolian High School	1990

## PROFESSIONAL EXPERIENCE

Year	Place	Enrollment
1997–2006	ROKETSAN	Engineer
2006–2007	TUBITAK Space Technologies Research Institute	Researcher
2007–2013	STM Defence Technologies and Engineering	Certification Engineer

## **PUBLICATIONS**

### **International Publications**

DURSUNKAYA Z. ODABAŞI G. “Numerical solution of solidification in a square prism using an algebraic grid generation technique” Heat and Mass Transfer, 40, pp 91–97, 2003